Ulrich Haselmann, BSc

Direct-Write Fabrication of Pure Metal Structures for Nano-Probing and Plasmonic Applications

MASTER'S THESIS

to achieve the university degree of

Diplom-Ingenieur

Master's degree programme: Technical Physics

submitted to

Graz University of Technology

Supervisor

Univ.-Doz. Dipl.-Ing. Dr. techn. Harald Plank

Institute for Electron Microscopy and Nanoanalysis

Graz, July 2016

AFFIDAVIT

I declare that I have authored this thesis independently, that I have not used other than the declared sources/resources, and that I have explicitly indicated all material which has been quoted either literally or by content from the sources used. The text document uploaded to TUGRAZonline is identical to the present master‘s thesis.

Date

Signature

Abstract

Focused Electron Beam Induced Deposition (**FEBID**) is a direct-write bottom-up nanofabrication method with true 3D capabilities (“3D nanoprinter”). Typically, this technology is executed in the vacuum chamber of a scanning electron / scanning ion beam microscope (**SEM** / **FIB**), where gaseous precursor molecules are injected via a fine capillary. They physisorb to the sample surface and are dissociated by the particle beam into volatile and non-volatile fragments with the latter forming the functional deposit. For a diverse range of applications, FEBID allows the fabrication of conductive, semi-conducting, insulating, or magnetic materials. However, for a long time FEBID deposits suffered from partly huge carbon impurities up to 90 at.%. Recently, it has been demonstrated at the Institute for Electron Microscopy and Nanoanalyis (Graz University of Technology, Austria), that e-beam assisted purification of Pt-C deposits in H_2O vapour can be used to entirely remove the carbon content resulting in pore and crack free morphologies and a minimal lateral shrink of less than 5 rel.%. Based on that breakthrough this master thesis focuses on application aspects of pure metallic, FEBID based (nano)structures.

In the premier part, the thesis focuses on the first industrial small-scale application of FEBID Pt materials, where both main aspects, the direct-write and pure-metal character, are of decisive relevance. Foremost, experiments to optimize the purification process were done. Therefore, the effect of different purification beam energies was examined for thin deposit layers. Also the resistivity of deposits during and after the purification was examined and optimized, which confirmed the suitability of the approach for the indented industrial application. Finally, the know-how was used to modify novel, self-sensing cantilevers for a special high-speed atomic force microscope (**AFM**), which can seamlessly be integrated in SEMs, FIBs and dual beam instruments. Thereby, FEBID’s capabilities to produce pure metal tips for conductive-AFM measurements and localized nano-probing, but also the on-demand shaping according to the addressed problem, proved essential. These results will leverage the utilization of the special high-speed AFM (**AFSEM™**) as an electric characterization tool beyond current possibilities.

In the second part of this thesis the above mentioned purification approach is successfully expanded to Au based precursor materials. This is of essential importance for e.g. plasmonic structures, as FEBID allows a highly flexible fabrication on practically any given surface. AFM, high-resolution transmission electron microscopy (**TEM**), energy dispersive X-ray spectroscopy (**EDXS**) in SEMs as well as in scanning TEMs (**S-TEM**) and electron energy loss spectroscopy (**EELS**) were used to characterize the morphology, the chemistry and the inner structure of purified Au FEBID deposits. To remove occasionally appearing carbon residues around the edges of the purification area, a new post purification cleaning approach was developed. STEM EELS was then used to prove the plasmonic activity of FEBID produced nano-discs. In the last step, in the effort to fabricate terahertz plasmonic structures, the resolution limits for bi-ring patterns were investigated.

By overcoming the long lasting problem of high carbon contents, FEBID is now at a turning point as it finally can fully exploit its unique strengths of a mask-less, direct-write fabrication on practically any given surface together with a pure metal character for full functionality.

Kurzfassung

Fokussierte Elektronenstrahl induzierte Abscheidung (Focused Electron Beam Induced Deposition, **FEBID**) ist eine direkt schreibende, von unten nach oben arbeitende Nanofabrikationstechnik mit richtigen 3D Fähigkeiten („3D Nanodrucker“). Dabei wird diese Technik typischerweise in der Kammer eines Rasterelektronenmikroskops (**REM**) oder eines Rasterionenmikroskops (**RIM**) durchgeführt, wobei gasförmige Präkursormoleküle über eine feine Kapillare eingebracht werden. Sie haften durch Physisorption an der Probenoberfläche und werden durch den Partikelstrahl in flüchtige und nicht-flüchtige Bruchstücke zerlegt, wobei letztere die funktionelle Ablagerung bilden. FEBID erlaubt für ein weites Feld von Anwendungen die Fabrication von leitenden, halbleitenden, isolierenden oder magnetischen Materialien. Allerdings litten FEBID Abscheidungen für lange Zeit an großen Kohlenstoffverunreinigungen von bis zu 90 at.%. Kürzlich konnte am Institut für Elektronenmikroskopie und Nanoanalysis (Technische Universität Graz, Österreich) gezeigt werden, dass Elektronenstrahlunterstützte Aufreinigung von Pt-C Abscheidungen in H_2O Gas genutzt werden kann, um den Kohlenstoffanteil komplett zu entfernen resultierend in einer poren- und rissfreien Morphologie und geringem lateralem Schrumpfen von weniger als 5 rel.%. Basierend auf diesem Durchbruch, behandelt diese Masterarbeit Anwendungsaspekte von rein metallischen, FEBID basierenden (Nano)Strukturen.

Im ersten Teil, fokussiert sich diese Arbeit auf die erste kleinindustrielle Anwendung von FEBID Pt Material, bei der sowohl das direkte Schreiben als auch die reine Metallcharakteristik von entscheidender Relevanz sind. Als erstes wurden weitere Experimente zur Aufreinigungsoptimierung durchgeführt. Dafür wurde der Effekt von unterschiedlichen Aufreinigungsstrahlenergien für dünne Abscheidungen untersucht. Auch wurde der spezifische Widerstand während und nach der Aufreinigung untersucht und optimiert, wodurch die Eignung für die beabsichtigte industrielle Anwendung bestätigt werden konnte. Schlussendlich wurde das Knowhow genutzt um neuartige, selbsterfassende (self-sensing) Cantilever für ein spezielles Hochgeschwindigkeits-Rasterkraftmikroskope (**RKM**) zu modifizieren, welches nahtlos in REMs, RIMs und Zweistrahlengangmikroskopen integriert werden kann. Dabei waren die FEBID Fähigkeiten reine Metallspitzen für leitfähigkeitsmessende RKM Anwendungen herzustellen aber auch rascher Fertigungsmodifikationen essentiell. Diese Resultate werden diesem speziellen Hochgeschwindigkeits-RKM (AFSEM™) zum Durchbruch als ein Instrument für elektrisches Charakterisierung verhelfen.

Im zweiten Teil dieser Arbeit wird diese Aufreinigungstechnik erfolgreich auf Au-basierende Präkursormaterialien erweitert. Das ist von essentieller Wichtigkeit, z.B. für plasmonische Strukturen, deren Herstellung durch FEBID hochflexibel auf praktisch jeder Oberfläche wird. RKM, hochauflösende Transmissionselektronenmikroskopie (**TEM**), Röntgenstrukturanalyse sowohl durch REM als auch in Raster-TEM (**RTEM**) und Elektronenenergieverlustspektroskopie (Electron Energy Loss Spectroscopy, **EELS**) wurden genutzt um die Morphologie, die Chemie und die innere Struktur aufgereinigter, Au-basierender FEBID Abscheidungen zu untersuchen. Um gelegentlich auftretende Verunreinigungen entlang der Grenze des Aufreinigungsbereichs zu entfernen, wurde eine neue Reinigungstechnik für aufgereinigte Strukturen entwickelt. Danach wurde RTEM EELS genutzt um die

plasmonische Aktivität von mit FEBID hergestellten Nanoscheiben nachzuweisen. Im letzten Schritt wurde im Rahmen der Anstrengung plasmonische Strukturen im Terrahertz Bereich herzustellen, die Auflösungsgrenze für Doppelringstrukturen untersucht.

Durch das überwinden des lang andauernden Problems hoher Kohlenstoffanteile, befindet sich die FEBID Technik an einem Wendepunkt, da sie nun ihre einzigartigen Stärken von maskenloser, direktbeschreibender Herstellung auf praktisch jeder möglichen Oberfläche zusammen mit der nun möglichen reinen Metallcharakteristik komplett ausspielen kann.

Acknowledgements

First I would like to thank the head of the institute Prof. Dr. Ferdinand Hofer for giving me the opportunity to write my master thesis at this institute.

I want to express my biggest gratitude to my supervisor Univ.-Doz. Dr. Harald Plank for his encouragement to believe in my capabilities and his trust as well as his support. I would like to thank him for his great ideas, for teaching me, for taking his time and caring. By accepting me in his work group he gave me the unique possibility to be part of this interesting research project.

My gratitude goes to the whole workgroup S3 for being very supportive: DI Robert Winkler for his expertise and support towards FEBID processes and his feedback on my results, Dr. Thomas Ganner and DI Jürgen Sattelkov for advises and help towards AFM issues and Sebastian Rauch for the support concerning plasma cleaning.

I want to thank Dr. Franz Schmidt and DI Angelina Orthacker, who performed the TEM investigations, which revealed important results. In that frame, I also want to thank the head of their work group, Prof. Dr. Gerald Kothleitner for enabling this cooperation and his input.

My gratitude also goes to Dr. Julian Wagner, Mag. Manfred Nachtnebel, Dr. Armin Zankel, DI Harald Fitzek and Dr. Johannes Rattenberger for their help with ESEM issues. I also want to thank the other FELMI staff members for advice, help and providing such a comfortable working environment.

I have spent really good times with my colleagues from the institute, which I'm very grateful for.

I want to thank Prof. Dr. Michael Huth and his workgroup as well as *GETec Microscopy GmbH* and *SCL-Sensor.Tech. Fabrication GmbH* for fertile cooperation in regard of the research projects associated with this thesis. Without them, these projects wouldn't have been possilbe

I also want to thank my fellow students for the good times with each other and studying together. Esspecially I want to thank Dr. Andreas Kautsch, DI Gernot Kraberger and DI Michael Hollerer.

Finally, I want to express my deepest recognition to the people closest to me. I want to express my gratefulness for my parents who enabled my education and always supported me. My brothers for their company, the fun we had together and also their support. Finally, I want to thank my closest friends, especially Dr. Christian Vetta and Hüseyin Birtan Kalelioglu.

Table of Contents

1 Introduction 7
2 Instrumentation and Basics of the Used Experimental Techniques 8
2.1 Nanofabrication 8
2.1.1 Dual Beam Microscope (DBM) 8
2.1.2 Focused Electron Beam Induced Deposition (FEBID) 12
2.2 Purification 19
2.2.1 Environmental Scanning Electron Microscopy (ESEM) 19
2.2.2 The Process of Purification 20
2.3 Plasma Cleaning 24
2.4 Characterization 24
2.4.1 EDXS 24
2.4.2 Atomic Force Microscopy (AFM) 29
2.4.3 Transmission Electron Microscopy (TEM) 32
2.4.4 Electric Measurements 36
3 Experiments and Results 38
3.1 Platinum High-Resolution AFM Tips for Electric Measurements 40
3.1.1 Motivation 40
3.1.2 Height Calibration and Growth Rates for the Pt Precursor 41
3.1.3 Purification of µm-Scale Pt-C Pads with Different Primary Beam Energies 42
3.1.4 Electric Characterisation of Purified Pt Deposits 46
3.1.5 FEBID Modification of Self-Sensing Cantilevers for Electric Measurements 55
3.1.6 Summary and Outlook 66
3.2 Plasmonic Gold Nanostructures Produced via FEBID 68
3.2.1 Motivation 68
3.2.2 Au Precursor Deposition Behaviour 69
3.2.3 Au Precursor Purification Behaviour 73
3.2.4 Post Purification Cleaning 78
3.2.5 Plasmonic Au Discs 80
3.2.6 Downscaling and Plasmonic Au Bi-Rings 92
3.2.7 Summary and Outlook 103
4 Conclusion 105

List of Abbreviations

Abbreviation	Meaning
ADF	annular dark field
AE	Auger electrons
AFM	atomic force microscopy/ microscope
Au	gold
BF	bright field
BSE	back scattered electrons
C	condenser lens
C-AFM	conductive atomic force microscopy
D	electron dose
DBM	dual beam microscope
DE	diffusion enhanced
DEA	dissociative electron attachment
DF	dark field
DI	dissociation ionisation
DT	dwell time
EBL	electron beam lithography
EC	environmental chamber
ED	environmental distance
EDT	Everhart-Thornley detector
EDXS	energy dispersive X-ray spectrum/spectrometer
EEL	electron energy loss
EELS	electron energy loss spectroscopy
ESE	environmental secondary electrons
ESEM	environmental scanning electron microscope
FEBID	focused electron beam induced deposition
FIB	focused ion beam
FSE	forward scattered electrons
FWHM	full width half maximum
GEA	Gas Entladungs Apperatur/ gas discharge apparatus
GIS	gas injection system
GSED	gaseous secondary electron detector
HAADF	high-angle annular dark field
HV	high vacuum
LFD	large field detector
LJ	Lennard Jones
LV	low vacuum
MCA	multi-channel analyser
MTL	mass transport limited
PLA	pressure limiting aperture
PoP	point pitch
PSD	position sensitive detector
Pt	platinum
RRL	reaction rate limited
SCL	SCL-Sensor. Tech. Fabrication GmbH
SE	secondary electrons
SEM	scanning electron microscope
SS-CL	self-sensing cantilevers
STEM	scanning transmission electron microscopy/ microscope
S-TET	specific total exposure time
TEM	transmission electron microscopy/ microscope
TLD	through-the-lens detector
t_{rel}	relative exposure time
UHR	ultra high resolution
UHV	ultra high vacuum
VdW	Van der Waals
WD	working distance

1 Introduction

Nowadays, countless fields in science and industry crucially depend on the capabilities of nanofabrication. A widely spread technique in nanofabrication is lithography with an overwhelming importance in the semi-conductor industry. While lithography is very well suited for industrial mass production, it has also downsides.

Focused electron beam induced deposition (**FEBID**) is a novel, increasingly important nanofabrication method, which can produce structures with spatial nanometer resolution[1]. This is achieved by local electron beam induced dissociation of physisorbed precursor materials injected via a fine capillary into the instruments vacuum chamber. The advantages of this technique are the mask-less direct-write characteristic, which allows fast layout changes and the production on practically any given surface. Combined with the fact that not only 2D but real free-standing 3D nano-structures can be built ("3D nanoprinting"), FEBID provides unique capabilities compared to lithography techniques. One of the limitations of FEBID technology is its limited production speed compared to lithography techniques.

For a long time, the high amount of unwanted impurities, mainly carbon stemming from incomplete dissociation of the precursor, was considered a major downside of the FEBID technique and very difficult to overcome. In 2014, B. Geier demonstrated an e-beam assisted purification approach of Pt-C deposits (from the $MeCpPt^{IV}Me_3$ precursor) in a H_2O environments, which entirely removes the carbon[2,3]. Even more important, the purified nanostructure are not only pure metallic but also pore and crack free with a minimal lateral shrink of less than 5 rel.%. and qualitatively maintained surface morphologies.

The possibility to produce pure metal deposits with FEBID is a huge capability gain for the technique and enables many new possible applications. In the frame of this thesis, the mentioned purification approach is also expanded to an Au based precursor material ($Me_2Au(acac)$), which expands the type of possible applications. In conclusion, to examine and implement selected applications for purified Pt and Au FEBID structures is the main focus of this thesis.

The aim of application for the Pt based precursor was to produce self-sensing cantilevers for conductive atomic force microscopy (**AFM**), which is a novelty for this type of cantilvers (for details see chapter 3.1.1). The objective of application for the Au based precursor was to fabricate plasmonically active nano-structures (for details see chapter 3.2.1). Both objectives were successfully achieved in the frame of this thesis.

Beside implementing these 2 applications, new insights were gained on the basic aspect of e-beam assisted purification and Au precursor deposition behaviour. These can be found in chapter 3.1 for the experiments concerning the Pt precursor and in chapter 3.2 for the experiments concerning the Au precursor. Examples for that are the development of a new post purification processing step improving the purification results (chapter 3.2.4) and a more detailed insight on the lateral shrinking behaviour during purification (chapter 3.2.5.1).

2 Instrumentation and Basics of the Used Experimental Techniques

2.1 Nanofabrication

In this chapter the nanofabrication method of focused electron beam induced deposition (**FEBID**) used during this thesis is presented.

2.1.1 Dual Beam Microscope (DBM)

A dual beam microscope (**DBM**) combines a conventional scanning electron microscope (**SEM**) with a focused ion beam (**FIB**) microscope.[4] The DBM, used during this Master thesis, is a FEI Nova 200. The ion column is thereby tilted 52° against the electron column. Because of this the specimen stage is tiltable from -15-60 degree [5], which allows to tilt the sample in such way that either the electron or the ion column is perpendicular to the sample surface. The so called eucentric height is the distance at which the optical axis of the electron and the ion column intersect. If the specimen surface is in the eucentric height, pictures of the electron and the ion column are showing the same area.

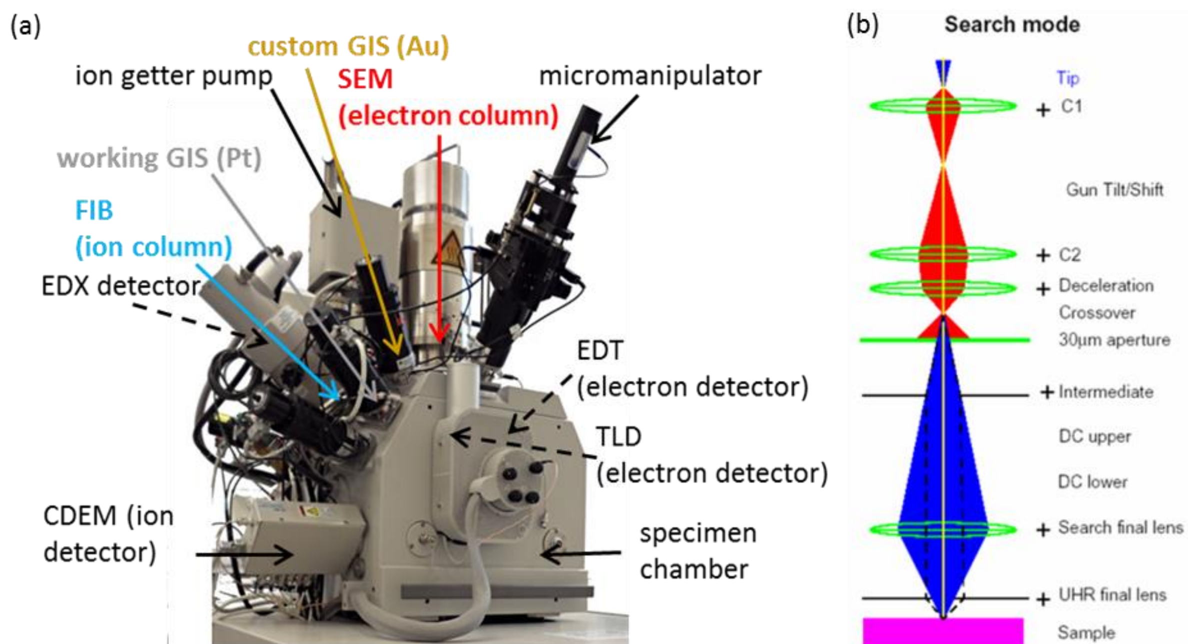

*Figure 1: (a) FEI nova 200 dual beam microscope (**DBM**) with labelling of the most important components for this thesis. Modified from [6]. A dashed arrow indicates that the component is not visible in the picture. The gas injection systems (**GIS**) for the platinum (**Pt**) precursor (working GIS) and the gold (**Au**) precursor (custom GIS) were important components for this thesis. The custom GIS was also used with the Pt precursor in the beginning. The detectors of the DBM include an Everhart-Thornley detector (**EDT**; electrons), a through the lens detector (**TLD**; electrons), channel detection electron multiplier (**CDEM**; ions) and energy dispersive X-rays (**EDX**) detector. (b) Illustration of the electron column of the FEI nova 200 dual beam microscope. A Schottky emitter emits electrons, which are focused on the sample with a lens system. The DC upper and the DC lower lens are responsible for the scanning movement of the electron beam across the sample. From [7].*

The working distance (**WD**) is defined as the distance between the specimen surface and the last pol piece of the last lens of the electron column.[8] The eucentric height for the DBM is in a WD of 5 mm. Although a smaller WD would improve the resolution, a certain distance is necessary to have enough space for the micromanipulator and the gas injection systems (**GIS**). An illustration of the DBM can be seen in Figure 1 (a).

During operation the specimen chamber needs to be in high vacuum (**HV**) state to minimize electron scattering at gas atoms.[8] The electron and the ion source need to be in the even higher ultra-high vacuum (**UHV**) and are very sensitive to vacuum loss. Vacuum in the specimen chamber is reached by a roughing pump and a turbo molecular pump. After the specimen chamber was opened, there is atmospheric pressure in the chamber. The roughing pump reduces the atmospheric pressure to a level where the turbo molecular pump can work, which reaches a much higher vacuum. For the UHV of the ion and electron source, ion getter pumps are used.

The electron column, which produces the electron beam and is labelled in red in Figure 1 (a), is in principal identical with a conventional scanning electron microscope (**SEM**). Diffraction effects limit the reachable resolution to the length of the wavelength. Thereby for light microscopes where the wavelength can't be arbitrarily reduced, the wavelength limits the reachable resolution. The wavelength of electrons (wave-particle dualism) is determined by the De-Broglie relation. The De-Broglie wavelength λ depends on the Planck constant h, the charge of the electron q, the relativistic mass of the electron and most importantly the acceleration voltage U:

$$\lambda = \frac{h}{\sqrt{2qmU}} \tag{1}$$

For an acceleration voltage of 30 keV for electrons (maximum acceleration voltage in the DBM), the wavelength would be approximately 7 pm. In practice, this resolution isn't reachable because the errors of the electron lenses reduce the reachable resolution dramatically.[8,9]

In Figure 1 (b) a schematic illustration of the electron column of the DBM can be seen. At the top, the electron source can be found. The FEI Nova 200 uses a Schottky emitter. This emitter uses both, the concept of a thermionic emitter (heating) and the concept of a cold field emitter (high electrical field intensities). The W (tungsten) tip of the Schottky emitter is coated with ZrO_2 to reduce the work function of the electron emission. The Schottky emitter reaches a much better source diameter and brightness than a thermionic source would, while its emission current is much more stable than the emission current of a cold field emitter. A Wehnelt cylinder bundles the electrons in the first cross over[8], after which they get further accelerated. Two electrical condenser lenses (C1 and C2 in Figure 1 (b)) demagnify the beam and align it with the optical axes. The deceleration crossover is used to reduce the beam energy on the desired value. A lens system (DC upper and DC lower in Figure 1 (b)) enables the scanning movement of the beam across the sample. For the ultra high resolution mode (**UHR**), which further improves the resolution, an additional lens (UHR final lens in Figure 1 (b)) is switched on. It's critical to ensure that the sample doesn't contain magnetic material when using the UHR mode, since this could heavily damage the lens system and electron column.

The ion column, which is labelled in Figure 1 (a) in blue, uses Ga^+ ions from a liquid ion metal source (**LIMS**). Ga^+ ions have a favourable low vapour pressure (unwanted losses minimized), a low melting point (easy liquefaction) and are not miscible with the tungsten, from which the ion source tip is made of. The tungsten hairpin is placed at the bottom of a Ga reservoir which is heated to liquefy the Ga. Under the gravitational influence, the liquid Ga forms a droplet on the tip of the tungsten hairpin. An extractor beneath the hairpin with a very high electric potential, deforms the droplet, which then forms the so called Taylor cone. The strong curvature at the tip of the Taylor cone leads to very high electric field intensities, which ionizes the Ga by removing a valence electron and thereby forms the Ga^+ beam. Apart from imaging, due to their high mass, Ga ions can be used to sputter sample material. Simultaneously, the SEM can be used for imaging and thereby for an *in-situ* observation of the sputtering process. A common use of the DBM at the institute is the preparation of thin lamellas (< 50nm) for transmission electron microscopy (**TEM**) using this sputtering effect.

2.1.1.1 Interactions of Electrons with Matter and Detection Mechanisms

The uninfluenced electrons in the electron beam are called primary electrons (**PE**). When they hit the surface and interact with the specimen atoms, interactions can be either elastically or inelastically.[8]

The electrons which interact elastically are scattered by a large angle, can exit the surface again and are then called back scattered electrons (**BSE**). In the Monte Carlo beam path simulation in Figure 2 (a), their trajectories are marked red. BSE have a strong material contrast because elastic scattering is more probable for high atomic numbers. BSE also have a broad energy spectrum between 50 eV and the acceleration voltage because many of them have suffered additional to the elastic scattering multiple inelastic (energy loss) scattering processes.[8,9]

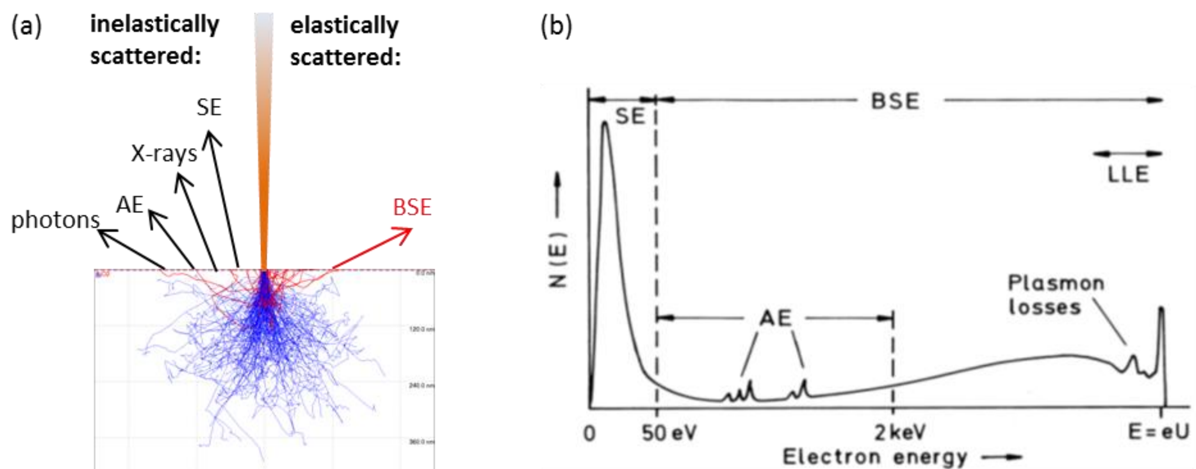

*Figure 2: (a) Illustration of the electron beam interaction with the sample including the Monte Carlo trajectories inside the sample and the detectable scattering products. Inspired by [10]. (b) Energy distribution of electrons, which exit the sample and can be detected. Secondary electrons (**SE**) have their peak at 2-5 eV. The limit between SE and back scattered electrons (**BSE**) at 50 eV is determined per definition. Auger electrons (**AE**) have material characteristic energies and can thereby be used for material characterization. Low loss electrons (**LLE**) are BSE, which have only lost a small of the primary electron (**PE**) energy, e.g. by plasmonic excitations. From [9].*

Electrons which are scattered inelastically loose a part of their energy and are deflected at low angles. This energy loss process can repeat until the electrons are stopped at a maximal depth, which is called the penetration depth. An increase of the primary beam energy increases also the penetration depth. One possible inelastic scattering process is the interaction of the primary beam electrons with upper shell electrons of specimen atoms, which results in the ejection of the upper shell electron. These electrons are called secondary electrons (**SE**), with their maximum in the energy distribution between 2-5 eV. If the secondary electrons are created by PE, they are called SE_1 (PE → SE_1). Because of their low energy, SE can only leave the specimen from a surface layer of a few nm thicknesses. However, this doesn't mean that SE are only created by the narrow beam of PE, but also in a much larger area by BSE on their way to exit the surface. SE which are caused by BSE are called SE_2 (BSE → SE_2). The last possible way to create SE are forward scattered electrons (FSE → SE_3).[8,9]

Electrons with enough energy can cause the ejection of an inner-shell electron. The refill process of this inner shell vacancy either results in the emission of a (material) characteristic X-ray photon (favourable for elements with a high atomic number) or of an Auger electron (**AE**; favourable for elements with a low atomic number). Continuum X-Rays or Bremsstrahlung are created by the deceleration of electrons in the Coulombic field of an atom[8,9]. For more information about characterization via X-rays see chapter 2.4.1.

In Figure 2 (a) the detectable scattering products in a SEM can be seen. Photons from cathodoluminescence (electron-hole recombination) in the infrared, visible or ultraviolet wavelength can be used for the characterization of minerals, semiconductors and biological specimens. Plasmon excitations (waves in the free electron gas) and the excitations of phonons (lattice oscillations, e.g. heat) are further inelastic scattering processes.[8,9] Figure 2 (b) shows the energy distribution of all kind of sample exiting electrons.

The FEI Nova 200 dual beam microscope has 2 detectors for electrons. One is the Everhart-Thornley Detector (**ETD**), which can be seen in Figure 3. The part of the ETD called collector allows the selection between SE and BSE. When the collector is positively biased, the SE which have low energies are attracted into the detector. When the collector bias is negative, electrons are generally rebelled Only BSE with their high energies can overcome this potential barrier and enter the detector. After passing the collector, the electron is accelerated towards the scintillator. Hitting the Scintillator electron-hole pairs are created, which generate light photons when they re-combine. The photons travel by fibre-optic light guides to a photomultiplier where the number of photons gets multiplied. Since, the ETD is tilted with respect to the beam axis, for electrons, which have an obstacle (barrier) in their way to the collector grid, it's much more difficult to reach the detector. The minor number of electrons, which reach the detector from these areas, make them appear darker and give the three dimensional expression of an observation from the ETD position.[8]

The second detector on the DBM is the through-the-lens detector (**TLD**). Since the TLD is above the objective lens, which the signal electrons have to pass again on their way to the detector, a high positive bias (> 10 keV[8]) has to be applied to attract SE. The magnetic field in the objective lens forces them on spiral trajectories. BSE with their high energy stay uninfluenced, can't reach the TLD and thereby can't be detected with it.[8]

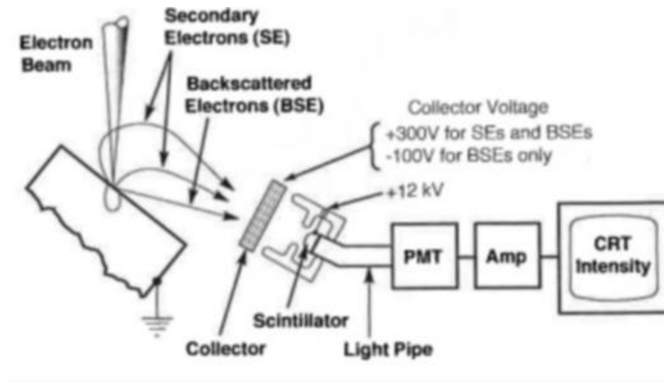

*Figure 3: Everhart-Thornley Detector (**ETD**). From [8].*

2.1.2 Focused Electron Beam Induced Deposition (FEBID)

2.1.2.1 Concept

Focused Electron Beam Induced Deposition (**FEBID**) is a direct-write bottom-up nanofabrication method with true 3D capabilities ("3D printer on the nanoscale"). Typically, this technology is executed in the vacuum chamber of a SEM/FIB, where gaseous precursor molecules are injected via the gas injection nozzle and are dissociated by the electron beam into volatile and non-volatile parts. The non-volatile parts adhere to the surface and thereby form a deposition. (see Figure 4).[1]

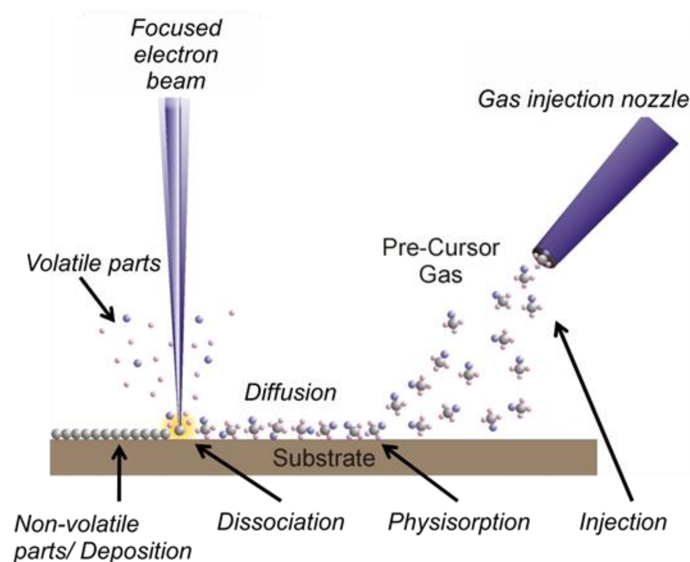

Figure 4: FEBID/FIBID operating principle. From [10].

Figure 4 shows a schematic illustration of the FEBID/FIBID operating principle: The microscope has to be equipped with a gas injection system (**GIS**). The GIS contains the precursor material with a relative low sublimation or evaporation temperature. By heating the precursor slightly above this

temperature, a certain amount of precursor molecules goes into the gaseous phase. The gas injection nozzle is brought closely to the specimen surface and the scanning area. When the valve of the nozzle is opened, gaseous precursor molecules are permanently injected into the chamber. The molecules physisorb on the substrate surface, diffuse around and desorb again randomly. The mean residence time on the surface depends on parameters related to the substrate and precursor. When the electron or ion beam hits the physisorbed precursor molecules, the molecules are dissociated into a non-volatile part, which forms the deposit by remaining on the surface, and a volatile part, which gets pumped away.[1]

The advantages of FEBID are (1) the direct-write approach allowing (2) depositions to the nanoscale with (3) fast layout changes, (4) the capability to deposit on almost any, even on non-flat surface, (5) the lack of special preparation or follow-up procedures and finally (6) the capability to deposit freestanding 3D structures.[11] The downside of the FEBID technique is, beside the broadening of the structures[12], the poor purity of the deposited material. Usually metal-organic precursor molecules with large amounts of carbon are used. In this metal organic precursor molecules, the metal atom sits in the centre of the molecule and organic compounds, the so called ligands, are bound with its valence electrons. The ligands are the molecule parts responsible for the volatility of the precursor. Often the deposit of such precursors is described as a carbon matrix with only small metal content (5-30 at.%)[13]. In order to receive a pure metal deposit, all the ligands must be dissociated from the metal atom and removed from the deposit. As the electrons have a vast energy range (see Figure 2 (b)), the bond splitting is not selective and different types of dissociation products are created.[1]

2.1.2.2 Dissociation Mechanism for Absorbed Precursor Molecules

As mentioned, adsorbed precursor molecules are dissociated because of electron impingement, which provides the necessary energy to overcome the binding barrier. As demonstrated by Arnold et.al.[14], a strong indication for a SE dominated deposition process is that the beam of PE can be focused with nanometre resolution. Therefore, if PE and descending SE_1 were mainly responsible for the deposition, FEBID should have a nanometre resolution limit. This is not the case and it could be shown that BSE and SE_2 contribute significantly to the deposition process.

Engmann et.al.[12] came to the same conclusion that mainly SE contribute to the deposition process due to favourable cross sections for them. The two main dissociation processes are dissociative electron attachment (**DEA**) and dissociation ionisation (**DI**):

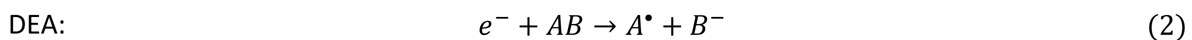

DEA: $$e^- + AB \rightarrow A^\bullet + B^- \tag{2}$$

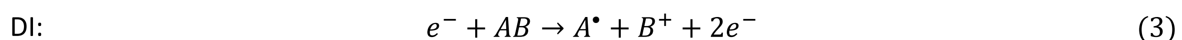

DI: $$e^- + AB \rightarrow A^\bullet + B^+ + 2e^- \tag{3}$$

The dots indicate free valence electrons. DEA induces, dependant on the precursor, mainly incomplete segregation of the ligands from the central metal atom, which leads to the large amount of non-metal compounds in the deposit. Although, DEA processes work only in a narrow energy

range (1 – 5 eV), this overlaps very well with the maximum of the SE energy distribution. Because DI processes have usually a binding barrier of around 10 eV to overcome and therefore overlap only with the tail of the SE energy distribution, the DEA mechanism dominates over the DI mechanism. The PE contribution to the dissociation process is negligible, since the cross section is too low.[1,12,15]

2.1.2.3 Working Regime

An important aspect concerning FEBID depositions is the working regime. The working regime describes the balance between the number of dissociation causing electrons and the number of precursor molecules available for the dissociation process. It can be distinguished between 3 deposition conditions: [1,11,16]

- Reaction rate limited (**RRL**): There is an excess of available precursor molecules compared to the dissociating molecules, which results in an incomplete separation of the metal atoms and the ligands (see Figure 5 (b)) leading to an incorporation of the latter ones.[1,11,16]
- Mass transport limited (**MTL**): There is an excess of dissociating electrons compared to available precursor molecules, which leads to a polymerization (see Figure 5 (c)) and incorporation of the ligands in metal-organic precursors.[1,11,16]
- Diffusion enhanced (**DE**): This regime lies in between the two extremes of too many precursor molecules (RRL) and too many dissociating electrons (MTL). All the molecules within the deposition spot (SE_1 and SE_2) are dissociated but molecules from the proximity of the deposition spot, can replenish the loss by diffusion.[1]

However, the models above are a simplification of the real situation as they assume constant surface coverage of the precursor molecules and neglect replenishment conditions and directional components like topographical features or deposition strategies.[16,17]

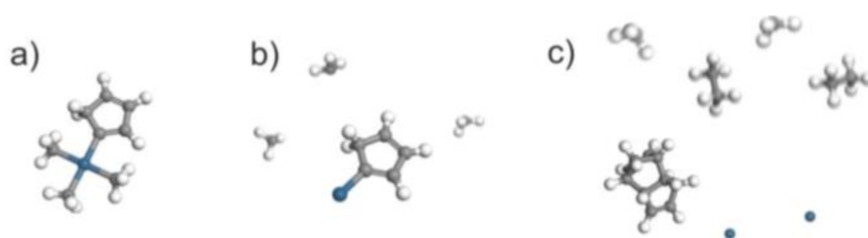

Figure 5: $MeCpPt^{IV}Me_3$ precursor (a) in its native form before deposition, (b) partially dissociated form as it appears for RRL conditions and (c) complete dissociation of the ligands from the Pt atom including polymerized organic compounds, like it occurs for the MTL deposition regime. Blue coloured atoms are Pt atoms, grey coloured ones are carbon atoms and the white coloured ones represent hydrogen. All from [10].

2.1.2.4 FEBID Deposition Parameter

There are many different influences on the result of the deposition process, some of which are hard to predict. For example, different precursor coverages originating from differently strong precursor gas flows from the nozzle, the nozzle distance from the deposition site (see chapter 2.1.2.7) or simply topographical obstacles for the precursor supply.

The electron beam parameters for the deposition are the primary beam energy, beam current, dwell time (**DT**), point pitch (**PoP**), number of passes, an eventual defocus setting and the patterning strategy. Depositions, which are referred as "pad" below, have simply a square or rectangular footprint and are usually deposited with multiple passes to reach the desired target height. All pads were fabricated with the serpentine patterning strategy, which can be seen in Figure 6 (a) and results in the best deposition quality[6]. The direction of the precursor gas flow has to be chosen in such a way, that already deposited lines of the deposition pattern don't act as gas flux barriers (geometrical shadowing effect[6]) for still to be deposited lines.

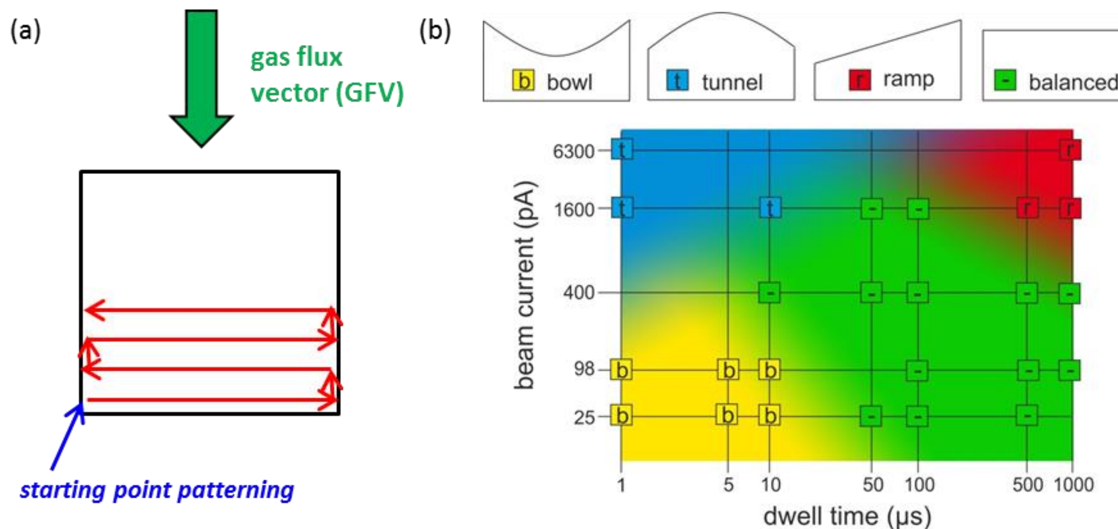

Figure 6: (a) serpentine patterning strategy for a square pad with the optimal direction of the precursor gas flux (gas flux vector) in relation to the serpentine direction. This prevents, that already deposited lines act as gas flux barriers (geometrical shadowing effect) for still to be deposited lines. (b) Morphological shape (colour interpretation see the top row of) of $2 \times 2\ \mu m^2$ pads in dependence of the beam current and the DT deposited with 5 keV, 1000 µs DT and serpentine patterning strategy using the custom GIS filled with the $MeCpPt^{IV}Me_3$ precursor. From [6].

Usually, height calibration experiments were done in advance to evaluate deposition rates for pads with desired heights. The primary beam energy, beam current, DT and PoP were usually kept constant. The height of a deposition was then directly determined by the number of passes. We also introduced a new unit called the relative exposure time (**t_{rel}**), which measures the amount of e-beam radiation:

$$t_{rel} = \frac{t \cdot I}{A} = \frac{DT \cdot n \cdot I}{PoP} \qquad [t_{rel}] = \frac{min \cdot nA}{\mu m^2} \tag{4}$$

t_{rel}	...	relative exposure time	
t	...	exposure time	min
I	...	electron beam current	nA
A	...	scan frame size	μm^2
DT	...	dwell time	min
n	...	number of passes	
PoP	...	point pitch	μm^2

t_{rel} is actually, apart from the used units, equivalent with the electron dose (unit for the electron beam irradiation) already introduced by B. Geier et.al.[2,3] for the purification. While the dose is given in charge per area (usually C/cm^2), the relative exposure time t_{rel} still contains the time in explicit units which makes it easier to calculate processing times directly. For depositions only t_{rel} was used. For more details about the dose and unit conversion see chapter 2.2.2.2.

As Figure 6 (b) demonstrates, the influence of the beam current and the dwell time (DT) on the morphology shape of the deposited pad. The other parameters of the deposition, 5 keV beam energy, 1000 µs Total Exposure time, serpentine patterning strategy and *custom GIS* filled with $MeCpPt^{IV}Me_3$ were kept constant.[6]

For single line depositions, since the beam energy and the current were usually constant, the so called specific total exposure time (**S-TET**) was chosen containing dwell time (DT) and the number of passes (n) summing up to the total exposure time (TET), divided by the point pitch (PoP):

$$S\text{-}TET = \frac{TET}{PoP} = \frac{DT \cdot n}{PoP} \qquad [\, S\text{-}TET \,] = \frac{ms}{nm} \tag{5}$$

2.1.2.5 Adsorption Rate Model

4-key processes determine the surface density n(r,t) of adsorbed precursor molecules. The change over time of the surface density is described by the adsorption rate model[18–20]:

$$\frac{\partial n(r,t)}{\partial t} = \underbrace{sJ\left(\frac{n(r,t)}{n_0}\right)}_{adsorption} - \underbrace{\frac{n(r,t)}{\tau}}_{desorption} - \underbrace{\sigma \cdot f(r) \cdot n(r,t)}_{dissociation} + \underbrace{D\left(\frac{\partial^2 n(r,t)}{\partial r^2} + \frac{1}{r}\frac{\partial n(r,t)}{\partial r}\right)}_{diffusion} \tag{6}$$

n(r,t)	...	number of adsorbates in dependence of place (r) and time (t)
s	...	sticking probability at an empty surface without adsorbates
J	...	precursor flux
n_0	...	number of molecules in a complete monolayer
τ	...	average residence time before desorption of an adsorbate
σ	...	net cross-section of the adsorbates
f(r)	...	local intensity distribution of the electron beam
D	...	surface diffusion coefficient of the adsorbates

(6) describes that at a certain location the surface density of adsorbed precursor molecules can be either reduced by a normal desorption process after an average residence time τ or by dissociation (deposition) of (some) adsorbed precursor molecules. The latter is dependent on the net cross-section σ, the local intensity of the electron beam f(r) and the surface density of the adsorbates n(r,t). The surface density of the adsorbates can be replenished by two processes: Either by the new adsorption of precursor molecules, which depends on the sticking coefficient s, the precursor flux and the amount of free places for adsorption ($n(r,t)/n_0$) or by diffusion from other places on the substrate with higher adsorbates surface density, which is mainly determined by the surface diffusion coefficient. As Szkudlarek et.al[20] demonstrated for high currents where a a big part of the initial surface density of adsorbates is depleted by the electron beam, the influence of the diffusion is orders of magnitudes larger than the influence of the adsorption, if the surface diffusion coefficient D is large. [18–20]

2.1.2.6 Precursor Material

The precursor material has to fulfil several requirements, e.g. physisorb to the surface, a favourable sublimation or evaporation temperature and the expected dissociation process.[1]

For platinum (**Pt**) based depositions, the trimethyl(methycyclopentadienyl)platinum^{IV} ($MeCpPt^{IV}Me_3$) precursor, which is referred to as “Pt precursor” below, was used (see Figure 7 (a)). The untreated deposits of the Pt precursor contain in dependence of the deposition parameters only approximately 15 at.% Pt[21]. At least several minutes before and during deposition the precursor was heated to 45°C.

Dimethylgold^{III} acetylacetonate ($Me_2Au(acac)$) was used for the gold (**Au**) depositions and is referred to as “Au precursor” below (see Figure 7 (b)). The untreated deposits contain approximately 8 at.% Au[21]. At least several minutes before and during deposition, the precursor was heated to 30°C.

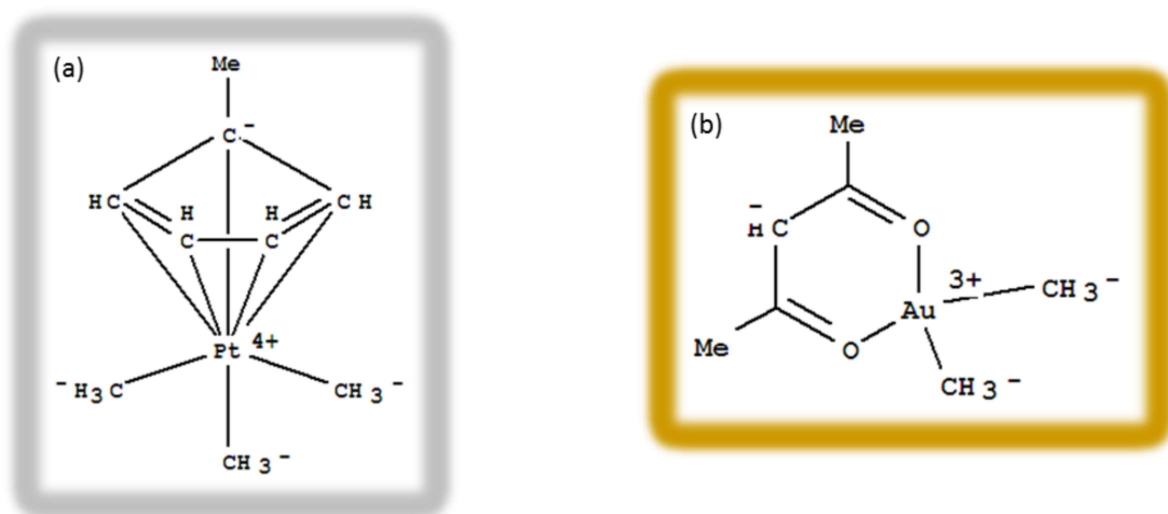

Figure 7: (a) Structure formula of the trimethyl(methycyclopentadienyl)platinum^{IV} ($MeCpPt^{IV}Me_3$) precursor. From [22]. (b) Structure formula of the dimethylgold^{III} acetylacetonate ($Me_2Au(acac)$) precursor. From [23].

2.1.2.7 Positioning of the Gas Injection Nozzle

2 GIS were used during the experiments described below. The so-called *custom GIS* and the *working GIS*. At the beginning both GIS systems were loaded with the Pt precursor. The GIS position for the Pt-C depositions in relation to the centre of the electron beam can be found for the *custom GIS* in Figure 6 (a) and for the *working GIS* in Figure 6 (b). The position of the *custom GIS* after it was filled with the Au precursor can be found in Figure 8 (c). If only single structures were deposited, the location of the deposition was the e-beam centre. For arrays of structures this was not possible anymore but the array was placed in such a way that the single structures are as close as possible to the e-beam centre.

The exact position of the GIS system is important, because it influences the gas flux and thereby the surface density of the adsorbed precursor molecules at the deposition location and consequently also the deposition result.

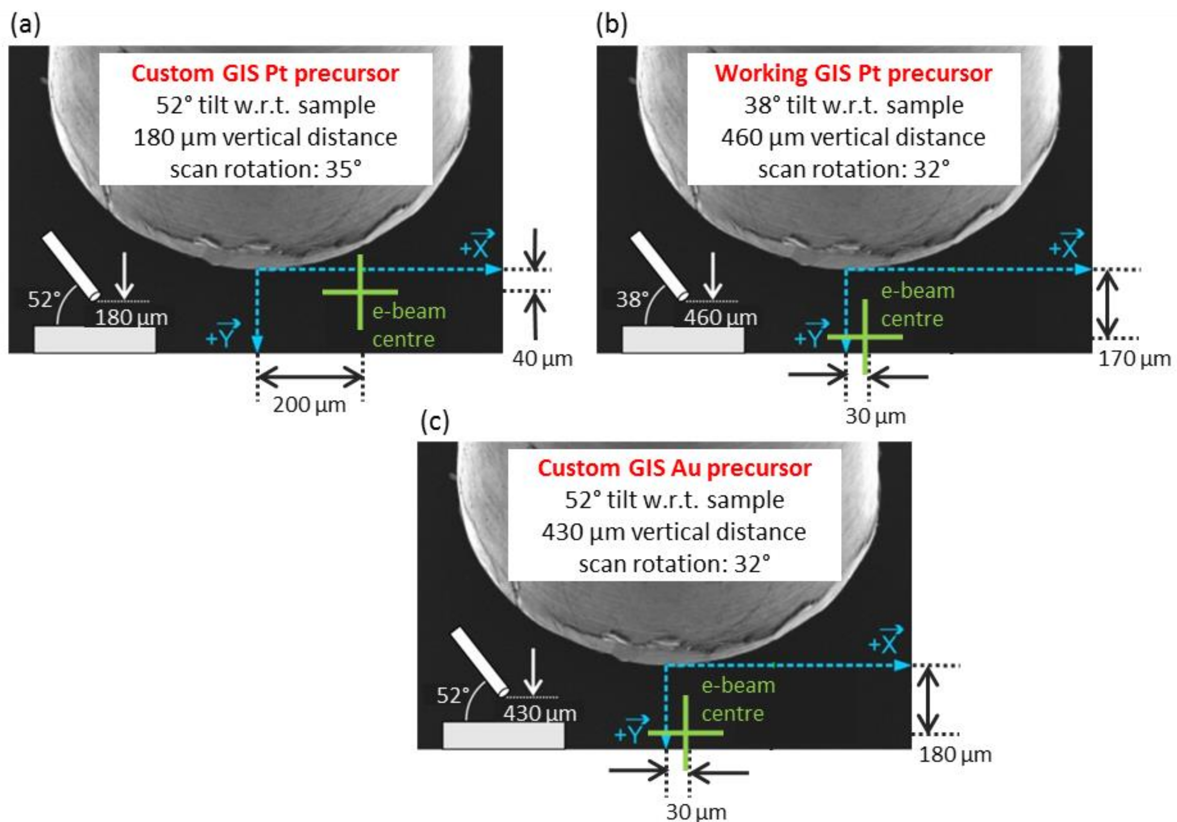

Figure 8: Different gas injection nozzles and their positions in relation to the centre of the electron beam. The depositions locations were as close as possible to the centre of the e-beam. (a) nozzle position of the custom GIS filled with the Pt precursor, which was only the case at the beginning of the experiments . (b) nozzle position of the working GIS with the Pt precursor (c) nozzle position of the custom GIS filled with the Au precursor. All modified from [6].

2.2 Purification

The term purification describes the removal of the carbon from the metal-carbon deposits leaving over only the metal parts of the deposition. To achieve that, the FEBID deposits were exposed to H_2O vapour of several Pascal in combination with electron beam irradiation in an environmental scanning electron microscope (**ESEM**). For the purification the FEI Quanta 200 ESEM was used.

2.2.1 Environmental Scanning Electron Microscopy (ESEM)

For operation a SEM requires a high vacuum suitability of the sample. The sample needs to be clean, dry and electric conductive. The conduciveness is necessary because otherwise the impinging electrons would be implanted into the sample and lead to local charges. This disturbs the imaging electrons. Various preparation techniques have been developed to make difficult samples suitable for SEM. However, these techniques have the disadvantage that they severely modify the sample and are not suitable for certain tasks.[24]

Environmental scanning electron microscopes (**ESEM**) allow operation at much higher pressures of up to several thousand Pa with various gases like for example H_2O vapour. This allows the examination of wet samples (biologic samples) without preparation. Samples, which usually would outgas in a SEM environment and samples which are dirty or oily can be investigated. Filigree specimen, which are destroyed by the sample preparation and *in-situ* heating of the sample are further possible application. For insulating samples the gas ionization in the sample chamber eliminates the typical charging artefacts.[24]

The basic construction principles are the same of ESEMs and SEMs but ESEMs have additional vacuum systems, which allow them to the operation at high pressures. The vacuum system is divided into five stages with decreasing pressure from the sample chamber to the gun chamber (Figure 9 (a)). The critical elements, which allow the large pressure differential, are 2 pressure limiting apertures (**PLA**) in the final lens of the microscope (Figure 9 (b)). Because of that, the electrons travel only a short distance through areas with high pressure, which reduces unwanted scattering effects. At the short distance between the sample chamber and the electron column, the pressure is reduced by the factor 10^{-6}.[24]

The FEI Quanta 200 ESEM, which was used for the purification process, uses a thermionic electron source made out of tungsten. Since the ETD (see chapter 2.1.1.1) can't work at the high chamber pressure, specialized detectors are needed. Both, the environmental secondary detector (**ESD**) and the more advanced gaseous secondary electron detector (**GSED**) are located concentric with the beam at the bottom of the pole piece. However, since an X-ray cone was used to optimize the EDX signal (see chapter 2.4.1) and reduce the environmental distance (**ED**), this detector types weren't used. The large field detector (**LFD**), which is located behind the electron column, can only work in the low vacuum (**LV**) range from 10 to 130 Pa which limits the pressure range. All 3 detectors use the same working principle. The detectors represent electrodes at which a positive potential of a few hundred volts is applied. When electrons, mainly SE, are accelerated toward the detector by the field, they collide with gas molecules and create additional electrons, which are themselves also forced on an accelerated trajectory toward the detector and create further electrons. This cascade

amplifies the original secondary electron signal. The ions of the signal amplification process are attracted to the sample surface and compensate the charge there, which also allows the usage of nonconductive specimen.[24,25]

In order to measure the current of the electron beam, a simple Faraday cup can be used in HV. In lower vacuum modes, the ions created in the amplification process would recombine at the Faraday cup leading to a positive specimen current and disturb the measurement. Thereby during the master thesis of H. Fitzek[26] a Faraday cup allowing the current measurement in a gaseous environment was developed and built after the design of Fletcher et.al.[27]

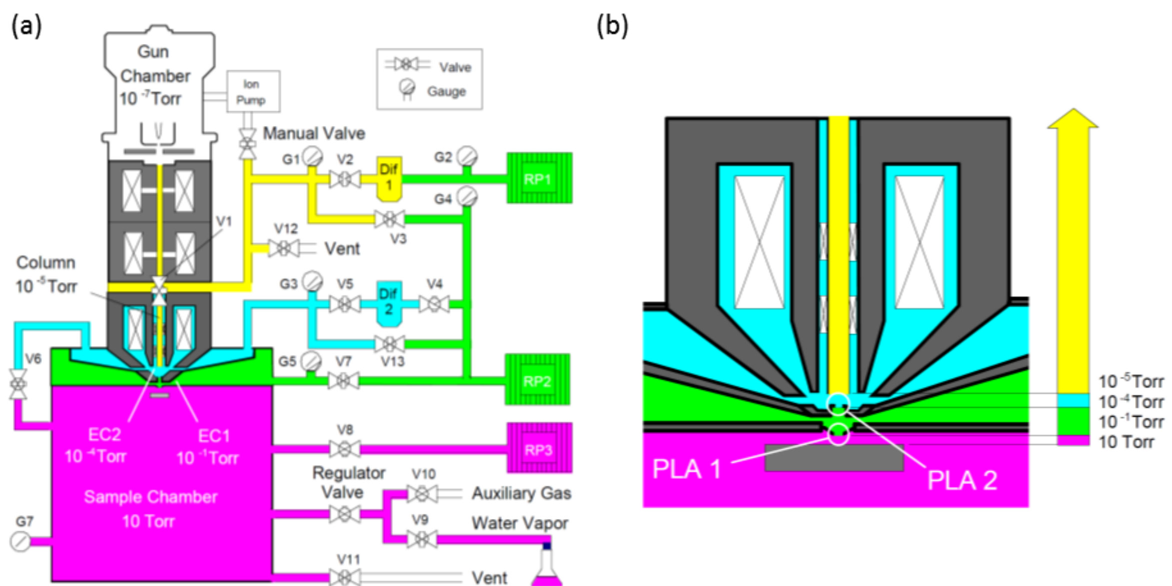

*Figure 9: (a) Illustration showing the 5 areas with different pressures inside an ESEM. Following the pressure decrease, they are the sample chamber, the 1st environmental stage (**EC1**), 2nd environmental stage (**EC2**), the column and the gun chamber (b) Enlarged area of the final lens assembly with 2 pressure limiting apertures (**PLA**) closely spaced, which allows the large pressure differential. Both from [24].*

2.2.2 The Process of Purification

The electron beam assisted purification of Pt-C deposits in H_2O vapour at room temperature was first done by B. Geier et.al. in 2014[2,3]. The supposed mechanism is that, initiated by secondary electrons (SE), atomic H and O is formed which binds to the C in the deposit. The new formed molecules are volatile and can gas out.

After the fabrication in the dual beam microscope, the samples were moved to the Quanta 200 ESEM, whose EDXS system was used for *in-situ* and *ex-situ* EDX characterization (see chapter 2.4.1). Initially the chamber was evacuated to the HV state and after selecting the primary beam energy, basic alignments were made and the target area for purification was selected. The rectangular scan frame was in detail selected with a so called “F7-window”, which allows fast adjustment in case drift movements appear during the purification process. The dwell time (DT) was selected via the scan

speed. The point pitch (PoP) could be influences via the magnification and the number of pixel of the scan frame (note that the scan speed and the number of pixel set in the microscope interface are always for the whole window and not the small “F7-window”). The intended beam current was selected via setting the spot size. The beam current measured by the simple Faraday cup only suited for HV and a Keithley 6485 picoamperemeter. Then the pressure was switched to LV.

2.2.2.1 Influence of the Scattering Effect on the Purification Current

This chapter deals with the question, how much the electron beam current reaching the deposit is reduced due being scattered by the chamber molecules.

The environmental distance (**ED**) is defined as the distance from PLA1 to the sample or as the working distance from the last pol piece to the sample (**WD_{samp}**) minus the working distance from the last pol piece to PLA1 (**WD_{PLA1}**):[3,26]

$$ED = WD_{samp} - WD_{PLA1} \tag{7}$$

Since WD_{samp} was chosen to be 11 mm to have optimal conditions for the EDX system and the height of the X-ray cone, which represents PLA1, is 8 mm, the ED is reduced to 3 mm.

The so called stagnation gas thickness (θ) takes the ED and the pressure gradient in the X-ray cone (between PLA1 and PLA 2) into account:[26]

$$\theta = ED + \Delta \tag{8}$$

Δ	…	additional stagnation gas thickness	$(3 \pm 1) \cdot 10^{-3}$ m ([26])

The additional stagnation gas thickness (Δ) was derived from the measured results from H. Fitzek’s master thesis[26] for a GSED having the same aperture size as the X-ray cone and being therefore very well comparable. In the LV conditions of the chamber, the average number of scattering events per electron is given by the following relation[28]:

$$m = \frac{\sigma(U)}{kT} p\theta \tag{9}$$

m	…	scattering events per electron	
σ(U)	…	total scattering cross section	3.88×10^{-21} m² ([29])
k	…	Boltzmann constant	1.38×10^{-23} J/K
T	…	gas temperature	296 K
p	…	Pressure	10 Pa and 100 Pa
θ	…	stagnation gas thickness	$(6 \pm 1) \cdot 10^{-3}$ m

For the total scattering cross section of H_2O, the values measured by Rattenberger et.al.[29] were used. The current resulting from all unscattered electrons can be received with the equation[28]:

$$I = I_0 \cdot e^{-m} = I_0 \cdot e^{\frac{\sigma(U)}{kT} p \theta} \tag{10}$$

I	…	unscattered electron current
I_0	…	total current in HV

Under the assumption that only unscattered electrons reach the deposit and can contribute to the purification, using (8), (9) and (10) at 10 Pa, (94.0 ± 1.5) rel.% of I_0 stay unscattered, while for 100 Pa only (56.5 ± 5) rel.% stay unscattered. B. Geier reported in her master thesis a measured current of (80 ± 3) rel.% of I_0 at 10 Pa, while for 100 Pa (50±3) rel.% were reported to remain.[3] While for 100 Pa the values fit very well, for 10 Pa they don't. Using the value of 80 rel.% measured by B. Geier to calculate the additional stagnation gas thickness an very high value of Δ ≈ 20 mm is received. This seems highly unrealistic. The Δ of the X-ray cone should be quite similar to Δ ≈ 3 mm of the GSED with the same aperture opening (see [26]) and not 7 times higher. Also measured I/I_0 ratios suggest that the better fitting value for the unscattered current is (94.0 ± 1.5) rel.%.[26] Because all the purifications were made with 10 Pa, the current set in vacuum was not corrected since the difference is small and the exact value needs further investigation. However, the strong pressure influence makes the comparability for different pressures difficult. Also it has to be mentioned that lower beam energy leads to more scattering and vice versa.[26]

Monte-Carlo simulations demonstrated that even for a H_2O pressure of 100 Pa and the scanning movement over a scanning frame of 4 x 3.5 µm², the scattered e-beam contributes nearly equal to every point of a potential 2 x 2 µm² pad in the centre of the scan frame.[3]

2.2.2.2 Relative Exposure Time and Equivalent Used Units

Similar as for the deposition in chapter 2.1.2.4, the relative exposure time (t_{rel}), which can be found in equation (4), was used to measure the electron beam irradiation. As already said above, this relative exposure time, which contains the current and the time explicitly and therefore makes calculations of the fabrication time easier, is equivalent to the dose, which was already used by B. Geier et.al.[2,3]. The electron dose (D), which is the impinged charge per cm²:

$$D = \frac{I \cdot t}{A} \qquad [D] = \frac{C}{cm^2} = \frac{A \cdot s}{cm^2} \tag{11}$$

D	…	dose	
I	…	Electron beam current	A
t	…	exposure time	s
A	…	scan frame size	cm^2

To ensure comparability with the results of B. Geier et.al[2,3] both units are used in this thesis. Usually diagrams in this thesis show the carbon decrease during the purification by using both units on two x-axes, relative exposure time t_{rel} on the lower x-axis and the dose D on the upper x-axis. Both units can be easily transferred into each other by the equation below if the standard units mentioned in equation (4) and equation (11) are used, which is always the case in this thesis:

$$D = 6 \cdot t_{rel} \qquad [D] = \frac{C}{cm^2} \qquad [t_{rel}] = \frac{min \cdot nA}{\mu m^2} \tag{12}$$

Which one is to be used in a certain moment is a matter of preference. t_{rel} is more practically to estimate the required purification from e.g. a diagram, since the numbers stay in a scale easier hand able.

2.2.2.3 Purification – State of the Art

The purification strategy using e-beam assisted purification in H_2O vapour was first introduced by B. Geier et.al.[2,3] for the $MeCpPt^{IV}Me_3$ precursor. Pad shaped deposits, single lines and free standing nanopillars were successfully purified. It was revealed by ESEM EDXS analysis and STEM-EELS, that purified deposits were totally carbon free, while in as-deposited layers Pt grains of 2-3 nm diameter were embedded in a carbon matrix (Figure 10 (a)). TEM investigations also showed that the purification is a bottom-up process – the first layers to be purified are the bottom ones and then moving upwards more and more layers get fully purified (Figure 10 (b)). This suggests an inwards diffusion of water molecules into the deposit where they are reacting under the initiation of low energy SE due to their large cross section. The carbon can leave the structure via binding to H and O atoms and forming volatile CH_X, CO_2 and CO molecules. After full purification the carbon was removed, the grain size was grown to 6-9 nm and had a widely dense composition (Figure 10 (c)).[2,3]

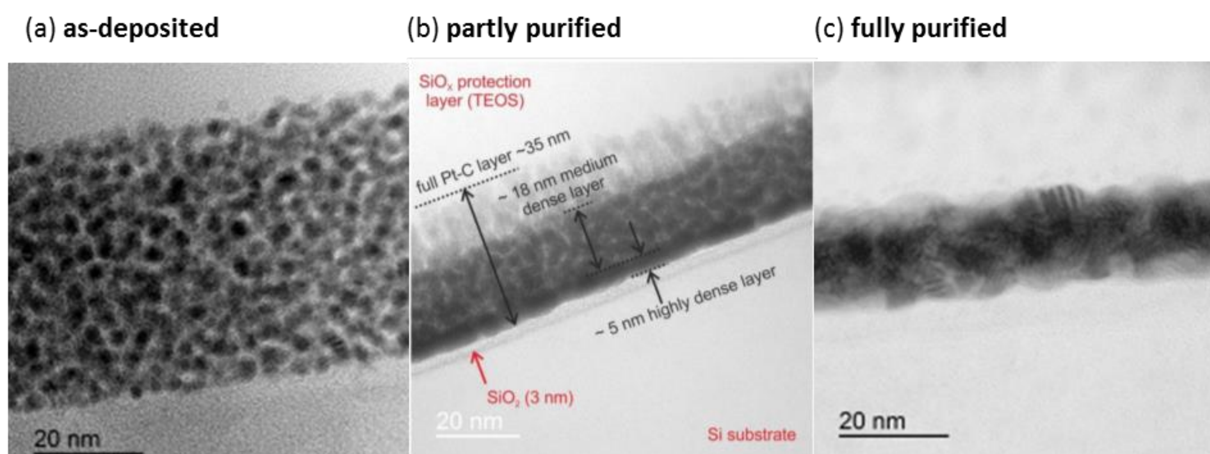

Figure 10: TEM BF images of (a) an as-deposited layer of the $MeCpPt^{IV}Me_3$. Pt grains appear as dark dots embedded in a bright carbon matrix. (b) a partly purified layer showing that the purification process is a bottom-up process and (c) a fully purified layer of the deposit. All from [3].

For pads it was shown that the purifications for 10 and 100 Pa took course in the same way and showed similar results. AFM examinations revealed a volume loss of (69 ± 3) vol.% fitting very well to the theoretical expectations of 70 vol.% loss. The fully purified deposit was pore and crack free while the footprint shape showed only a small lateral shrink of 4 nm. Single lines showed a height loss in the range of 55 rel.% and only a minimal shrinking of the of the single line base width. The RMS surface roughness of the lines slightly increased from 0.5 to 1.3 nm. Free standing nanopillars where purified with 100 Pa to profit from the strongly increased scattering. By that, more electrons are able to enter the pillar from the side. For high pillars the shrink occurs vertically, while for very low pillars the shrink occurs laterally.[2,3]

2.3 Plasma Cleaning

Plasma cleaning is generally applied to remove contaminations and impurities such as hydrocarbons from sample surfaces. In the frame of this thesis it was used to remove contaminations at the edge of the purification scan frame as the last processing step. Different gases can be used in a low pressure environment. The plasma is created by using high frequency voltage, which excites the gas into higher energy states. A plasma contains molecules, ions, electrons, free radicals, atoms and photons from the visible range (oxygen plasma emits blue light) up to short wave ultraviolet (**UV**). While the UV radiation breaks effectively organic bonds of contamination molecules, the plasma species, e.g. for oxygen O, O^+, O^-, O_2^+, O_2^-, O_3, react with them and form CO, CO_2, H_2O, acids and esters. These reaction products are volatile and get pumped away by the vacuum system.[30,31]

2 different plasma cleaners were used during this thesis:

- Gas discharge apparatus (**GEA** – Gas Entladungs Apperatur), which was constructed by the institute and is also used for metal coating via sputtering. The used gas is pure oxygen. This was the standard apparatus since the chamber is large and the samples are not limited in size.
- Model 1020 Plasma Cleaner of Fischione Instruments for TEM samples and sample holders. This plasma cleaner uses 25 vol.% oxygen and 75 vol.% argon and the samples are limited by the size of the TEM sample holder[32].

2.4 Characterization

In this chapter, the methods used to characterize the chemistry, the morphology, the inner structure and the resistivity of the purified but also as-deposited deposits are presented. Also the method to observe the plasmonic modes in FEBID produced Au discs is presented

2.4.1 EDXS

Both the FEI Quanta 200 ESEM and the FEI Nova 200 DBM have energy dispersive X-ray spectrometers (**EDXS**). While the ESEM is using a Si(Li)-detector (XL-30 EDXS system; EDAX; USA), the FEI Nova 200 is equipped with a silicon drift detector (**SDD**), which has a better count rate capability

and energy resolution compared to the ESEM detector. Energy dispersive X-ray spectra (**EDXS**) can be used to evaluate the purification progress and success [3]. If not specified differently, the EDXS data in this thesis were gained with the ESEM Si(Li)-detector.

X-rays are created by the interactions of the primary electrons of the microscope with the sample. There are two types of X-rays, which differ in the way they are generated (see Figure 11): The first type is the Bremsstrahlung (X-ray continuum), which originates from a deceleration of the primary electrons as a result of inelastic scattering. [9]

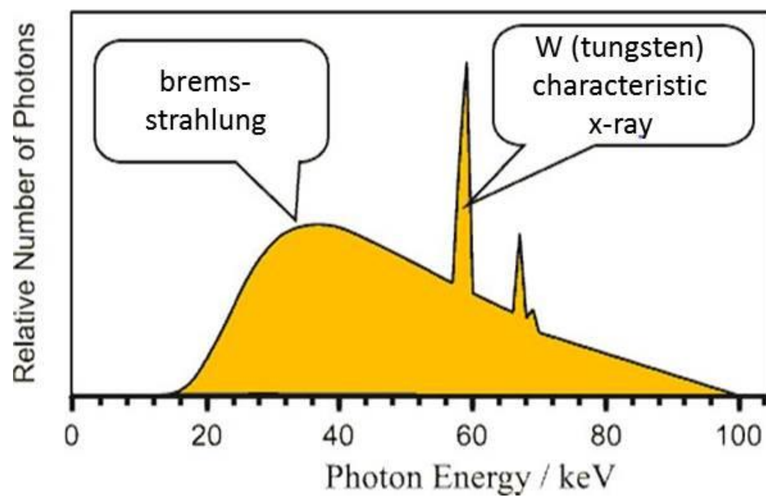

Figure 11: Calculated X-ray Spektrum for 100 keV primary beam energy for a W (Tungsten) target at 13° angle. Both the characteristic X-ray radiation and the Bremsstrahlung can be seen. Modified from [33].

The other type, which is the essential one for material analysis, are the characteristic X-rays lines, which are generated when primary electrons knock out inner shell electrons of the atoms of the examined material (ionization). This vacancy is filled by atomic electrons from outer shells. In this case a characteristic X-ray quantum can be emitted whose energy is equal to the de-excitation energy, which is the difference between the energies of the initial and the final states (see Figure 12). If there isn't a characteristic X-ray photon created, the de-excitation energy is directly transferred to an atomic electron, which then leaves the atom as an Auger electron. The characteristic X-ray lines can be classified in series according to the shell in which the ionization took place. The Latin letter on first position represents the initially ionized shell (K, L, …), while the Greek letter with an Arabic number as subscript on second position represents the shell of the electron, which fills the vacancy. For example $K\alpha_1$ indicates a vacancy position in the K shell, which is filled by an electron from the $L_3(2P_{3/2})$ shell (see Figure 12). The allowed transitions have to fulfil the selection rules $\Delta l = \pm 1$, $\Delta j = 0, \pm 1$.[9]

The width ΔE_x of X-ray lines is linked to the life time of the energy state by Heisenberg's uncertainty relation: $\tau \Delta E_x = \hbar$. From that follows that the lifetime τ of a state is inversely proportional to ΔE_x :

$\tau \propto \Delta E_x^{-1}$. However, this is a factor which doesn't influence the EDXS analysis in practice because the energy resolution of Si(Li) detectors (> 100 eV) is way larger than the natural line width. [3,9]

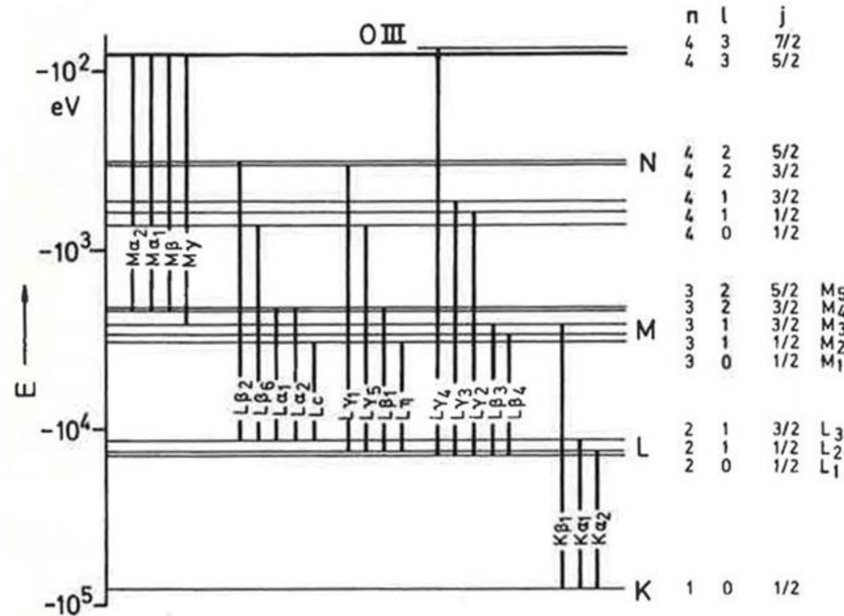

Figure 12: Energy levels of atomic shells in Au on a logarithmic scale and the nomenclatura of the subshells with quantum numbers n, l and j. Also there can be seen the possible transitions, which result in characteristic X-rays, and their classification. From [9].

Three different interactions of X-rays with matter have to be taken into account and contribute to X-ray absorption: elastic scattering, inelastic scattering and photoelectric absorption. In case of a quantitative analysis X-ray adsorption has to be taken into account.[9]

The intensities of the X-ray lines depend, in addition to the material composition, on the ionization cross section and the ionization probability which are summarized as X-ray yield (or fluorescence yield). The Auger yield indicates the complementary probability to the X-ray yield for a radiation less transition. As can be seen in Figure 13 (a) the X-ray yield is low for small atomic numbers and large for high atomic numbers while for the yield of Auger electrons it's exactly contrariwise. Therefore, absolute quantification of light elements as carbon and thin layers via EDXS is difficult and leads to strong uncertainties.

This situation is given for the Pt-C or Au-C deposits used in this thesis. To be able to evaluate the progress and the result of the purification process in the ESEM (see chapter 2.2.1) a semi-quantitative approach using relative C/Pt ratios was used[2,3,34,35]. In Figure 13 (b) the EDX spectra of an as-deposited Pt-C pad, a fully purified (5 keV) Pt pad and a spectra of the SiO_2/Si substrate (Si-wafer) can be seen. The as-deposited Pt-C spectra has a high peak around 250 eV, which contains mainly the C-K line but also the Pt-N line (originating from the deposit) and Si-L line (originating from the substrate). Therefore, using only the EDXS information around 250 eV, which stems from all 3 elements, wouldn't be sufficient to receive detailed information about the carbon content. To

calculate the C/Pt ratio, first the substrate spectrum is subtracted from the deposit spectrum to cancel out the background information in the spectrum. In the following step the value of the intensity integration from 120 – 330 eV (C-K and Pt-N, for simplification denoted as C-peak) is divided by the value of intensity integration from 1950 – 2220 eV (indicated as Pt-peak) to receive the semi-quantitative C/Pt ratio. For the Au precursor the same principle was used (for more details see chapter 3.2.3). To simplify the work for this calculations a Matlab program written by B. Geier was used and modified[3].

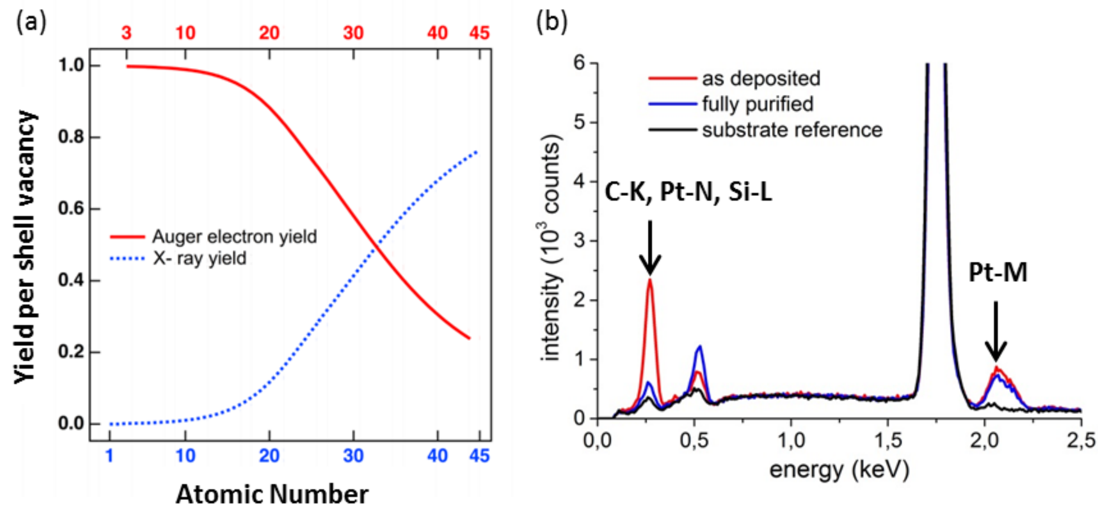

Figure 13: (a) The X-ray and the Auger electron yield in dependency of the atomic number. Light elements like carbon have a bad X-ray yield making quantification of light elements difficult with strong uncertainties. Modified from [36]. (b) EDX spectra of an as-deposited Pt-C deposit, fully purified Pt deposit and the SiO_2/Si substrate (Si-wafer) as the reference. The as-deposited Pt-C spectra has a high peak around 0.25 keV containing mainly the C-K line but also the Pt-N line (originating from the deposit) and the Si-L line (originating from the substrate). Therefore, it's necessary to calculate the C/Pt ratio to receive a reliable, relative value for the carbon content.

2.4.1.1 In-Situ and Ex-Situ EDXS Analysis

The semi-quantitative approach of using the relative C/Pt ratios allows the determination of the relative carbon content inside the deposit. Two different types of EDXS analysis have to be distinguished:

- *In-Situ* EDXS: The data of the *in-situ* EDXS were gained during the purification process in the ESEM mode which means that the same microscope parameters as for the purification (primary beam energy, current, field of view, etc.) were used. Therefore, there is no *in-situ* EDXS analysis possible if the primary energy is below 2.25 keV, because then the Pt-Peak wouldn't occur in the spectrum anymore. *In-situ* EDXS data reveal the decrease of the C content during the purification process. The saturation behaviour is a good indicator for the operator when the purification process is finished.
- *Ex-Situ* EDXS: The data of the *ex-situ* EDXS were gained on the deposits before or after the purification. The *ex-situ* EDXS data are usually more accurate concerning the exact values,

because in contrast to the *in-situ* EDXS data, the microscope parameters can be chosen optimal for recording them. For example the *ex-situ* data could be recorded on small, central areas of the deposit (for example 1x1 µm² on a $2 \times 2\ \mu m^2$ Pt pad). In contrast to that for the *in-situ* EDXS data the purification field had to be chosen larger than the actual deposit resulting in the surrounding area contributing to the EDXS signal. Furthermore, the *ex-situ* data were always gained in HV and not in the ESEM mode, since first one is more exact due to less scattering.

2.4.1.2 Inner Structure of an EDX Spectrometer

An EDX spectrometer consists of 3 main parts: the detector, the processing electronics and the multi-channel-analyser (**MCA**). Inside the semiconductor detector electron-hole pairs are created by the incoming X-rays. The band gap between valence and conduction band is 3.8 eV for Si. In a Si(Li) detector the dotation of the Si with the Li leads to a p-n junction. Since X-rays have normally energies higher than 1 keV, thousands of electron-hole pairs are produced by a single X-ray photon. The energy of the incoming X-ray photon can be analysed, because the amount of electrons produced is directly proportional to the energy of the incoming X-ray photon. An applied, reversed bias across the intrinsic zone separates the electrons and holes and collects them on the electrodes on the faces of the crystal generating a charge pulse. To reduce the leakage current a Si(Li) detector has to be cooled with liquid nitrogen. The signal gets amplified by a field effect transistor and then identified electronically. Afterwards the MCA stores the digitized signal in a channel which is assigned to the X-ray energy of the photon.[8,9]

In Figure 14 a schematic illustration of the inner structure of an EDX spectrometer can be seen.

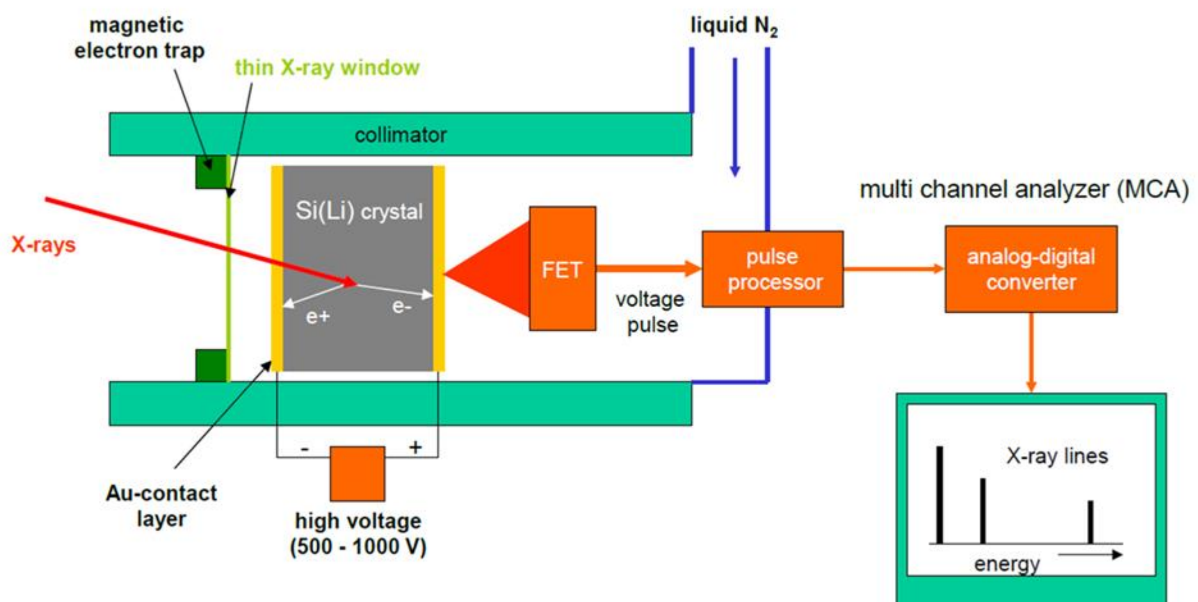

Figure 14: Schematic illustration of an energy dispersive Si(Li) X-ray spectrometer (EDXS). From [37].

2.4.2 Atomic Force Microscopy (AFM)

Atomic Force Microscopy (**AFM**) is a surface scanning probe technique with possible resolutions down to the sub-nm range. The measuring unit thereby is a small, flexible cantilever with a thin tip. The typical tip radii are between 10 and 20 nm. During this thesis a Bruker Dimension Fastscan AFM was used. When the tip approaches the surface in dependence of the distance different forces are dominating:[38]

- Electrostatic or magnetic forces dominate for tip-surface distances larger than 10 nm
- Van der Waals (**VdW**) forces predominate between approximately 10 to 5 nm tip-surface distance
- Electron-electron repulsion (stemming from the Pauli exclusion principle) is a strong repulsive force, which begins to predominate for distances smaller than approximately 2 nm

For scanning the surface, the tip is normally located closer than 10 nm to the surface. Therefore, the influences of VdW forces and electron-electron repulsion are by far the most predominant and the Lennard Jones potential (**V_{LJ}**) can be used to describe the interaction:[38]

$$V_{LJ} = V_{VdW} - V_{rep} = -\frac{a}{r^6} + \frac{b}{r^{12}} \tag{13}$$

V_{LJ} ... Lennard Jones potential
V_{VdW} ... Van der Waals (VdW) potential
V_{rep} ... electron-electron repulsion
a, b ... constants
r ... tip-sample distance

The acting force is received by differentiate the potential after the tip-sample distance r:[38]

$$F_{LJ} = \frac{dV_{LJ}}{dr} = \frac{6a}{r^7} - \frac{12b}{r^{13}} \tag{14}$$

In Figure 15 the characteristic LJ potential (blue solid line) can be seen, which is the superposition of the VdW potential (green dashed line) and the electron-electron repulsion potential (red dashed line). The green coloured area marks the values for the tip-sample distance for which the VdW forces predominate. The red area marks the area where the electron-electron repulsion dominates. The black solid line is the force originating from the LJ potential (**F_{LJ}**). When an AFM tip is continuously approached to the surface, it begins to sense the attractive VdW force when entering the green area. At the moment when the force exceeds the threshold force of the cantilever (green dashed line) the cantilever jumps to full contact.[38]

The interaction force with the surface bends the cantilever. To measure this bending, different approaches are possible. For example, for so called self-sensing cantilevers (SS-CL) the deflection is measured via piezo resistors implemented in the cantilever. The Bruker Dimension Fastscan, which was used for the AFM measurements in this thesis, used an optical detection system, whose

functional principle can be seen in Figure 16. A laser shines on the cantilever and is reflected in the on a position sensitive (photo)detector (**PSD**). When the cantilever is deflected (e.g. by surface features), the laser spot is reflected to a different area of the PSD. In case the reason for the deflection is a surface feature, the scan moves in the according direction to compensate that feature.[38]

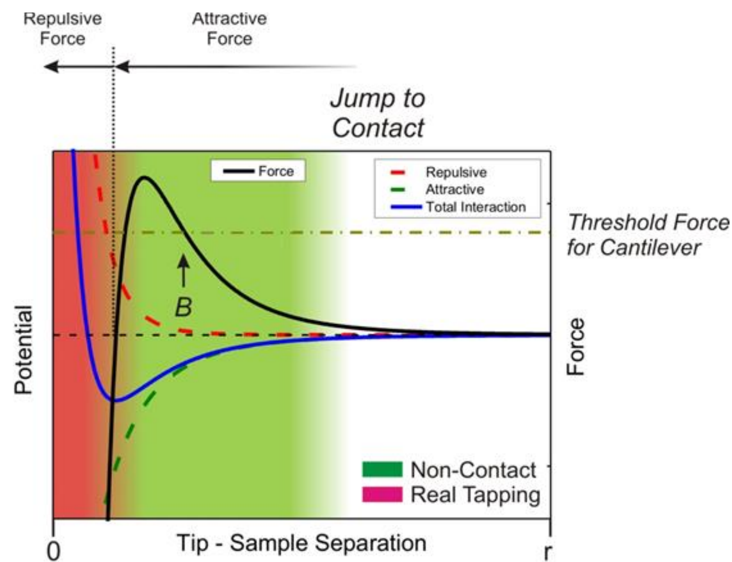

*Figure 15: Potential situation for an AFM tip in dependence of the distance to the surface. The Van der Waals (**VdW**) potential resulting in an attractive force is displayed by the dashed green line, while the dashed red line represents the electron-electron repulsive potential. The superposition of this 2 potentials results in the Lennard Jones (**LJ**) potential (blue solid line) and in the force displayed by the black line. When approaching the surface, at the point B the cantilever jumps to the contact distance because the threshold force of the cantilever (green dash-dotted line) is exceeded by the attractive force. From [38].*

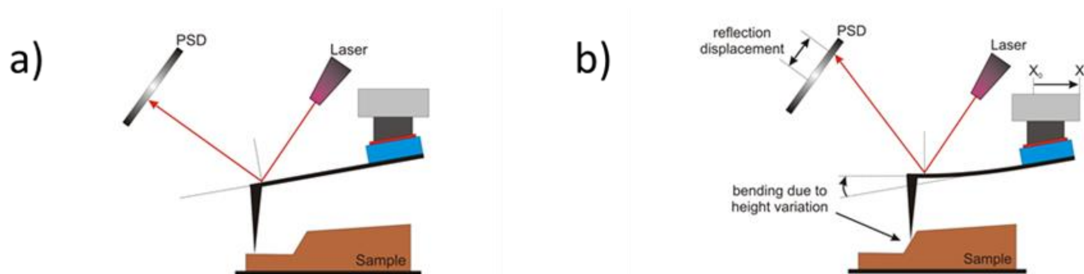

*Figure 16: Function principle of optical deflection detection, which the Bruker Dimension Fastscan, used during this thesis, utilizes. A laser shines on the cantilever tip and is reflected on a position sensitive (photo)detector (**PSD**). If, during the scanning movement, the cantilever gets deflected from the equilibriium state (a) because of a surface feature, the position of the reflected laser beam on the PSD changes (b). Both from [38].*

Since these movements need to be in the sub-nm range, piezoelectric crystals are used. An applied voltage to a piezoelectric crystal leads to an expansion or contraction as displayed in Figure 17 (a). Since an AFM head needs to execute movements in all 3 spatial dimensions, a special arrangement of the piezoelectric crystals has to be chosen, which can be seen in Figure 17 (b). The x and y motion are needed for the scanning movement, while the z movement is needed for the tip to follow the surface morphology.[38]

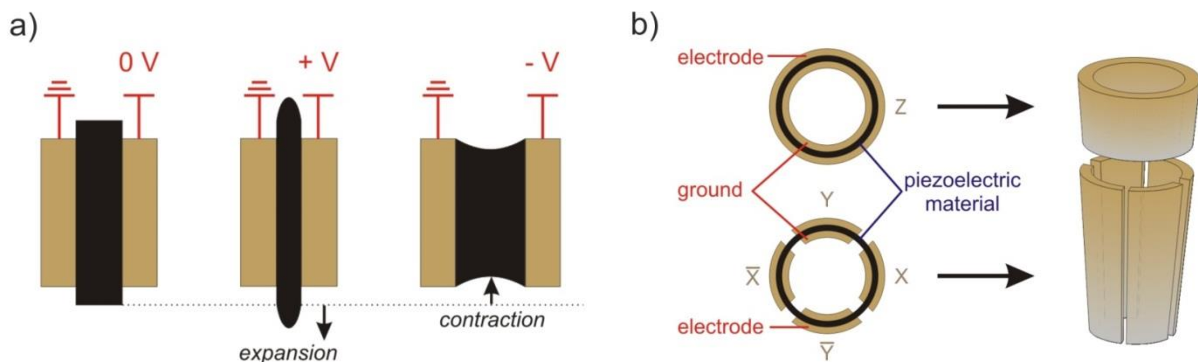

Figure 17: Function principle of the use of piezoelectric crystals for movements in small scale. (b) Arrangement of piezo crystals in an AFM scan head to enable movements in all 3 spatial directions. Both from [38].

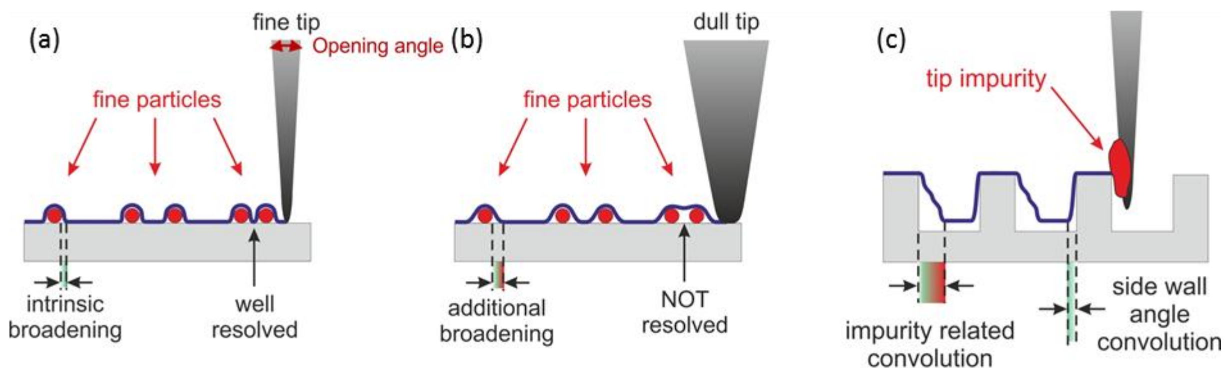

Figure 18: (a) Even for perfectly sharp cantilever tips, an intrinsic broadening due to the tip radius blend into the scanning results. (b) If the tip is dull small surface features can't be resolved anymore and also the intrinsic broadening is more severe. (c) When measuring walls perpendicular to the surface, even for a perfect tip, in the measuring results the side walls are not perpendicular because the measurement blends the side wall topography with the tip angle. If an impurity is stuck at the side of the tip, that additionally reduces the appeared steepness of the wall. All from [38].

A very important component of the measuring process is the cantilever tip as can be seen in Figure 18. Even if the cantilever tip is perfectly sharp, an intrinsic broadening of surface structures occurs in the measurement results (see Figure 18 (a)). For dull tips the additional broadening is larger and fine surface features can't get resolved anymore (see Figure 18 (b)). When measuring a wall perpendicular to the surface, in the measurement results this wall doesn't appear perpendicular to

the surface, because beside the wall topography the tip angle is blended in the results (see Figure 18 (c)). Impurities, which might be picked up during the measurements, can drastically worsen the measurement results (see Figure 18 (c)).[38]

There are numerous different variants of imaging modes (contact mode, tapping mode, conductive AFM, chemical AFM,…). Since contact mode, for which the tip is always in contact with the surface and is thereby dragged over it, can result in surface damaging and the quality of the tips worsens fast, often the so called tapping mode is preferred to receive topographic surface features. All AFM results, which are presented below, were gained via tapping mode.[38]

For the tapping mode, the cantilever is excited into oscillations by a piezo crystal so that it taps the surface periodically. In the beginning the stimulating vibration of the piezoelectric crystal is tuned to match the resonance frequency of the cantilever. When the vibrating tip interacts with the forces originating from the surface, 2 main effects occur:[38]

1. The undisturbed resonance amplitude is damped. Using this effect the height information can be gained.
2. A phase shift between the exciting piezo oscillation and the cantilever oscillation occurs. The phase shift depends partly on the local surface material and thereby a material contrast can be seen in the phase image.

2.4.3 Transmission Electron Microscopy (TEM)

A transmission electron microscope (**TEM**) uses, as already the name indicates, electrons to shine through a thin sample of several nm thickness. The electrons emitted by the source are accelerated up to 300 keV primary beam energy[39]. The TEM, which was used for the examinations in this thesis, was a FEI Tecnai F20.

There are various different TEM modes. A standard mode is the parallel beam operation mode, which can be seen for the part of the beam path above the specimen in Figure 19 (a) and for the part below the specimen in Figure 19 (b). Of those electrons, which have passed through the sample, the unscattered electrons can be selected and the scattered ones excluded in the beam path below the specimen (Figure 19 (b)). Then the resulting image is a so called bright field (**BF**) image. If the opposite is the case, the scattered electrons are selected and the unscattered ones are excluded, a dark field (**DF**) image is received. High resolution TEM (**HRTEM**) is an operation mode with especially high resolution showing details finer than 0.2 nm.[39]

When scanning transmission electron microscopy (**STEM**) is used, the beam hitting the specimen is not parallel anymore but focused and convergent, which can be seen in Figure 19 (c). Two scanning coils between C2 (condenser lens 2) and C3 initiate the scanning movement across the sample (the coils are not shown in (Figure 19 (c)). In dependence of their interaction with the sample, different signals can be distinguished. The unscattered electrons form the BF signal, as can be seen in Figure 19 (d). The inelastically scattered electrons are scattered in a relatively low angle and contain information about interaction processes, by which the primary electrons have lost energy. These electrons can be used to form the annular dark field (**ADF**) image. Elastically scattered electrons are

scattered at a much larger angle than inelastically scattered electrons. Using elastically scattered electrons a high-angular annular dark field (**HAADF**) image is received, which shows a high Z contrast.[39]

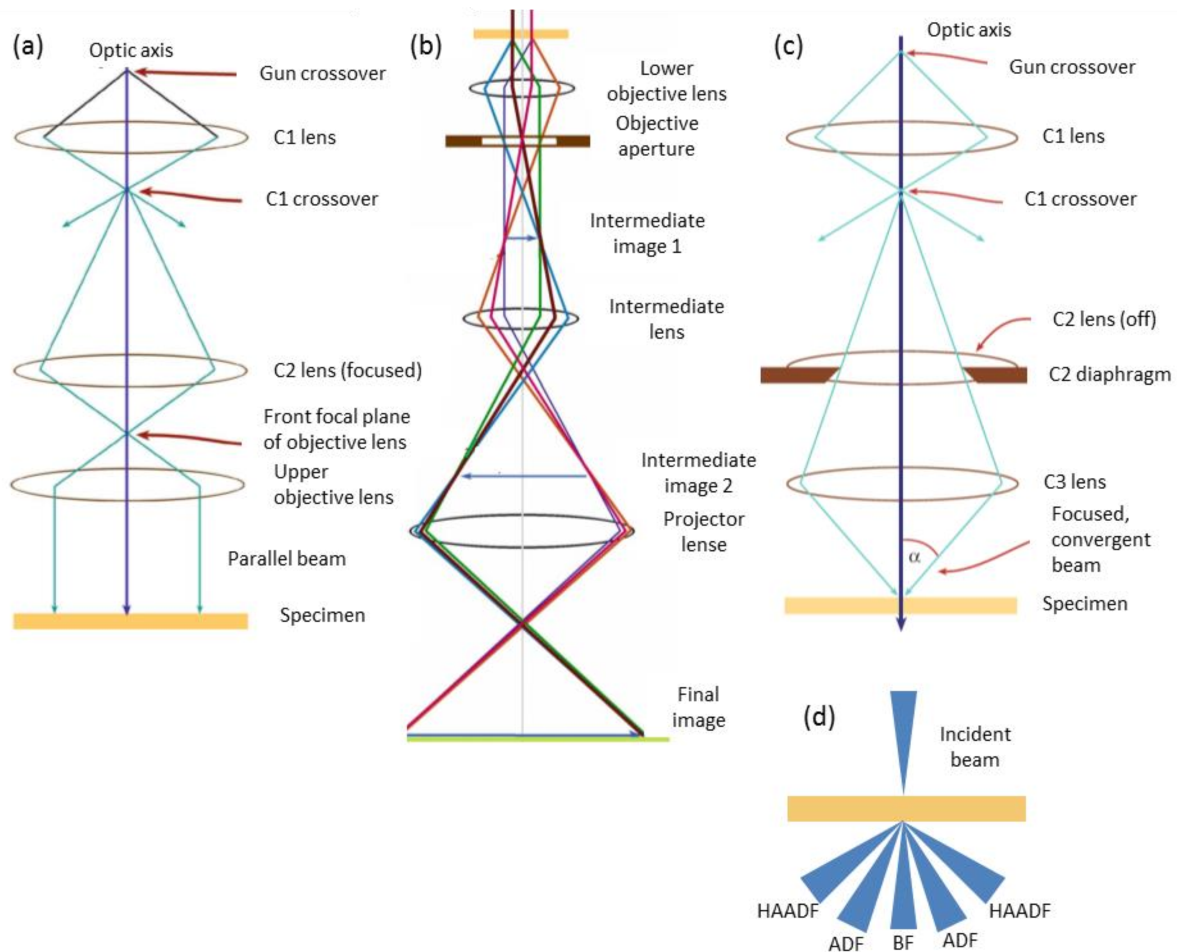

*Figure 19: (a) Upper part (above the specimen) of the beam path in paralell beam TEM operation mode ("C" indicates a condensor lens). (b) Lower part (below the specimen) of the beam path in parallel beam TEM operation mode. If by the objective aperature unscattered electrons, which passed through the sample, are selected, a bright field (**BF**) image is received. If the scattered electrons are selected a dark field (**DF**) image is received. (c) Beam path above the specimen for scanning transmission electron micrsocopy (**STEM**). Between C2 and C3 (C3 corresponds to the upper objective lens in paralell beam operation mode) there would be the scan coils, which are responsible for the scanning movement but aren't pictured in this image. (d) Different image modes in a STEM. All from [39].*

As already explained above, the inelastically scattered electrons contain information about the interaction process causing the energy loss. This interaction process can be the creation of X-rays, which can be used for EDXS analysis as explained in chapter 2.4.1. But also, the energy loss of the primary electrons can be examined directly via electron energy loss spectroscopy (**EELS**). To analyse

the energy loss of the primary electrons a magnetic prism spectrometer is used, whose function principle can be seen in Figure 20.[39,40]

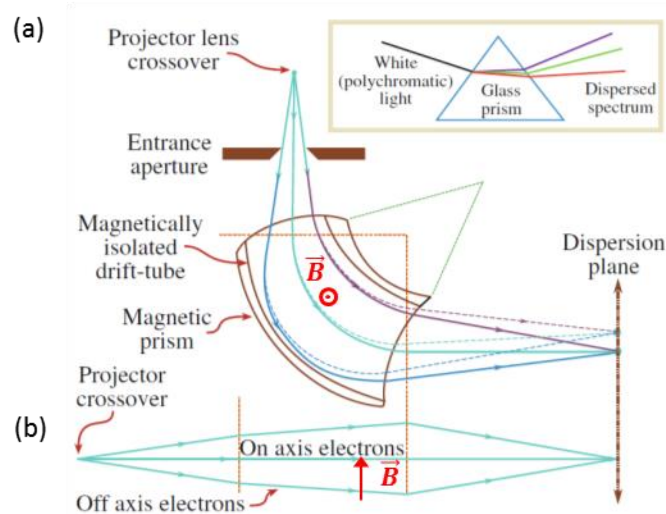

Figure 20: (a) Schematic drawing of the ray paths through a magnetic prism spectrometer showing that energy-loss and no-loss electrons have different dispersion. However, electrons with same energy are focused on the same spot of the dispersion plane, since the prism is also a lens. The analogy with dispersion of white light in a glass prism is shown in the inset. (b) The focusing mechanism of the magnetic prism in the plane normal to the spectrometer by fringing field at the pole piece edges. Both from [39].

A magnetic field is used to create an energy dispersion effect for the electrons, as can be seen by setting equal the Lorentz and the centripetal force:[40]

$$|F| = evB = \frac{mv^2}{R} \rightarrow R = \frac{me}{B} \cdot v \rightarrow R \propto v \tag{15}$$

F	…	centripetal and Lorentz force
e	…	electron charge
v	…	electron velocity
B	…	magnetic field
m	…	relativistic electron mass
R	…	electron circular path radius

The magnetic prism spectrometer acts also as a lens for electrons with the same energy so that on axis and off axis electrons with the same energy are focused on the same spot on the dispersion plane. The reason for that, which can be seen in see Figure 20 (a), is that electrons below the central trajectory run through a longer path within the magnetic field and therefore get deflected stronger while it's inverse for electrons above the central trajectory. Also in the plane normal to the spectrometer (parallel to the magnetic field) of axis and on axis electrons are focused in the same spot (see Figure 20 (b)), because of fringing fields at the pole piece edges. Multipole lenses behind

the magnetic prism spectrometer magnify the energy dispersion and reduce the aberrations. The electrons are converted to an optical signal via a scintillator and are recorded via a CCD detector.[39,40]

Via EELS it's possible to detect elements from He till U. Light elements and noble earth elements but also transition metals are detected with especially high efficiency. The identification of a wide range of elements via EELS is possible because the PE use a characteristic amount of energy when inner shell electrons are knocked out. During the refilling process of this inner shell vacancy, either Auger electrons (**AE**) or X-rays are created, which both can also be also used for characterization (see chapter 2.4.1). The typical detection efficiency for EELS is in the range of 0.1 to 1 at.%. In the low loss range of the spectrum below 50 eV, the inelastic interactions of the primary electrons give information about the electrical and physical properties of the specimen. One of this inelastic scattering in the low energy range is the excitation of plasmons.[39,40]

2.4.3.1 Plasmons

A plasmon is a quasi-particle representing a collective excitation of the conduction electron gas in a metal. For so called bulk plasmons the conduction electrons are displaced at one instant in time and then oscillate in phase against the positive ions with the plasma frequency. Because their frequency is exactly the plasma frequency, they can't couple to transverse electromagnetic waves and can only be caused by charged particle impact. Surface plasmons are, as the name already suggests, waves at a metal/dielectric interface. Thereby, an electric field is coupled to the charge oscillations. Surface plasmons in macroscopic (concerning the wavelength) systems are evanescently limited, localised to the metal/dielectric interface and propagating.[41–43] When the size of a particle becomes much smaller than the exciting wavelength $d \ll \lambda$, the 2D surface is rolled up to a quasi 1D wire with periodic boundary conditions at the "start" (arbitrary defined) and the "end" of the wire. The periodic boundary conditions force the charge oscillation corresponding to the surface plasmons of the wire to be periodic, divided over the circumference of the loop and non-propagating. This leads to discrete plasmonic surface modes with specific frequencies. Higher order modes than dipole modes in nanoparticles cannot interact with an electric field that is constant across the particle. Therefore, these higher modes are called (optically) dark modes while the dipole modes are called (optically) bright modes. Although non-propagating surface plasmons in nanoparticles follow the same physical principles as propagating ones in the higher dimensional case, in literature they have been described separately for a long time.[41–44]

Electrons from an electron beam can induce plasmons in nano-structures. The high resolution in a STEM allows creating plasmonic maps of the non-propagating plasmons. That means that for a certain energy loss a 2 dimensional plasmonic map can be obtained. In the totality of the different energy losses, plasmon maps for all different plasmon energies are obtained. The electron beam can interact directly with multiple plasmon modes and unlike optical excitation, which interacts only with dielectric modes, they can also interact with quadrupole, hexapole and higher modes of a wide range of possible frequencies. This allows examining effects not accessible with other techniques. [41–44]

Since this thesis doesn't provide enough space for a more detailed insight into plasmonics, the references above can be recommended for a more detailed insight.

2.4.4 Electric Measurements

Examinations about the electric properties of as-deposited FEBID structures and possible applications have been already done in previous master theses[45,46]. During this master thesis the resistance development for Pt deposits during the purification process was measured and the resistivity of fully purified structures was determined and optimized. The resistivity of the deposit is determined by measuring the resistance and scaling it by the cross section of the deposit, through which the current flows, and the distance over which the resistance was measured:

$$\rho = R\frac{A}{l} = \frac{U}{I} \cdot \frac{A}{l} \tag{16}$$

ρ	…	resistivity	Ωm
U	…	voltage	V
I	…	current	A
R	…	resistance	Ω
l	…	travel distance of the current	m
A	…	cross section of the deposit	m^2

The substrate used for the resistivity measurements, was a boron doped silicon wafer with dimensions of $25 \times 12 \times 2\ mm$ and a 500 nm thick SiO_2 layer on top to ensure isolation and prevent any current between the electrodes. On each substrate there were four 2-electrode setups and one 4-electrode setup. The electrode structure was designed and fabricated in the frame of a previous master thesis[46] together with Dr. Andreas Hohenau (Institute for Physics, Karl-Franzens-University Graz, Austria). The substrate was manufactured by using e-beam lithography and subsequent physical vapour deposition of (1) an approximately 5 nm thick Cr layer to raise adhesion and afterwards (2) the thicker Au layer leading to a total height of approximately 50nm.

To measure the resistivity, the 4-point method was chosen using the 4-electrode setup of the substrate seen in Figure 21 (a). The exact measurement setup can be seen in Figure 21 (b). For a 4-point measurement a constant current is sent over two outer contacts, while via the two inner contacts the voltage drop is measured. Together with the constant current the resistance between the 2 inner contacts of the voltage measurement, can be calculated. The 4-point measurement has the big advantage that only resistance of the deposit is taken into account, but all contact and wire resistances are cancelled out. The measurement setup for the deposits can be seen in Figure 21 (b). Knowing the distance between the 2 inner electrodes, the height and the width of the deposit, the resistivity of the Pt deposit can be calculated via (16). As constant current source a *Keithley 224 Programmable Current Source* was used and the voltage was measured with a *Keithley 196 System DMM* (Digital Multimeter).

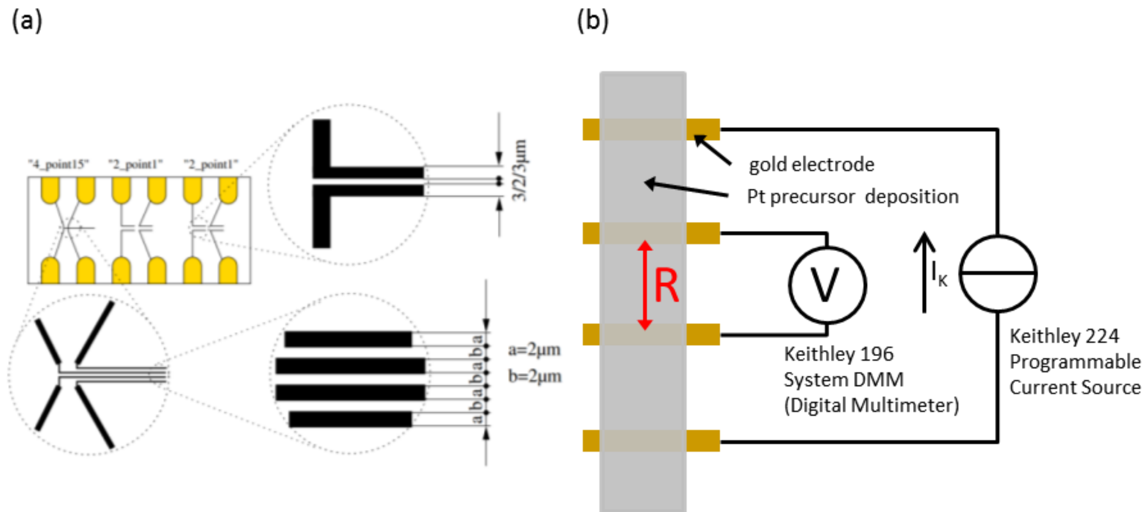

Figure 21: (a) Au electrode layout of the substrate used for the electric measurements providing 2-electrode but also 4-electrode structures. From [45,46]. (b) Schematical drawing of the setup to measure the resistivity. The so called 4-point method was used, which has the advantage that only the resistance of the deposit between the 2 inner contacts is measured, while contact and wire resistances are cancelled out.

3 Experiments and Results

The aims of this thesis were applications of metalorganic FEBID deposits, which were transformed via electron stimulated H_2O reactions (purification) from their original state of containing a large proportion of carbon into chemically pure metal deposits. The deposits were fabricated in a dual beam microscope (**DBM**), consisting of a scanning electron microscope (**SEM**) and a focused ion beam beam (**FIB**), and further purified in an environmental scanning electron microscope (**ESEM**). The results were analysed via DBM, ESEM, atomic force microscope (**AFM**) and transmission electron microscope (**TEM**). Figure 22 shows an overview over the topics handled during this master thesis including the work-flow.

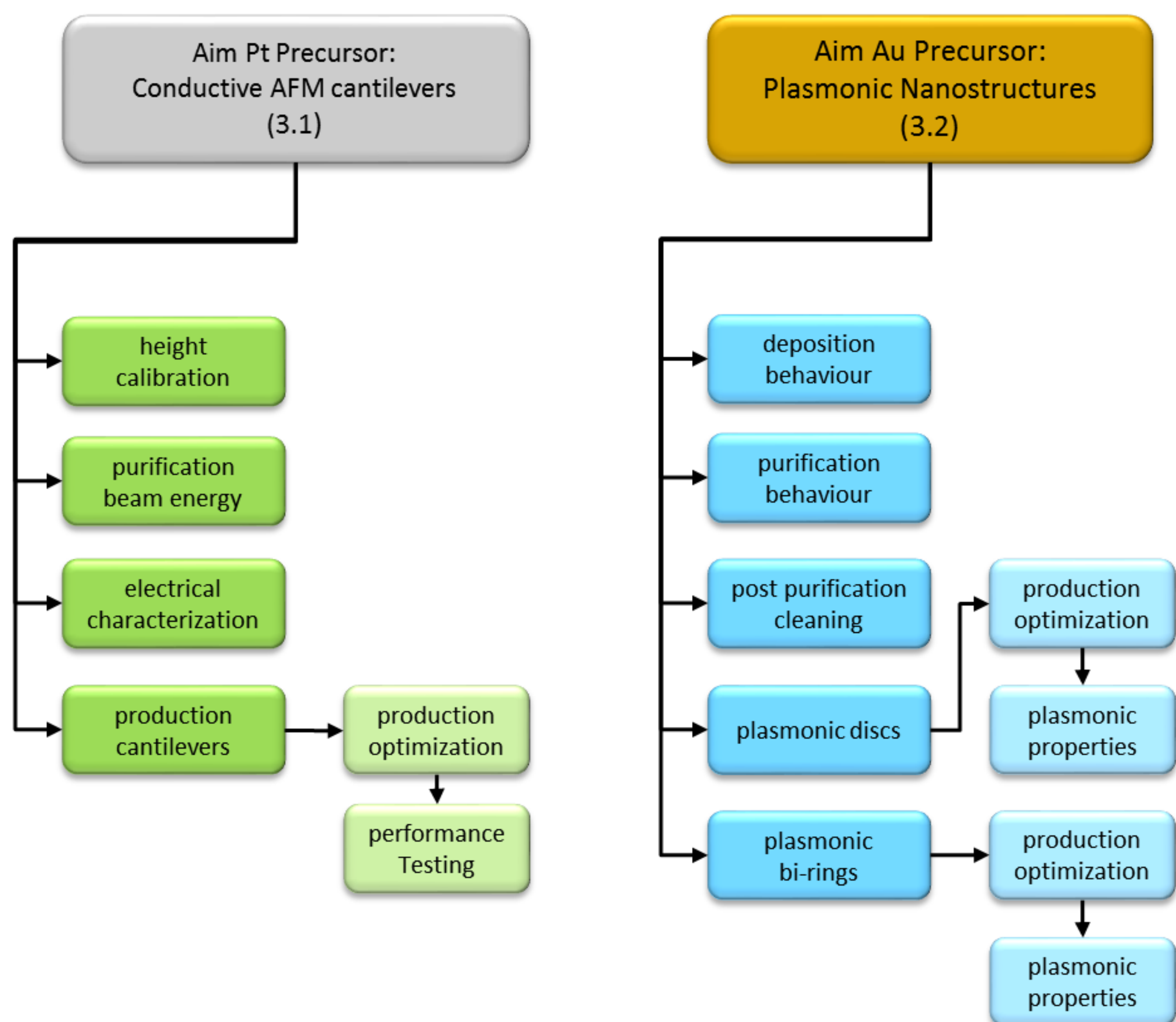

Figure 22: Overview of the topics handled during the master thesis. The two main aims were to produce conductive AFM cantilevers with FEBID technique (left column) and to prove that plasmonic gold nano-structures can be produced via FEBID (right column).

The aim for the Pt precursor was to modify self-sensing cantilevers (**SS-CL**) via FEBID in such a way, that conductive-AFM (**C-AFM**) measurements can be done (chapter 3.1). Therefore, experiments to calibrate the height for the Pt precursor depositions (chapter 3.1.2) and to examine the influence of different purification beam energies were initially performed (chapter 3.1.3). The *in-situ* resistivity development of Pt deposits during the purification procedure was determined and pure Pt deposits were electrical characterized *ex-situ* after the purification (chapter 3.1.4). The manufacturing of the conductive cantilevers was then optimized (chapter 3.1.5.2) and the performance of the cantilevers was tested together with our industrial partners (chapter 3.1.5.3).

For the Au precursor, the aim was to first learn how to handle this precursor, which was newly introduced at the institute. First experiments about the basic deposition characteristics were done (chapter 3.2.2) in comparison with our standard Pt precursor. The purification approach, used for Pt-C deposits, was then expanded to the Au based precursor (chapter 3.2.3). As carbon residues along the edge of the scan frame are often appearing as a drawback, a post purification cleaning method could be developed to entirely remove this residues (chapter 3.2.4). This strategy is also relevant and applicable for purified Pt-C deposits. Finally, Au-C discs were fabricated and optimized for plasmonic characterization (chapter 3.2.5.1). Next, the plasmonic activity of ideally purified FEBID Au discs was successfully proven. Their plasmonic properties were then compared with discs produced via conventional lithography (chapter 3.2.5.2) to assess the quality of FEBID based Au structures. Finally, the thesis focused on Au bi-ring structures and if these materials / structures could be used as metamaterial for Terra-Hertz plasmonic applications. Dedicated experiments determining the FEBID resolution, downscaling behaviour and purification were carried out (chapter 3.2.6.2). Although final bi-ring systems for optical characterization were produced after this master thesis by J. Sattelkow, the presented experiments can be considered as proof-of-concept (chapter 3.2.6.3).

3.1 Platinum High-Resolution AFM Tips for Electric Measurements

3.1.1 Motivation

In contrast to a conventional AFM design, where the cantilever deflection is monitored optically, which results in a relatively large and complicated scan head (see chapter 2.4.2), self-sensing-cantilevers (**SS-CL**) are using piezo resistors (see Figure 24 (a)) to measure the deflection [47]. Figure 23 shows the highly compact AFSEM® AFM scan head which becomes possible due to the application of SS-CLs. This allows using such an AFM inside the chamber of a SEM providing the user both, the possibilities of an SEM and of an AFM [47].

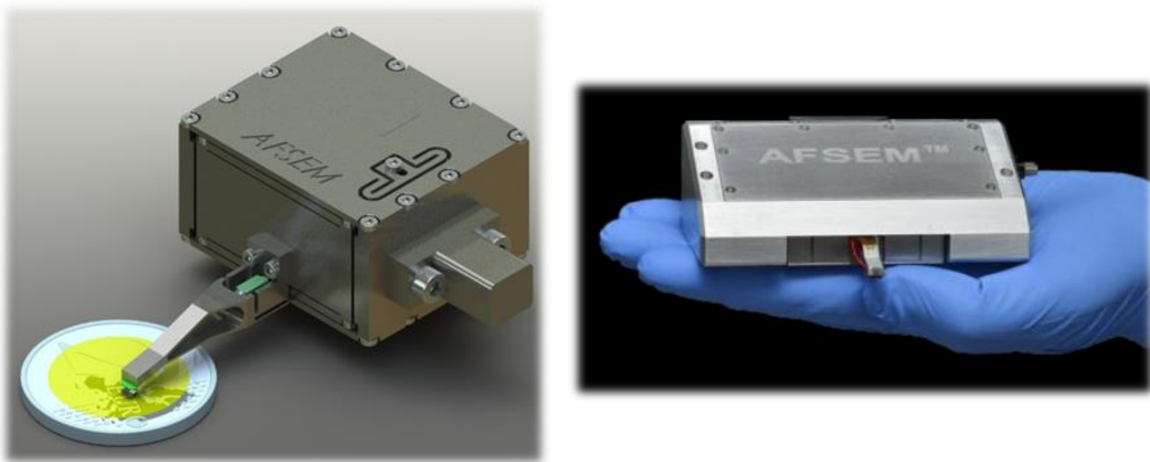

Figure 23: Highly compact AFSEM® scan heads for the seamless integration in SEMs, FIBs or DBMs.

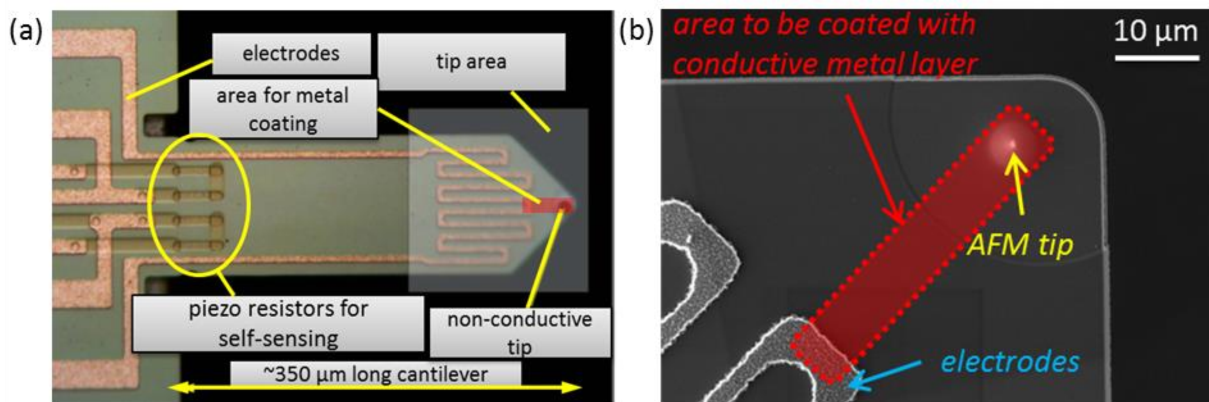

Figure 24: (a) Light microscope image of a self-sensing cantilever (SS-CL). The front part (red) should be coated with a Pt layer to reach electrical conductivity (modified from [47]). (b) Enlarged SEM image of the tip showing in red the area to be coated.

However, there are also some limitations using SS-CLs. One of them is, that currently they aren't suitable for electric C-AFM measurements, because highly conductive coating during the regular production process is not possible due to technical limitations. A market analysis by the

SCL-Sensor.Tech.Fabrication GmbH (further addressed simply as **SCL**), which are our industrial partner in this project, revealed a high interest for electrical conductive SS-CL in combination with the AFSEM® platform. Especially, it would provide a unique selling point for the products of SCL.[47]

In Figure 24 (a) there can be seen an overview image of a SS-CL with the intended area for coating marked in red. In Figure 24 (b) the area between the electrodes and the tip can be seen in higher resolution. This red area has to be coated with a high conductive metal layer in order to receive a CL suitable for C-AFM measurements.

Already before the start of this project, SCL tried the most obvious approach of using shadow mask technique for coating. The results can be seen in Figure 25. Two main problems occur using shadow mask technique, which makes it not suitable to produce SS-CL for C-AFM measurements[47]:

1. The AFM tip radius is increased dramatically to 23 nm, which leads to a much worse resolution of the AFM tip. Also the roughness on the tip is increased (see Figure 25 (a)).
2. Because the Al electrodes are ≈350 nm high and strongly porous, it wasn't possible to accomplish a sufficient electrical contact between the electrode and the coated Pt-layer (see Figure 25 (b)).

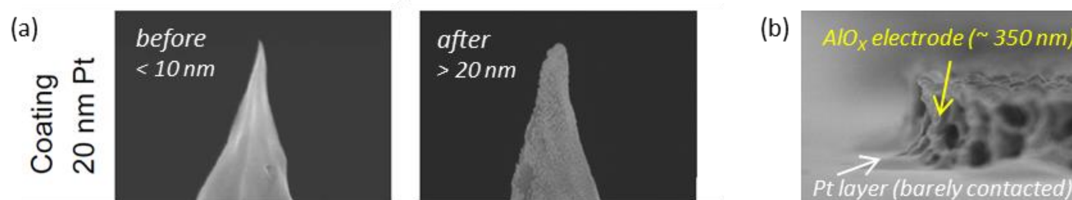

Figure 25: (a) SEM images of an ideal SS-CL tip before (left) and after (right) the coating via shadow mask with a 20 nm thick Pt layer. Thereby the tip radius is dramatically increased from <10 nm to 23 nm making high resolution measurements impossible. (b) Problematic transitional area between the Pt layer and the Al electrode, strongly reducing or totally preventing electric conductivity. From [47].

To overcome these problems sticking with the shadow mask technique, it would have been necessary to change the entire production process for the SS-CL. Therefore, it was decided to try the new approach of 3D (nano) deposition of Pt-C via FEBID and subsequent e-beam assisted H_2O purification[2,3], to reach pure Pt-deposits.

3.1.2 Height Calibration and Growth Rates for the Pt Precursor

First the growth rates of the Pt based precursor were examined to be able to produce deposits in a certain target height. Depositions with the Pt precursor were made with 2 different gas injection systems (**GIS**): The *custom GIS* and the *working GIS* (see chapter 2.1.2.7). This is due to the fact, that the first depositions Pt-C depositions were made with the *custom GIS* but later this system was used for the Au based precursor.

Since the height (thickness) of a deposit is usually smaller than 150 nm, the height can't be accurately determined by a simple SEM investigation. Therefore, it's necessary to use an AFM. However, switching samples from the FIB to the AFM and carry out the AFM measurements is time intensive. Therefore, the deposition rates for certain deposition parameters were determined, which allowed later to produce depositions with desired heights.

To determine the deposition rates, an array of $2 \times 2\ \mu m$ pads with different numbers of passes and thereby different t_{rel} (relative exposure time, see chapter 2.1.2.4) were deposited and afterwards the height was measured via AFM. Although the current and the DT were different for the 2 GIS systems, both sets of deposition parameters were in the **MTL** (**M**ass **T**ransport **L**imited) regime [6]. For the *custom GIS* the deposition parameters were 5 keV, 98 pA, 10 µs DT and 13 nm PoP. The defocus for this and other depositions in this thesis was 0 µm, if not specified differently. The heights for the varying relative exposure times and according number of passes can be seen in Figure 26 (a). For the *working GIS* the deposition parameters were 5 keV, 1.6 nA, 100 µs DT and 13 nm PoP. These heights can be seen in Figure 26 (b). Both height diagrams show a linear behaviour, which makes the height tuning easy. As a result of the GIS nozzle geometry and its position (chapter 2.1.2.4), the depositions with the *custom GIS* had a height growth rate more than 3 times larger than those of the *working GIS*, although the deposition using the *working GIS* was using a much bigger current.

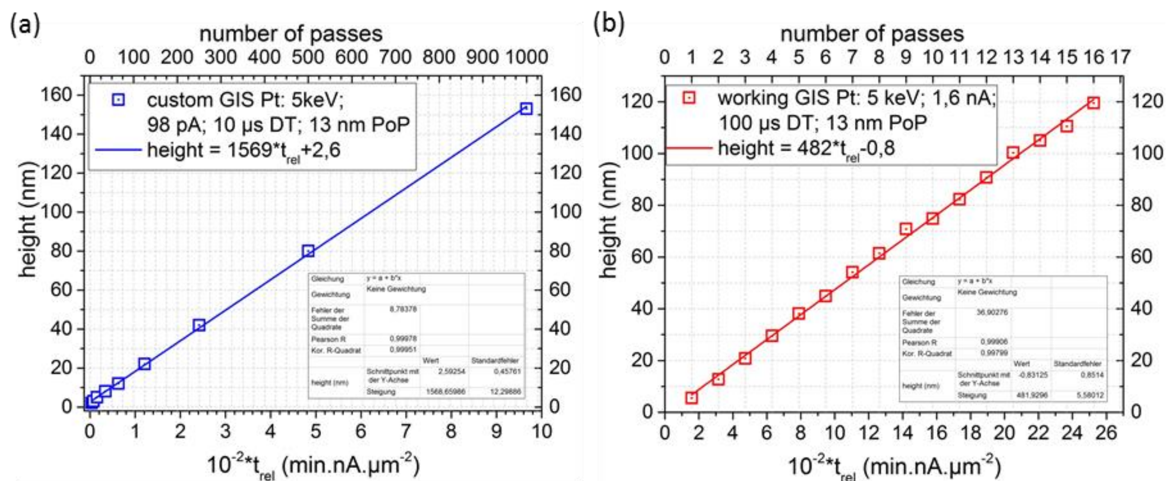

Figure 26: (a) Deposition height for the custom GIS in dependence of t_{rel} or the number of passes (two x-axes). (b) Deposition height for the working GIS. The used parameters can be found in the legend.

3.1.3 Purification of µm-Scale Pt-C Pads with Different Primary Beam Energies

As already shown by B. Geier[2,3] purification parameter variation of the current, the PoP, the DT and the H_2O vapour pressure don't significantly change the final purity of a purified structure. However, to receive optimal shape fidelity short e-beam residence times per unit area, which means relatively large PoPs and short DTs, should be chosen for the purification, as it gives slightly better resuls.[3]

A parameter, whose influence on the purification has to be still investigated, is the primary electron beam energy during purification. Since the penetration depth of the electrons into the deposit (and

into the substrate) increases with the primary beam energy, lower primary beam energies mean a greater fraction of energy loss in layers close to the surface and thereby a stronger e-beam induced purification effect. For relatively thin deposits this might be an advantage since less energy is lost to the substrate. However, the scattering on the H_2O molecules in the beam bath in the ESEM chamber becomes stronger.

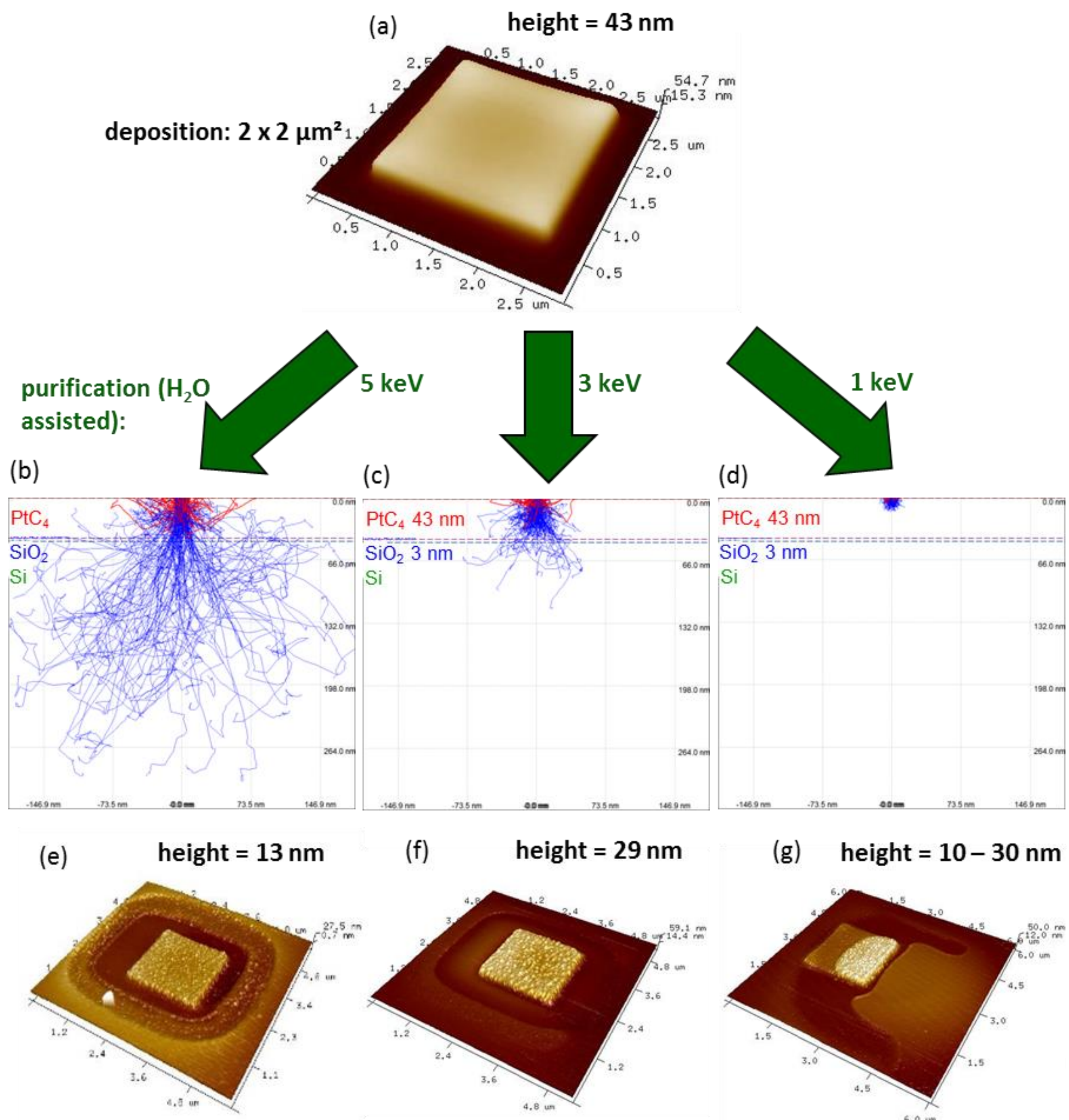

Figure 27: Schematic representation of the purification experiment with different primary beam energies. (a) shows the AFM image of the as-deposited pad. (b), (c) and (d) show Monte Carlo electron path simulations for primary beam energies of 5 keV, 3 keV and 1 keV. Blue are the primary electron trajectories and red are the trajectories of the backscattered electrons. The software used was Casino 2.48 [48]. (e), (f) and (g) show the AFM images of the purified structures for the corresponding primary beam energies. Note that for the AFM images the height of the deposit is also indicated.

The Pt pads with a footprint of $2 \times 2\ \mu m^2$ were produced with 5 keV, 98 pA, 10 µs DT, 13 nm PoP and 250 passes (MTL regime) resulting in a deposition with a height of 43 nm. The as-deposited pad can be seen in figure Figure 27 (a). After the deposition the pads were immediately transferred to the ESEM.

The pads were purified with 3 different primary beam energies: 5 keV, 3 keV and 1 keV. Other than that the parameters for the purification were the same: 2.4 nA current, 6.3 nm PoP, 1 µs DT, 10 Pa H_2O pressure, a dose of 100 C/cm² and a purification field of 3.2 x 2.8 µm².

In Figure 27 (b) - (d) there can be seen the Monte-Carlo Simulations of the electron paths. The 43 nm thick Pt-C deposit is red. The substrate is an ordinary $0.5 \times 0.5\ mm^2$ Si wafer with an approximately 3 nm thick SiO_2 layer covering the pure Si. 5 keV primary beam energy electrons have an average penetration depth reaching deep into the substrate. For 3 keV primary beam energy only a small part of the electrons reaches the substrate. And for 1 keV the electrons can only penetrate approximately half of the deposit.

In Figure 28 (a) – (c) there can be seen the distribution of the remaining electron energy inside the sample (same Monte Carlo simulations as in Figure 27). The different shells indicated by colours show the amount of remaining electron energy. As evident, while for 5 keV primary beam energy there is still 25 rel.% of it left at the bottom of the deposit, for 3 keV only 5 rel.% of the energy reach the bottom layer. For 1 keV primary electron energy, 50 rel.% of it is lost already in the first 7.5 nm and only 5 rel.% of the energy of the primary electrons gets deeper than 13 nm.

The *ex-situ* C/Pt peak ratios show for the as-deposited pad an expected value of approximately 1.5 for our X-ray spectroscopy system [3]. For pads purified with different primary beam energies the C/Pt peak ratio is around 0.2 (see Figure 29 (b)) according to the expected value for a fully purified structure [2,3] (this *ex-situ* EDXS data where gained in HV with 5 keV). As can be seen in Figure 27 (e) and in Figure 29 (b) the pad purified with 5 keV maintains the shape morphology and shows an expected volume loss of 70 vol.% as described by B. Geier et.al. [2,3]. Though, the EDXS data of the pad purified with 3 keV suggest a fully purified, carbon free deposit, the volume loss only adds up to 33 vol.%. Since most of the primary electron energy is lost before the deepest layer of the deposit (see Figure 28 (b) in comparison to Figure 28 (a)), this apparently leads to a problem (probably more porosity of the inner structure), because of the changed energy distribution together with the purification characteristic of being a bottom up process [2,3]. For the 1 keV pad the shape morphology is not maintained at all. At approximately half of the patterning footprint the height of the purified pad is 10 nm and on the other half it's 30 nm. A possible explanation might be that half of the pad delaminated during purification process. More extreme than for 3 keV not even a minor part of the primary electron energy reaches the bottom layer of the deposit. The maximum penetration depth of the electrons is less than half of the deposition height. This leads to the upper part of the deposit being purified and the lower part staying un-purified. Most likely, this leads to inner stresses and finally caused the delamination.

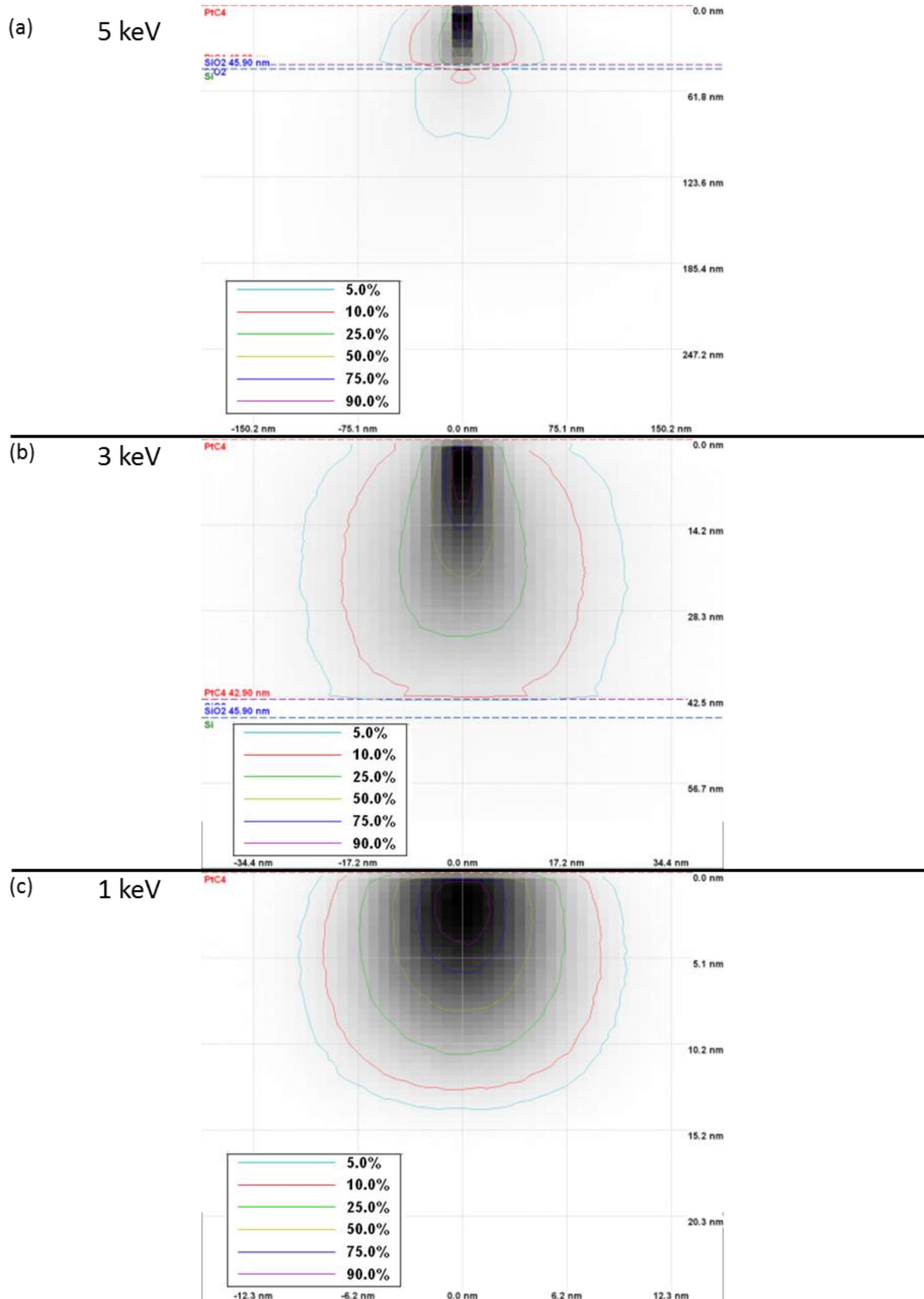

Figure 28: Monte Carlo simulations of the primary electron energy distributions inside the sample for the experiment with different primary electron beam energies of 5 keV, 3 keV and 1 keV. The concentric shells in different colours show the amount of remaining electron energy. Simulation was done with Casino 2.48 [48].

Figure 29 (a) shows the time evolution of the *in-situ* C/Pt peak ratios during the purification indicating the gradual carbon removal. There are only data for 5 keV and 3 keV, because for 1 keV the Pt-M peak is not recorded in the spectra anymore. Each EDX spectra was recorded over a period of 180 s. This acquisition time was also used for the vast majority of purification processes. In the rest of this thesis, the recoding time is only mentioned when a different value was used. The purification beam energy doesn't seem to have an influence on the purification speed. Both curves reach their saturation value of approximately 3 min.nA.µm^{-2}.

It can be concluded that for the purification of pads 5 keV purification energy shows clearly the best result (height dependent), since a reduction of the primary beam energy has a bad influence on the volume loss and shape morphology behaviour.

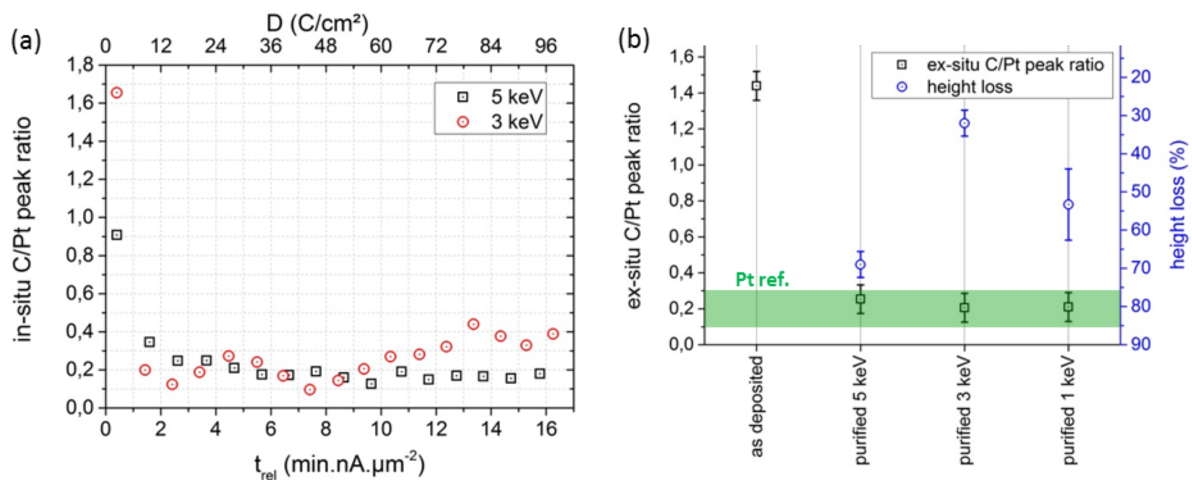

Figure 29: (a) Time evolution of the in-situ C/Pt peak ratio during purification for 5 keV and 3 keV primary electron beam energy (b) diagram comparing basic characteristics of the as-deposited and purified pads, the latter purified with different energies. There are 2 different y-axes according to 2 sets of data in this diagram: The left axis and the black, square data points show the ex-situ C/Pt peak ratio of the pads while the right y-axis and the blue, circular data points show the height loss of the purified pads compared to the as-deposited pad. The green zone indicates the approximate value for a sputtered Pt sample [2,3].

3.1.4 Electric Characterisation of Purified Pt Deposits

After having learned that 5 keV primary beam energy is better suitable for purification than smaller values, the next step was to investigate the resistivity of Pt deposits during purification. The coating of the SS-CLs has to be highly conductive in order to fulfil the requirements for conductive cantilevers. The electrical resistivity was determined with a 4-point measurement setup, like described in chapter 2.4.4. Pure Pt in the bulk state has a resistivity of $10.6\ \mu\Omega\ \mathrm{cm}$, which would be the ideal value for fully purified Pt structures to reach. As previous examinations by F. Kolb et al. showed [45,49], as-deposited Pt-C has a resistivity of $10^7\ \mu\Omega\ \mathrm{cm}$, which is approximately 10 million times larger than for pure Pt bulk state.

All Pt-C depositions for the electrical characterisation were made with the *working GIS*. The patterning footprint of the deposits was $15 \times 2\ \mu m^2$. The deposition parameters were 5 keV, 1.6 nA, 13 nm PoP, 100 µs DT and most of the time 10 passes leading to a deposition height of 75 nm. Once 14 passes were chosen, which resulted in a height of 105 nm (chapter 3.1.2).

2 structures were built to measure the resistivity and try to reach Pt bulk values. In the following they will be named pad 1 and pad 2. In the end, pad 1 consisted of 2 layers on top of each other and pad 2 consisted of 3 layers on top of each other. All layers were successively deposited and purified.

For pad 1 a 75 nm high Pt-C deposit was produced across the gold electrodes. The purification was done with 5 keV, 1.9 nA, 8 nm PoP, 1 µs DT, 10 Pa H_2O pressure, a purification field of $16 \times 3\ \mu m^2$ and a dose of 12.1 C/cm² (51 min purification time). Figure 31 (a) shows the time evolution of the *in-situ* C/Pt peak ratios. The saturation behaviour, which sets in after an approximate dose of 6 C/cm², gives a strong hint that the structure is fully purified. In Figure 30 (a) an AFM image of the Pt deposition after the purification can be seen. The red line marks the position of the xz-profile of the deposit between the 2 inner electrodes. This xz-profile can be seen in Figure 30 (b) and shows that after the purification the Pt deposit has an average height of 24 nm, which is exactly the expected height loss of 68 rel.%. Directly beside the deposit the surface level of the substrate is lowered due to edging processes during the purification (oxygen radicals). This effect occurs occasional during purification and amongst other things seems to depend on the substrate used. Since the deposit protected the substrate beneath from etching processes, the height was evaluated in relation to the normal substrate level. The width of the deposit is 2.2 µm and the distance between the 2 inner electrodes is 1.8 µm. These values for the deposit width and the inner electrode distance stayed the same for the other depositions.

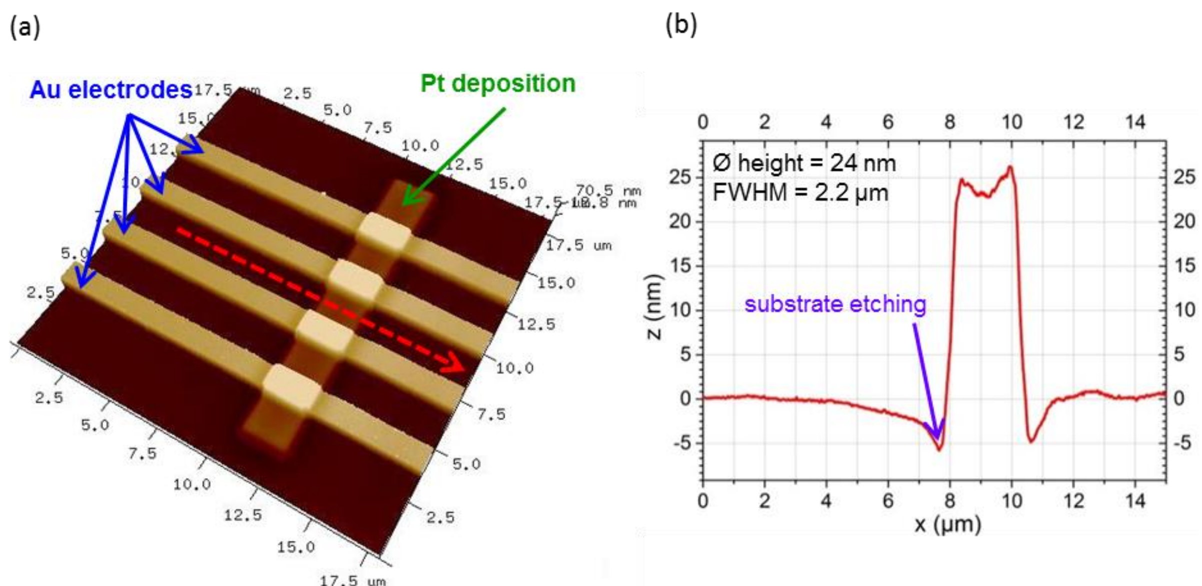

Figure 30: (a) AFM image of the 1st, fully purified, Pt layer of pad 1. The red line marks the position of the xz-profile displayed in (b).

The U / I characterisation in Figure 31 (b) shows a strongly linear behaviour. Via electric 4-point measurement a resistance of 129 Ω between the 2 inner electrodes was determined. Together with the dimensions of the deposit between the 2 inner electrodes, this leads to a resistivity of $391\ \mu\Omega\ cm$ (formula (16)), which is almost 40 times higher than the bulk state. For details about the 4-point measurement and the resistivity see chapter 2.4.4.

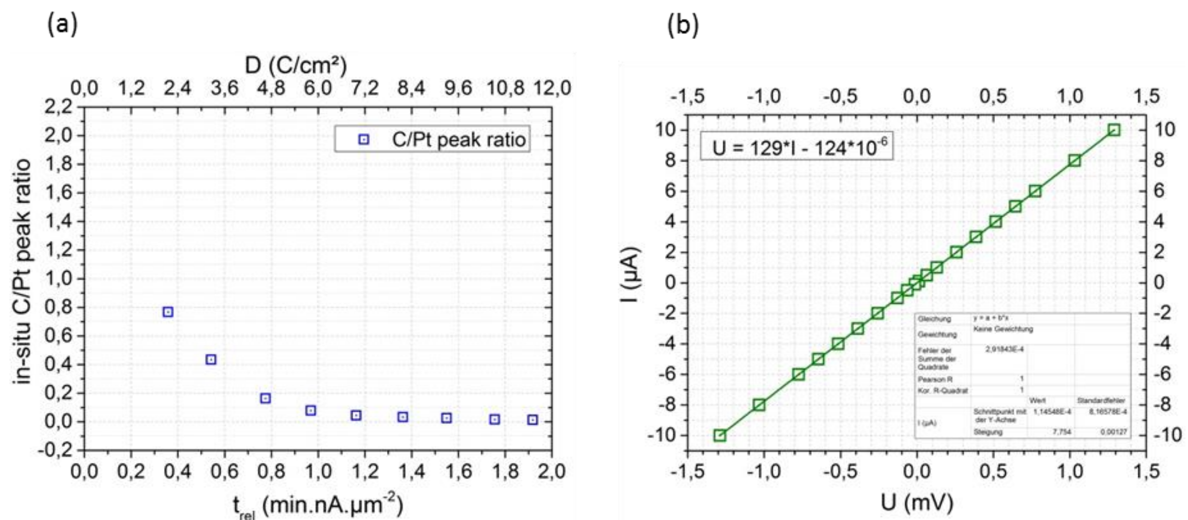

Figure 31: (a) Time evolution of the in-situ EDXS C/Pt peak ratio during the purification of the 1st Pt layer of pad 1. The saturation behaviour shows that the structure is fully purified. (b) U/I characterization of the purified 1st Pt layer showing a strictly linear behaviour.

Three possible reasons have to be considered to find the answer, why the resistivity of the purified Pt was higher than the bulk resistivity:

1. **Pt layer too thin to show bulk state behaviour:** As previous examinations of the resistivity of Pt thin films showed [50], the biggest change takes place until 10nm film thickness. For thicknesses larger than 10 nm the resistivity still decreases with increasing thickness, but at a much smaller rate (transition from quasi-2D to 3D transport). For a film thickness of 100 nm the resistivity is only approximately halved compared to 10 nm thickness. [50]
2. **Height of the Au electrodes leads to contact problems:** Since the Au electrodes form 50 nm high steps on the substrate and the Pt layers are quite thin compared to that, it's not sure if the contact between the electrodes and the platinum is optimal. This critical region is marked by an orange arrow and description in Figure 36 (a) showing a FIB crosscut of pad 1 after the experiments.
3. **Nano-voids and grain boundary electron scattering:** However, we know already from TEM investigations in the frame of the master thesis of B. Geier [2,3], that fully purified deposits consist of Pt grains with a diameter of 6 – 9 nm. Electron scattering at grain boundaries and nanovoids could be responsible for the higher resistivity compared to the reference value for bulk state Pt.

Since the purified Pt has a thickness of only 24 nm, a 2nd Pt-C layer with a height of 75 nm was deposited on top of the 1st, fully purified, layer to reach a more bulk state behaviour in case the layer thickness is the problem. The purification for the 2nd Pt-C layer was done with the same parameters as the purification for the 1st layer with exception of a slightly higher purification dose of 18.6 C/cm² (80 min purification time). After the 2nd purification, a final resistivity of $180\ \mu\Omega\ cm$ was determined for the 2, fully purified, Pt deposits with a total height of 48 nm. By adding a second purified layer and doubling the layer thickness, the resistivity is approximately halved but still 17 times higher than the bulk value for pure Pt.

To make sure that the height of the Au electrodes doesn't prevent a better resistivity value, for pad 2 the electrodes were thinned via FIB milling before the deposition. The parameters for the FIB milling were 30 keV, 30 pA, 8 nm PoP, 1 µs DT, $12 \times 4\ \mu m^2$ thinning area and a milling duration of 60 s. In Figure 32 the SEM image after the FIB milling can be seen. Afterwards a Pt-C layer with a height of 105 nm was deposited leading to an expected height of 32 nm for the fully purified deposit.

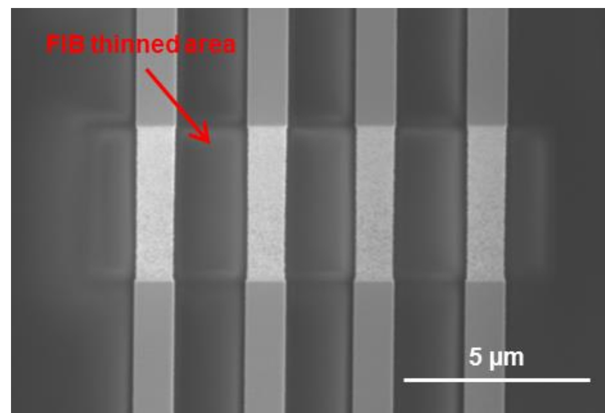

Figure 32: SEM image of the thinned gold electrodes via FIB milling.

For pad 2 the resistance and the resistivity were not only measured after purification but also *in-situ* during it. Simultaneously, the C/Pt peak ratios from the EDXS data were recorded. In the beginning the purification parameter were 5 keV, 4.3 nA, 1 µs DT, 8 nm PoP, a H_2O pressure of 10 Pa and a purification field of $16 \times 3\ \mu m^2$. The *in-situ* time evolution of the C/Pt peak ratio together with the *in-situ* time evolution of the resistance can be seen in Figure 33 (a). An interesting aspect is that while the C/Pt peak ratio starts decreasing after the start of the purification, the resistance increases until a peak at a dose of 6 C/cm² and then decreases. Most likely this initial peak is related to chemical effects. However, it would be necessary to do a more detailed examination to allow conclusions on the exact reason. In Figure 33 (b) beside the resistance on one y-axis, on the 2nd y-axis there can be also seen the resistivity for the expected height of 32 nm after the purification. After e-beam radiation with a dose of 33.5 C/cm² the resistivity of $265\ \mu\Omega\ cm$ was still too high. At this point of the purification the *in-situ* C/Pt peak ratio showed a clear saturation behaviour suggesting that the deposit was C free. In case the grain boundary scattering is the reason for the increased resistivity, the purification dose was increased with the intention to initiate further grain growth. Doing so,

some purification parameters were changed. These periods of varying purification parameters are indicated in Figure 33 (b) by the areas of different colour. After a dose of 33.5 C/cm² the length of the purification window was reduced from 16 µm to 8 µm resulting in the fact, that the outside areas of the 15 µm long deposit were not radiated with electrons anymore (yellow area in Figure 33 (b)). Since the resistance is only measured between the 2 inner electrodes (see chapter 2.4.4), this was not a problem. The parameter variation also resulted in a decrease of the PoP to 4 nm. After a dose of 64 C/cm² the current was slightly raised to 5.6 nA (orange area in Figure 33 (b)) and finally, after a dose of 183 C/cm², the current was strongly raised to 13.1 nA (red area in Figure 33 (b)). Finally, at an electron dose of 282 C/cm² the purification was ended. Between the end of the green coloured period and the purification end, the resistivity only decreased from $250\ \mu\Omega\ cm$ to $150\ \mu\Omega\ cm$, although an electron dose of almost 250 C/cm² was applied. Apparently the extremely high dose didn't have the intended effect.

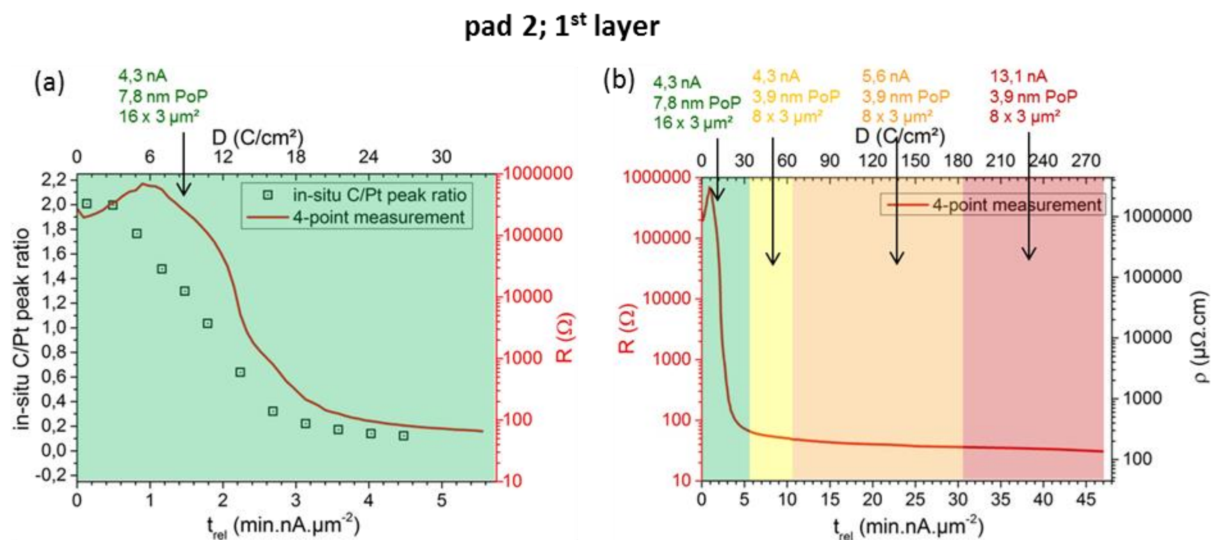

Figure 33: (a) Time development of the in-situ C/Pt peak ratio and the in-situ resistance (2 y-axes). The initial peak of the resistance, while the C/Pt peak ratio constantly decreases, is probably chemically relevant. (b) Time development of the resistance and resistivity of the entire purification process (resistivity for the expected final thickness of 32 nm of the fully purified layer). The periods marked with different colours represent different purification parameters. Those purification parameters, which were changed in regard of the initial purification parameter (current, PoP and purification field size), can be found in the same colour above the diagram. The green marked area is the period seen in more detail in (a).

On top of the 1st layer of pad 2 a second Pt-C layer with an thickness of 75 nm was deposited. After being fully purified, this results in a Pt layer with a thickness of 24 nm. The starting parameters for the purification were 5 keV, 2.1 nA, 1 µs DT, 7.8 nm PoP, a purification area of $16 \times 3.5\ \mu m^2$ and a H_2O pressure of 10 Pa. The time evolution of the resistance and the resistivity during the purification of the 2nd Pt layer can be seen in Figure 34 (a). After reaching a dose of 4.5 C/cm² the current was raised to 4 nA and after a total dose of 39.2 C/cm² the purification was ended. The final resistivity at the end of the purification stayed basically the same ($144\ \mu\Omega\ cm$) as for 1st Pt layer alone. Though, a

3rd Pt-C layer, again with a height of 75 nm, was deposited on top of the first 2 layers. In the beginning the purification parameters for the 3rd layer were the same as for the 2nd layer, with exception of a current of 4 nA. The time development of resistance and the resistivity during the purification of the 3rd Pt layer can be seen in Figure 34 (b). Since the decrease of the resistivity slowed down and the trend leaded to values still larger than hoped for, after a dose of 21 C/cm² the primary beam energy was changed to 20 keV. Still the trend of decrease did improve only for a short time and after a dose of 43 C/cm² the primary beam energy was changed back to 5 keV, the current was raised to 15 nA and, same as for the 1st layer, the length of the purification frame was reduced from 16 µm to 8 µm. The purification was ended after a total dose of 429 C/cm² with a final resistivity being approximately the same as after the 1st layer ($147\ \mu\Omega\ cm$).

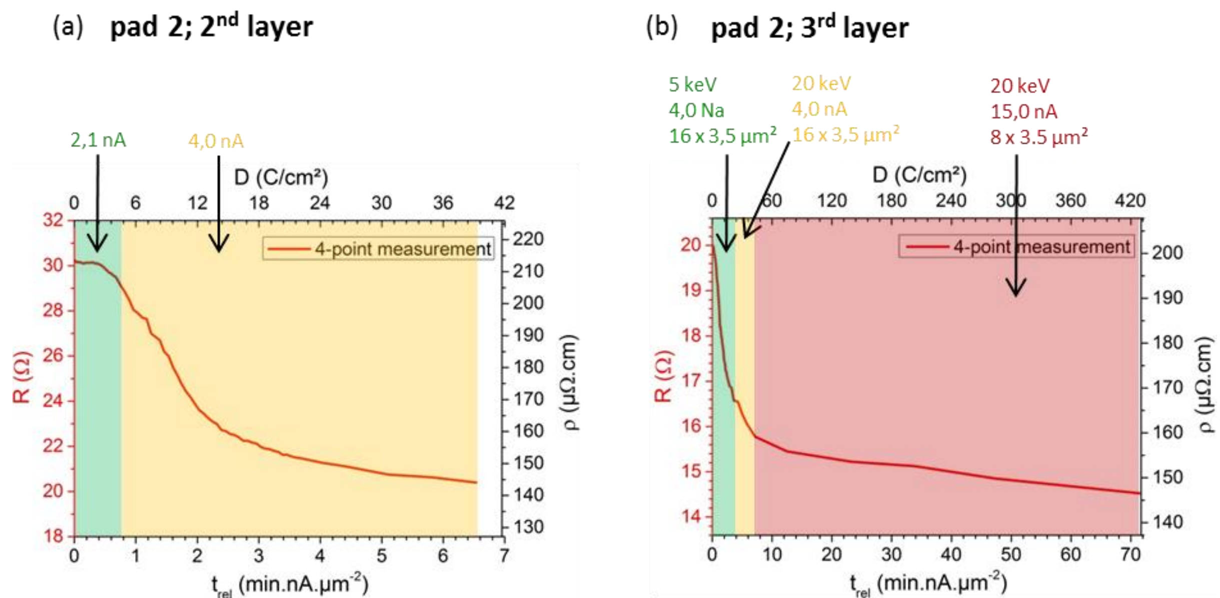

Figure 34: (a) time development of the resistance and the resistivity measured in-situ during the purification of the 2nd layer of pad 2. The final height of the 2 layers after full purification was 56 nm. (b) time development of the resistance and the resistivity measured in-situ during purification of the 3rd layer of pad 2. The final height of all 3 layers after full purification was 80 nm. In both diagrams the periods marked with different colours represent different purification parameters. Those purification parameters, which were changed in regard of the initial purification parameters (current, primary beam energy, purification field), can be found in the same colour above the diagram.

As can be seen in Figure 35 (a), the U/I characterisation of pad 2 with all 3, consecutively purified layers shows, apart from a different resistance value, the same strictly linear behaviour as for only 1 purified layer (see Figure 31 (b)). However, after the purification of the 3rd layer, the deposit looked awful with some kind of bubbles on the surface, as can be seen in Figure 35 (b). Probably they have formed due to the very high dose and current applied during the purification of that layer. These effects haven't been observed during any other purification process before.

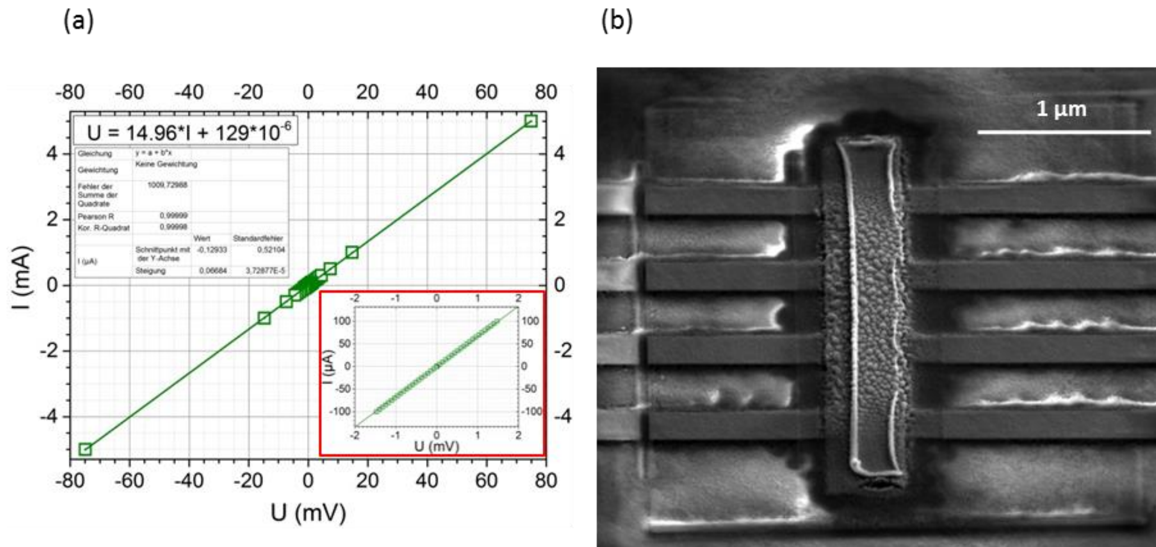

Figure 35: (a) U / I characterization of pad 2 after full purification of all 3 layers of Pt deposit. The inset shows the U / I diagram between -2 mV and 2 mV enlarged. Like for 1 Pt layer (see Figure 31 (b)) it shows a strongly linear behaviour. (b) SEM image of pad 2 after the purification of the 3rd deposit layer. The surface looks bad and some kind of bubbles can be seen, which formed probably due to the very high dose.

3.1.4.1 Internal Structure of the Deposits for Electric Characterization

To better understand why the resistivity was significantly larger than the Pt bulk value, FIB crosscuts were done on pad 1 and pad 2. The SEM images of these crosscuts can be seen in Figure 36 (a) and (b). The 2 Pt layers of pad 1 were purified respectively with relatively low doses. In Figure 36 (a) the boundary layer between the 2 Pt layers can't be seen. On the contrary for pad 2, which can be seen in Figure 36 (b), respectively relatively high doses (higher by the factor 2.5 – 29.0 compared to pad 1) were used to purify the layers. Between the layers there can be clearly seen what seems to be layers of contamination. The thickness of these contaminations seems to be influenced by the dose, which was applied to purify the layer. For example, the contamination layer above the 1st Pt layer is clearly thicker than the contamination above the 2nd Pt layer. The 1st Pt layer got purified with a dose 7 times higher than those for the 2nd Pt layer. Above the 3rd Pt layer, which had received the highest purification dose, the bubbles which were already seen in the normal SEM image in Figure 35 (b), can be also seen in the crosscut in Figure 36 (b).

To better understand the internal structure, a TEM lamella from pad 2 was prepared and investigated in a TF-20 microscope. The STEM mode HAADF image (light elements dark, heavy elements bright) of the 3 Pt layers can be seen in Figure 37 (a), with the Pt layers being the bright stripes running from the top to the bottom. A STEM EELS line-scan, whose track is marked by the green line in Figure 37 (b), was made across the 3 Pt layers. The dynamic profile of the amount of electrons with an energy loss between 278.5 eV and 350 eV, which corresponds to the relative carbon ratio along the line-scan, can be seen in Figure 37 (b). At the positions of the platinum layers, the relative carbon ratio is zero. Between the Pt layers in the contamination layers (see Figure 36 (b)), the relative carbon ratio is high. This leads to the conclusion that the contamination layers mainly consist of carbon, while the Pt layers are carbon free. The contaminations were probably brought on top of

each deposit layer by residual gas deposition (chamber contaminations) during purification. High doses and currents severely enlarge this effect.

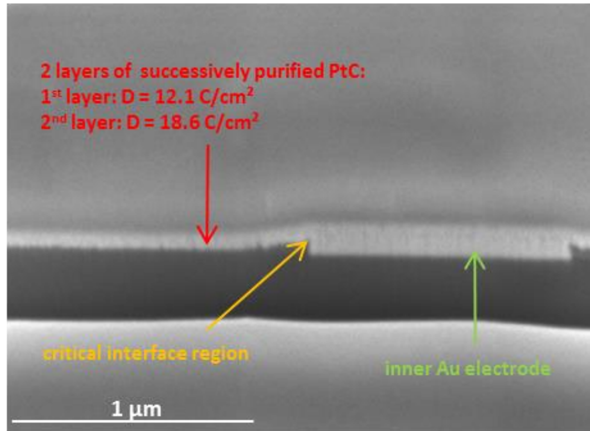

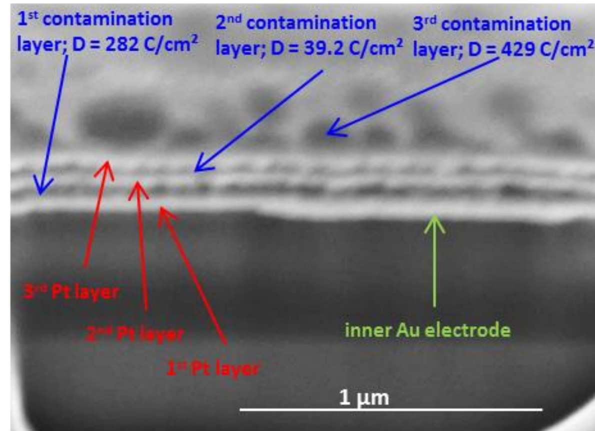

Figure 36: (a) Crosscut through pad 1 after the successive production of 2 Pt layers. The purification dose was respectively relatively low and the boundary layer between the 1st Pt layer and the 2nd can't be seen. (b) Crosscut through pad 2 after the successive production of 3 Pt layers. The purification dose was respectively relatively high. Therefore, between the single Pt layers there can be seen contamination layers (dark). The thickness of these contamination layers corresponds to the dose applied during purification.

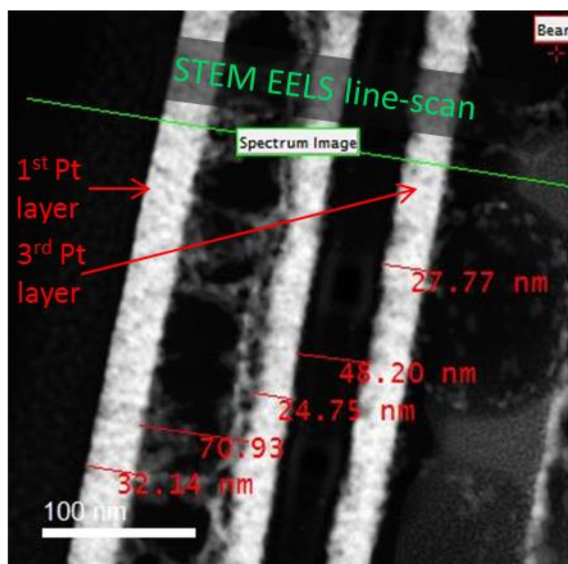

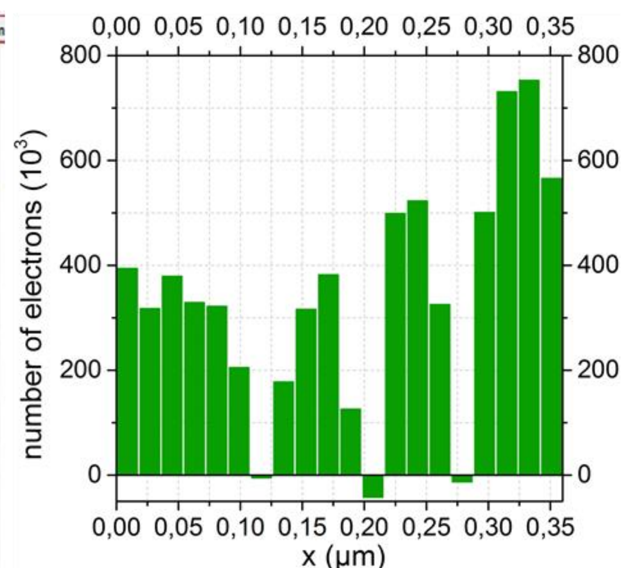

Figure 37: (a) STEM mode HAADF image of the 3 purified Pt layers (bright) of pad 2 with carbon contamination layers (dark) in between. The green line marks the track of the STEM EELS linescan. (b) dynamic profile of the amount of electrons with an energy loss between 278.5 eV and 350 eV along the STEM-EELS linescan, which corresponds to the relative carbon ratio along the linescan. The 3 areas where the relative carbon ratio is 0 correspond to the Pt layers in (a).

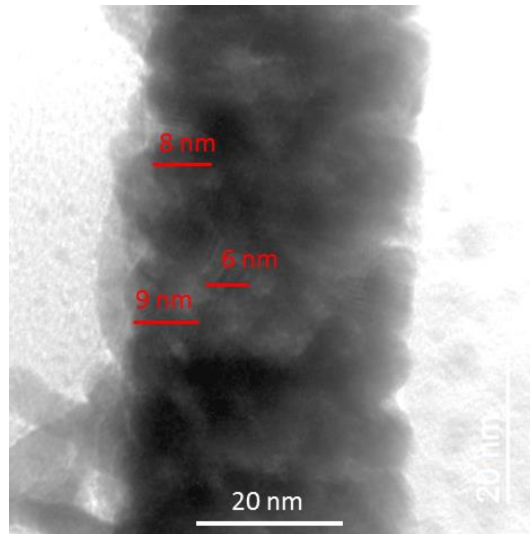

Figure 38: BF image of the, fully purified, 1st Pt layer (dark) of pad 2. As an example, the size of three grains can be found in the image. As expected and already observed by B. Geier [2,3] the grain sizes of the purified Pt lay between 6-9 nm.

A BF image (providing higher resolution than a HAADF image) of the purified 1st Pt layer can be seen in Figure 38. In this image, in the opposite way of Figure 37 (a), the Pt layer is dark while the surrounding carbon is bright. The single Pt grains, which can be seen in the image, have a size between 6-9 nm as already reported by B. Geier et.al. [2,3].

The conclusion of these experiments is that by purification a resistivity of 180 µΩ cm can be reached which is approximately 17 times higher than the reference value for bulk state Pt. This is the resistivity reached for pad 1 with 2 Pt layers, which can be considered as more exact. The reason for this is that the contamination layers between the Pt layers of pad 2 (dark layers in Figure 37 (a)) influenced the resistance and thereby distort the resistivity. Some of the current might have flowed over the contamination layers. Although the resistivity measurement from pad 2 was distorted, it can be concluded from the resistivity measurement result of 144 µΩ cm, which was not significantly lower than the result of pad 1, that the pre-thinning of the gold electrodes of pad 2 (see Figure 36 (b)), had no major effect. This leads to the conclusion that the height of the gold electrodes can be excluded as reason for the high resistivity. The resistivity might be slightly reduced by raising the layer thickness, but a Pt layer thickness of 48 nm (for the 2 layers of pad 1) is already in an area where the thickness has only a minor influence on the resistivity [50]. The reason for the higher resistivity is very probable electron scattering at grain boundaries and nano-voids. Because of the contamination the data are unfit to conclude, if applying very high doses after the deposit is already carbon free, leads to additional grain growth and thereby lowers the resistivity. The occurrence of contamination layers when high doses are applied is a problem which needs to be overcome. Until then it’s necessary to choose a dose for the purification, which is high enough to fully purify the deposit but not higher than necessary. For deposits in the scale above 1 μm^2, the C/Pt ratio proved as a reliable characteristic on the Si wafer substrate. Nevertheless this demonstrates the importance of the post purification cleaning method, which was developed in the frame of this thesis (see chapter 3.2.4).

3.1.5 FEBID Modification of Self-Sensing Cantilevers for Electric Measurements

After the ideal purification beam energy was determined and the electrical investigations revealed that the resistivity of purified deposits was good but not perfect (more than ten times larger than the bulk resistivity of Pt), the fabrication of the special cantilevers could be started.

3.1.5.1 Provided Cantilevers

SCL provided the cantilevers for the modification experiments (see Figure 39 (a)). These cantilevers can be divided into 2 groups according to the length of the cantilevers, which results in different spring constants: The 350 µm long cantilevers, which are going to be referred as CL-L (Figure 39 (b)) and (c)) and the 30 µm long cantilevers, which are going to be referred as CL-S (Figure 39 (d) and (e)).

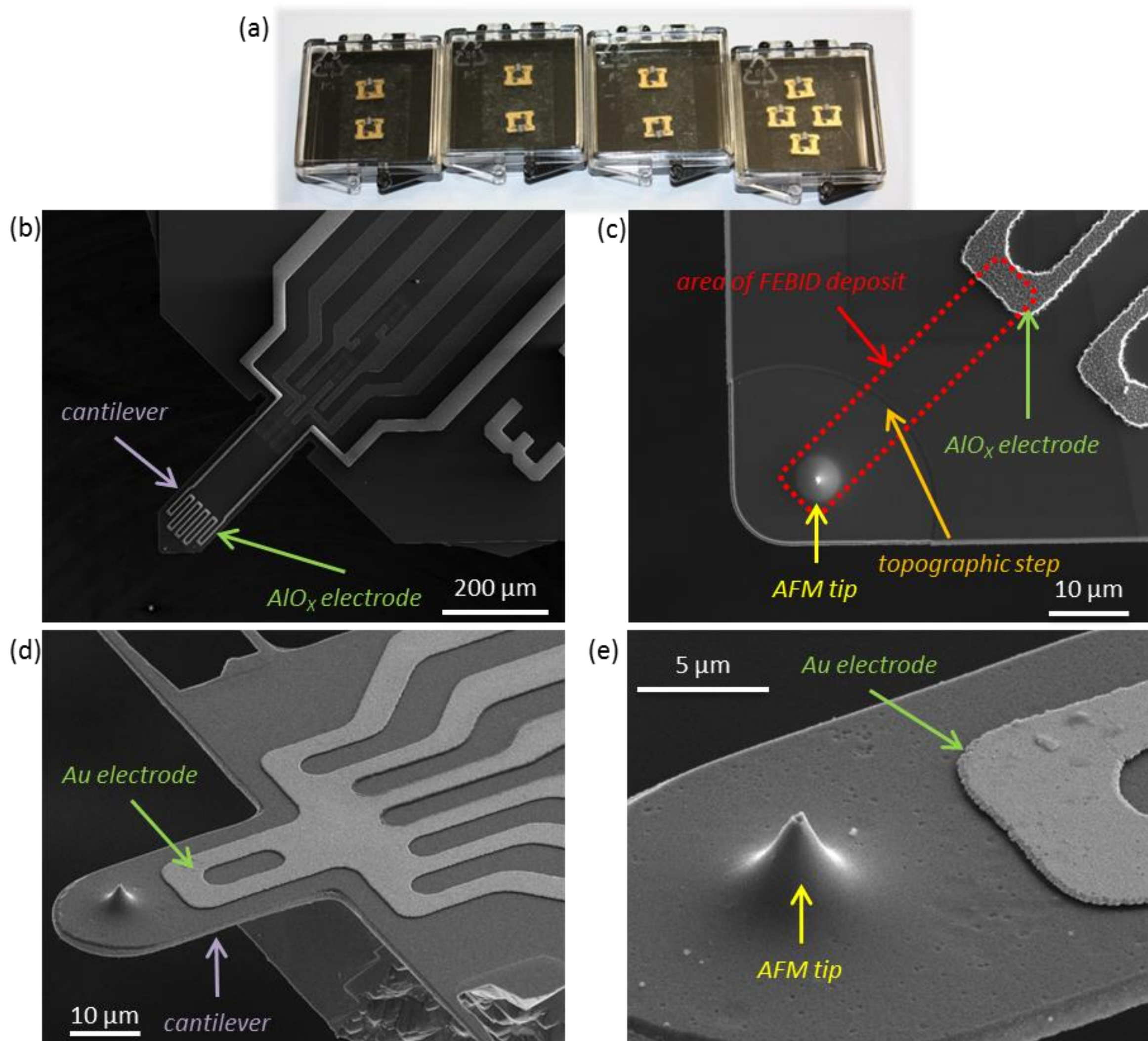

Figure 39: (a) SS-CL provided by SCL. 2 types of cantilevers were used for the experiments. (b) and (c) show the 350 µm long cantilevers (CL-L 1). These cantilevers have an additional topographic step (orange) and the area to be coated with a highly conductive layer is marked by the red square. (d) and (e) show the short cantilever type, a 30 µm long cantilever. The distance to be coated is much larger for the long cantilevers (CL-L) than for the short ones (CL-S).

3.1.5.2 Modification

In total four cantilevers, two CL-L with the electrode made out of AlO_X and two CL-S with the electrode made out of Au, were modified. To differentiate easy between them, they are going to be referred by the names of:

- **CL-L 1:** 350 µm long cantilever with AlO_X electrodes (Figure 39 (b) and (c))
- **CL-L 2:** 350 µm long cantilever with AlO_X electrodes
- **CL-S 1:** 30 µm long cantilever with Au electrodes
- **CL-S 2:** 30 µm long cantilever with Au electrodes

All the parameters for the deposition coating and other modifications done on the cantilevers can be found in Table 1. The deposition heights there are the as-deposited heights. To receive an approximate height for the purified deposition, these values have to be divided by 3. All the purification parameters can be found in Table 2. The time development of the *in-situ* C/Pt peak ratio can be found in Figure 40. CL-L 1, CL-L 2 and CL-S 2 clearly show the expected saturation behaviour. However, the C/Pt peak ratios for CL-S 1 and CL-S 2 are in general higher than for the other two cantilevers. The reasons for this are the substrate reference spectra which are subtracted from the spectra during purification (see chapter 2.4.1). A false value on this substrate reference, leads to wrong absolute C/Pt values. On the small cantilevers, it was not clear which places were suitable to take the reference spectra and therefore, non-optimal reference spectra were gained. The purification of CL-S 1 doesn't show a clear saturation behaviour but a tendency towards it. Beside the reference spectra problematic, the reason is that it was tried to use the lowest possible dose and finish the purification when the in-situ surveillance, which is less exact, indicates that the deposit is carbon free.

After the purification, some cantilevers were cleaned with O_2 plasma to remove contaminations (see chapter 3.2.4). The applied plasma cleaning times, can be found in Table 2.

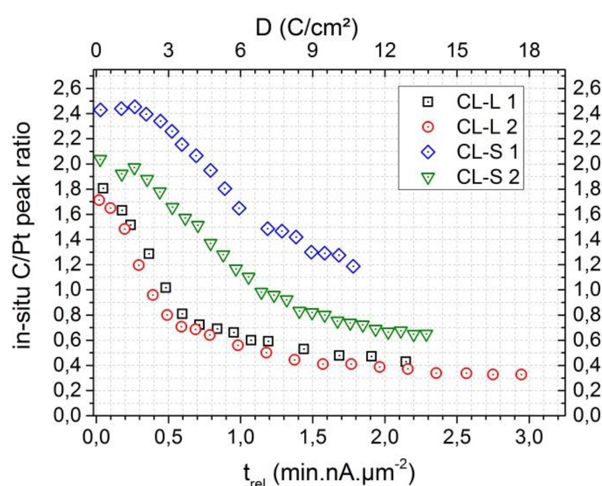

Figure 40: Time development of the in-situ C/Pt peak ratio during the purification of the FEBID coatings of the 4 cantilevers. The C/Pt values of all 4 purification procedures show clearly a saturation behaviour leading to the conclusion that the carbon removal was successful.

Table 1: Overview of the cantilever modification FEBID parameters. 4 different cantilevers were modified, two long (CL-L) and two short cantilevers (CL-S).

Name	CL-L 1	CL-L 2	CL-S 1	CL-S 2
Serial Number	B-V.01 173	B-V.01 167	V.01 9	V.01 98
Au Electrode thinning via FIB				
	No	No	Yes	Yes
electrode material	ALO_X	ALO_X	Au	Au
Primary energy			30 keV	30 keV
Current			30 pA	30 pA
DT			1 µs	1 µs
PoP			8 nm	8 nm
Thinning area			2 x 5.3 µm²	3 x 7.3 µm²
Thinning time			20 s	40 s
Pt-C deposition via *working GIS*				
Primary energy	5 keV	5 keV	5 keV	5 keV
Current	1.6 nA	1.6 nA	1.6 nA	1.6 nA
DT	100 µs	100 µs	100 µs	100 µs
PoP	13 nm	13 nm	13 nm	13 nm
Number of passes	5	6	7	8
Deposition height	38 nm	45 nm	54 nm	61 nm
Patterning footprint	37 x 3 µm²	37 x 3 µm²	15 x 5 µm²	15 x 5 µm²
2nd Pt-C layer across the across the electrode – deposition interface (same primary energy, current and DT as above)				
defocus			0 µm	250 µm
PoP			13 nm	110 nm
Number of passes			11	748
Deposition height			82 nm	82 nm
Patterning footprint			4 x 5 µm²	4 x 5 µm²
3rd Pt-C layer across the across the electrode – deposition interface (same primary energy, current and DT as above)				
defocus				250 µm
PoP				110 nm
Number of passes				515
Deposition height				61 nm
Patterning footprint				2 x 5 µm²
FEBID nanopillar as new, sharp tip				
	Yes	Yes	Yes	No
Primary energy	5 keV	5 keV	5 keV	
Current	5 pA	5 pA	5 pA	
Deposition time	10 s	10 s	10 s	
Height	600 nm	600 nm	600 nm	

Table 2: Overview of the purification parameters and the plasma cleaning steps for the four modified cantilevers. The purified main height means the height of the 1st deposit layer after purification without the height of optional additional depositions in the interface area (see Table 1).

Name	CL-L 1	CL-L 2	CL-S 1	CL-S 2
Serial Number	B-V.01 173	B-V.01 167	CL 9	CL 98
Purification parameters				
Primary energy	5 keV	5 keV	5 keV	5 keV
Current	3.1 nA	3.1 nA	1.9 nA	1.9 nA
DT	1 µs	1 µs	1 µs	1 µs
PoP	19.0 nm	18.1 nm	7.8 nm	8.7 nm
H_2O pressure	10 Pa	10 Pa	10 Pa	10 Pa
Purification field	39 x 5 µm²	37 x 6.4 µm²	16 x 6 µm²	18 x 6 µm²
Purification time	137 min	231 min	94 min	133 min
Dose	13.1 C/cm²	18.3 C/cm²	11.3 C/cm²	14.0 C/cm²
purified main height	13 nm	15 nm	18 nm	20 nm
O_2 plasma cleaning				
1st plasma cleaning	10 min		20 min	20 min
2nd plasma cleaning			15 min	10 min

3.1.5.2.1 Cracks in the Electrode Deposition Interface

A problem, which occurred during coating, concerned the interface region between the Au electrode and the purified Pt. The electrodes are up to 900 nm high. This is very high in relation to the purified Pt deposits, which were not more than approximately 20 nm high. In Figure 41 (a) the interface region between the AlO_X electrode of CL-L 2 and the un-purified FEBID Pt-C layer can be seen. Although the high difference was huge, no cracks could be seen in the interface area. However after purification, as can be seen in Figure 41 (b), the interface showed long cracks (orange arrow) due to the volume loss during purification. Probably, these cracks influenced the conductivity negatively.

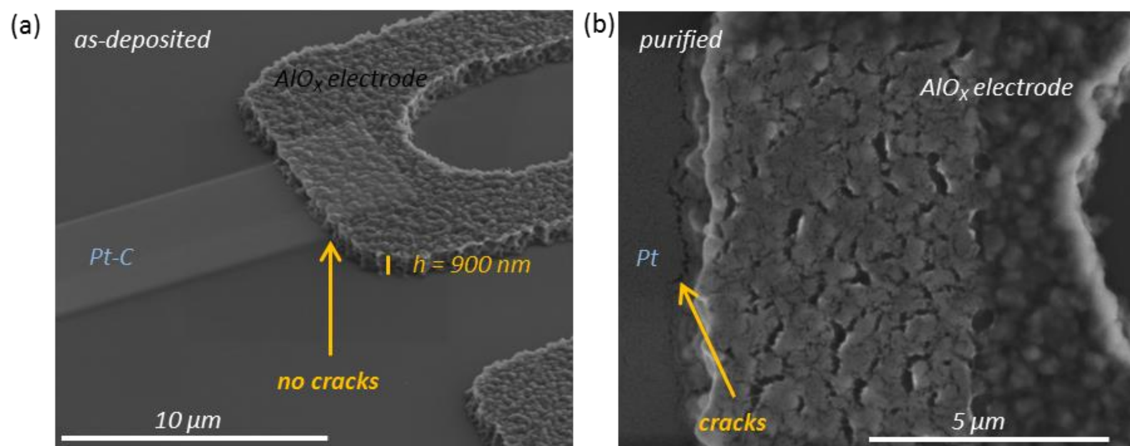

Figure 41: SEM images of the coating on CL-L 2 at the electrode-deposit interface. (a) shows the as-deposited Pt-C layer were no cracks are visible in the interface area. (b) shows the interface area after purification enlarged and perpendicular from above. Marked by the orange arrow there can be seen cracks, which influence negatively the electrical conductivity.

To overcome this problem, a 2 step solution was chosen. The first step was to pre thin the electrodes to reduce the height difference. Figure 42 shows a SEM image of the pre thinned Au electrode of CL-S 1 after 20 s of FIB milling (the exact parameters can be found in Table 2).

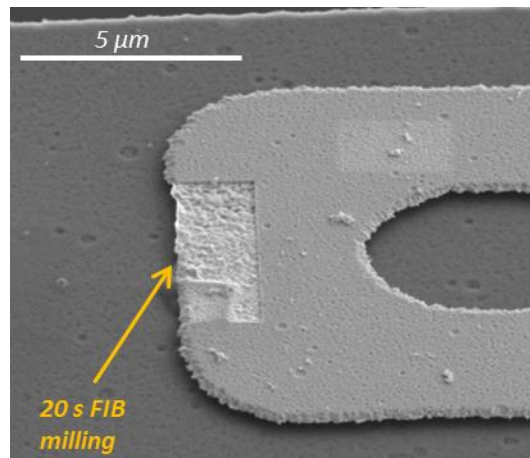

Figure 42: Pre thinned area of the Au electrode of CL-S 1 after 20 s of FIB milling.

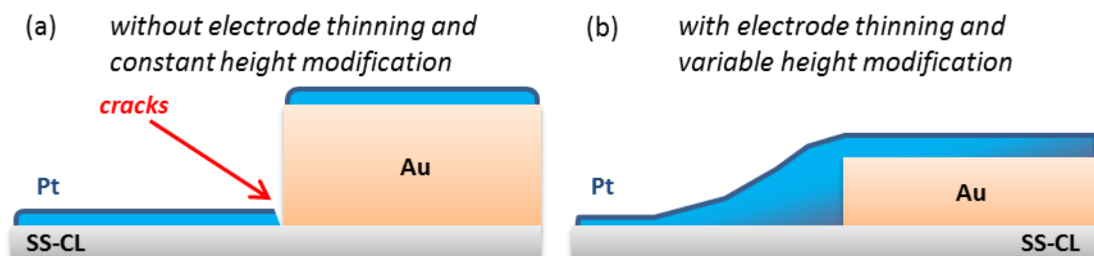

Figure 43: (a) Pt coating without electrode thinning and constant height modification. There appear cracks in the interface area between the electrode and the deposit. (b) Strategy to prevent the appearance of cracks in the interface area. First the Au electrode is pre-thinned and then at the interface region additional layers are deposited on top of the 1st layer to accomplish a smooth topographical shape.

As second step, in the interface area of the Au electrode and the Pt deposit, additional Pt depositions leading to a variable height modification were made. These were supposed to smooth the topographical shape in the interface area, which can be seen in Figure 43.

In the case of CL-S 1 after pre-thinning and deposition of a 54 nm high 1st Pt-C layer in the interface region of the electrode and the deposit, a second Pt-C layer with the same parameters and a height of 82 nm was deposited (for detailed parameters see Table 1). While, for the deposit before purification there weren't any cracks visible in the SEM images (see Figure 44 (a)), after purification cracks appeared in the coating, as can be seen marked by the orange arrow in Figure 44 (b). However, these cracks were not located at the interface of the electrode and the Pt layer, but at the

edge of the 2nd Pt layer on top of the 1st one, leading to the conclusion that the interface of the two Pt layers was the problem.

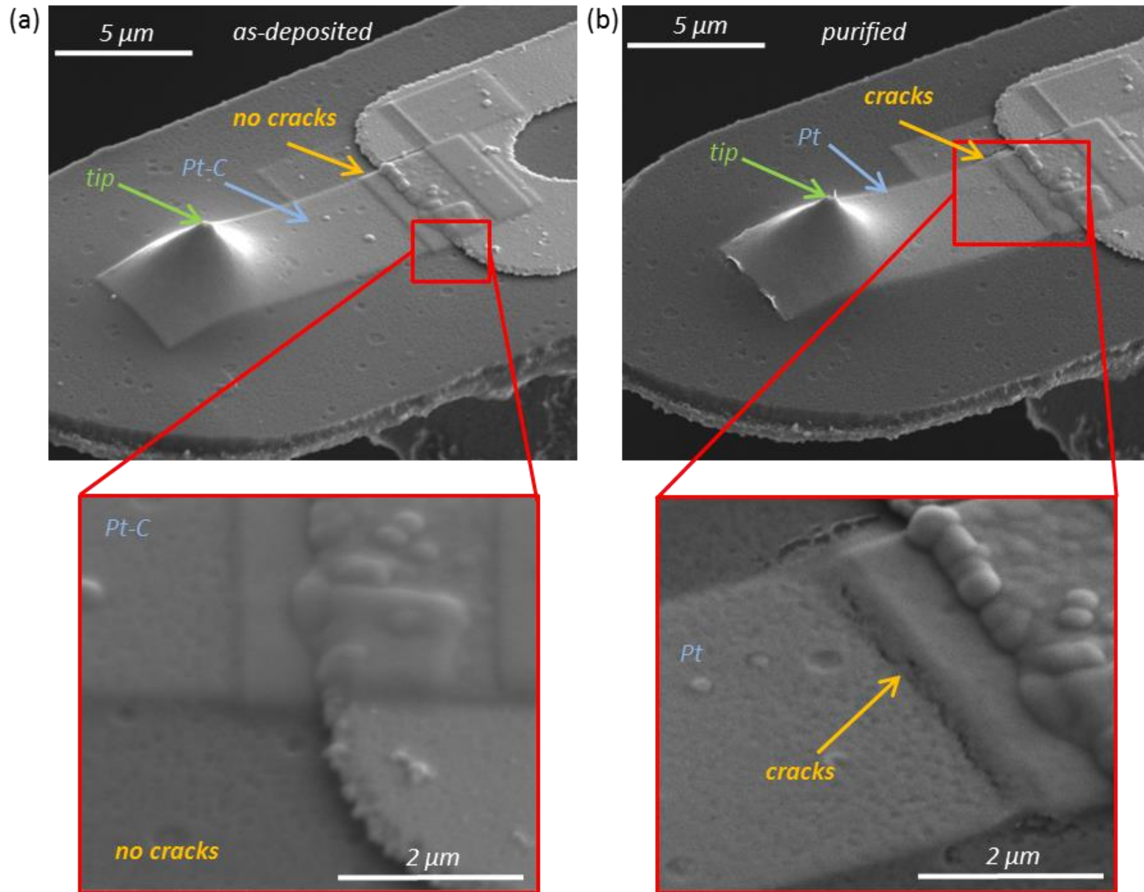

Figure 44: Coating of CL-S 1 with pre-thinning of the electrode and variable height deposition in the interface area. The red edged images below are more detailed images of the interface area. (a) shows the Pt-C deposit before purification. There are no cracks visible in the interface area of the Au electrode and the deposit. (b) shows the Pt-C deposit after purification. Although no cracks can be seen in the interface area, there are cracks exactly at the edge of the 2nd Pt layer marked by the orange arrow.

Therefore, for CL-S 2, after the deposition of a 61 nm high 1st layer, a 2nd layer with an approximate height of 81 nm and a 3rd layer with an approximate height of 61 nm were deposited in the interface area between the electrode and the 1st deposit. For the depositions at the interface area (2nd and 3rd layer) a defocus of 250 µm for the electron beam was chosen (for more deposition details see Table 1). While, as usual, there are no cracks visible in the interface area between the Au electrode and the deposit (see Figure 45 (a)), using the defocused electron beam results also in a crack free interface area after the purification, as can be seen in Figure 45 (b). The reason is that defocusing the electron beam, leads to a less sharp edge of the Pt-C deposit and therefore to a smoother topography along the deposit than if no defocus is used. The interface deposition strategy for CL-S 2 resulted clearly in the best, crack free interface region.

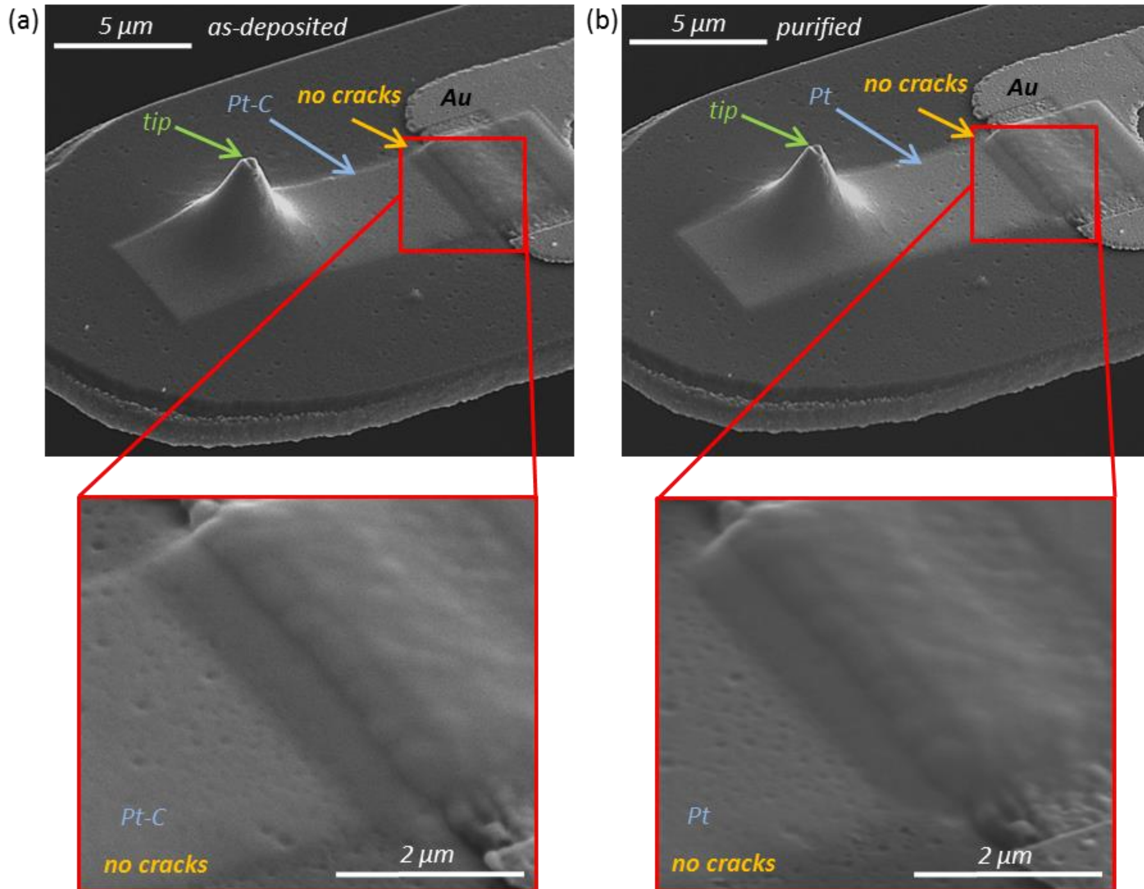

Figure 45: Coating of CL-S 2 with pre-thinning of the electrode and variable height deposition in the interface area using a defocused electron beam to add 2 additional layers (for more detail see Table 1). The red edged images below are more detailed images of the interface area. (a) shows the Pt-C deposit before purification. (b) shows the Pt-C deposit after purification. With this deposition strategy in the interface area, also after the purification, cracks could be completely prevented.

3.1.5.2.2 Modification of the Cantilever Tip

As can be seen in Figure 25 (a), coating of an AFM cantilever leads, independently from the used method, to a broadening of the AFM tip. However, a fine tip radius can be important or even essential for C-AFM measurements. Therefore, the capability to produce so called nano-pillars was used to receive a sharp tip. As already shown by B. Geier[2,3] purified nano-pillars, while having a diameter of approximately 60 nm, can have a tip radius of less than 10 nm, making them very well suitable for AFM tips (see Figure 48 (b)). Therefore, after coating the cantilever with a Pt-C layer, on some of the cantilevers (see Table 1) a Pt-C nano-pillar was deposited on the AFM tip. This took only 10 s production time. In Figure 46 (a) there can be seen CL-L 2 before purification after the coating and the deposition of the nano-pillar on the AFM tip. In the enlarged part, the tip can be seen showing a diameter of only 50 nm. For CL-L 2 the AlO_X electrode was not thinned. After purifying CL-L 2 with a dose of 18.3 C/cm² (see Table 2), the diameter of the tip had grown to approximately 60 nm, as can be seen in Figure 46 (b).

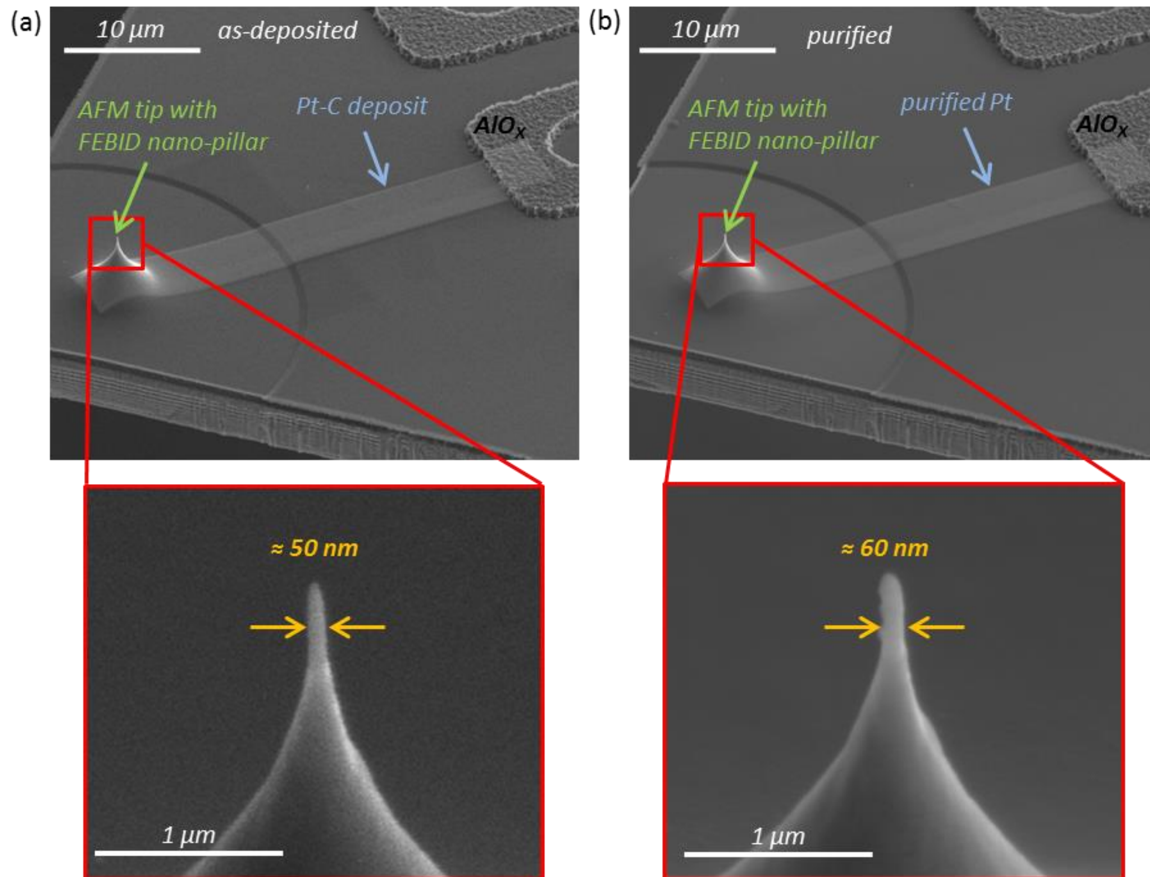

Figure 46: Coating of CL-L 2 with Pt-C via FEBID technique including the production of a FEBID nano-pillar as a new, sharp AFM tip to compensate the natural tip due to the coating. The red edged images below show the tip and the FEBID nano-pillar on top in high resolution. (a) shows the FEBID modifications before purification (b) shows the modifications after purification. The red edged images of the tip in high resolution show that the diameter of the nano-pillar grew by a small amount during the purification.

A huge advantage of the coating technique using FEBID and e-beam purification is the fact that non-sharp AFM tips can be repaired by depositing such a nano-pillar. This can be seen in Figure 47 (a) for CL-S 1 where the tip is broken and has a radius of a few hundred nanometres. The images after purification show again that the diameter of the nano-pillar, contrary to the expected volume loss, increased (see Figure 47 (b)). As Figure 47 (c) shows, an oxygen plasma cleaning step (see chapter 3.2.4) could reduce the diameter of the nano-pillar but it still stayed thicker than the as-deposited one. Further experiments specializing on the nano-pillar purification behaviour in the frame of the Dissertation Thesis of J. Sattelkow showed the reason for the thickening of the nanopillars. In Figure 48 (a) a TEM DF image of a purified Pt pillar can be seen. The core of the fully purified pillar consists of compact, pure Pt but around this core a contamination layer has formed. As the investigations of J. Sattelkow showed, these contamination layers form during imaging in the microscope after the purification process. A procedure to prevent the growth of these contamination layers has also been developed. Figure 48 (b) shows a TEM DF image of a nano-pillar where no contamination layer has formed [3].

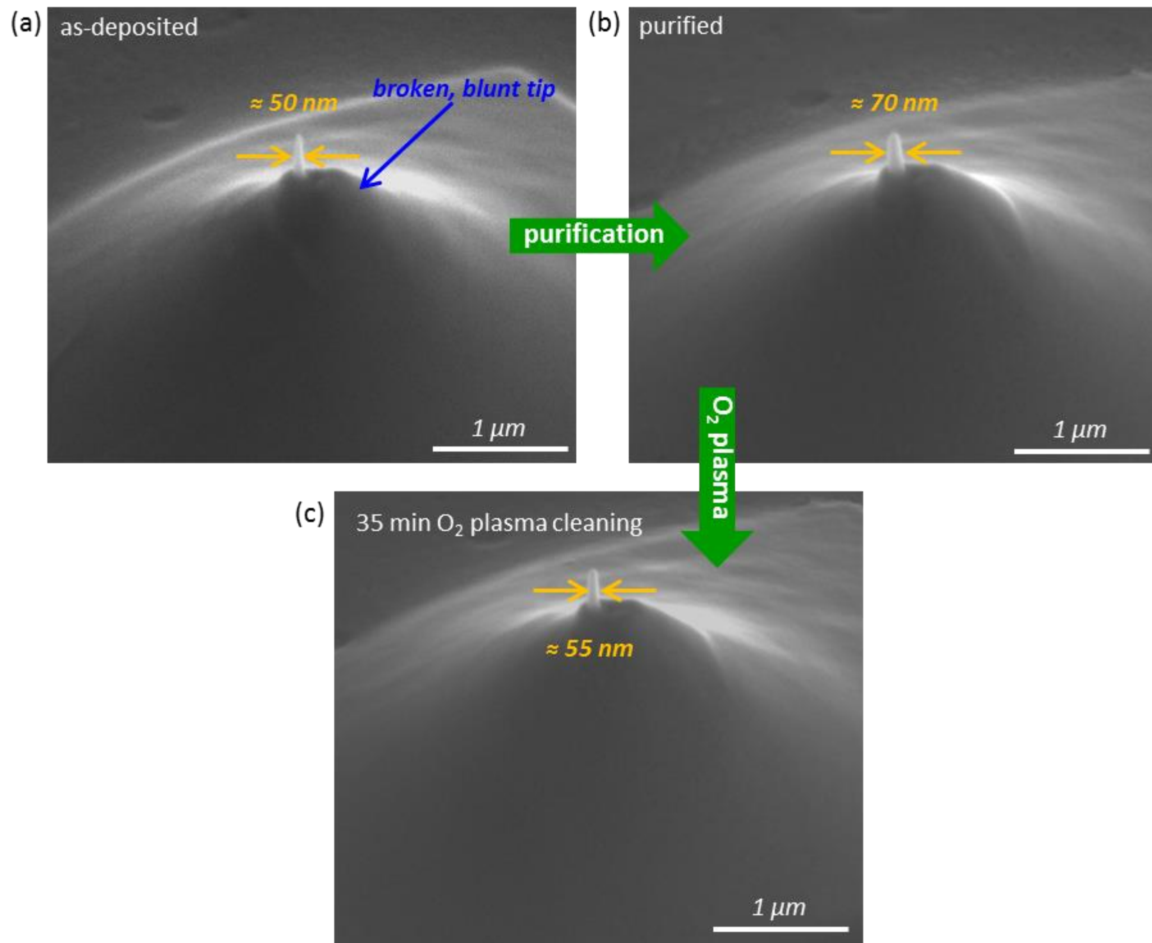

Figure 47: (a) shows the tip of CL-S 1, which was blunt and broken, after coating and the deposition of a FEBID nano-pillar (see Figure 44 for overview images.). The nano-pillar works as a new, sharp tip, which enables to even repair broken tips. (b) shows the nano-pillar on the tip after the purification. During the purification the pillar's diameter grew. (c) shows the nano-pillar after a total time of 35 min of O_2 plasma cleaning.

Also, it has to be mentioned that the chosen purification parameters were ideal to purify the coating layer but not the nano-pillars. First of all, a higher pressure (100 Pa) is desirable to make lateral penetration into the pillar by scattering more probable. Also the ideal purification parameters for nano-pillars are a higher dose (> 100 C/cm²).[2,3] Therefore, finding a purification parameter set being a good compromise between those for the purification of the coating Pt-C layer and those for the purification of the nano-pillar, is promising to further improve the quality of the nano-pillars.

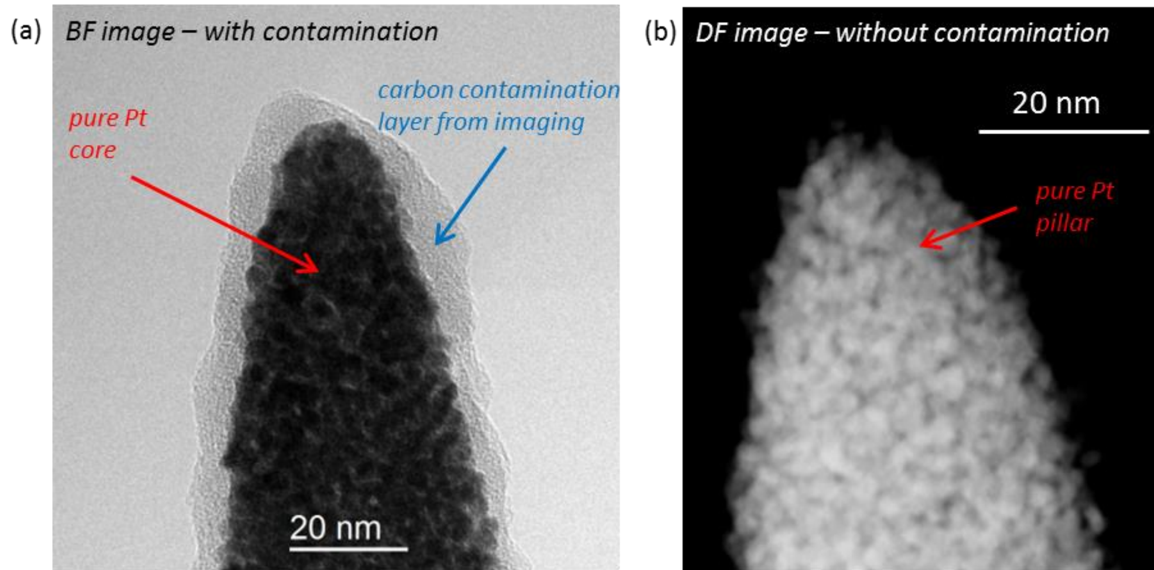

Figure 48: (a) TEM BF image of a purified pillar from further investigations focused on the pillar purification behaviour in the frame of the Dissertation Thesis of J. Sattelkow. It can be seen that inside the pillar there is a compact, pure Pt core which is covered by a contamination layer probably consisting of carbon. As observed by J. Sattelkow this contamination layer is formed during imaging in the SEM after the purification process is finished. (b) TEM DF image of a pure Pt-nano pillar where no contamination layer developed. From [3].

3.1.5.3 Performance Testing

To test if the coating was successful, the modified cantilevers were sent back to SCL. Unluckily the electric circuits of CL-S 1 and CL-S 2 were not correctly contacted by SCL during the production, which made them not usable for performance testing. Therefore, only CL-L 1 and CL-L 2 were used for testing.

To test the performance, the tip of the modified SS-CL was pressed periodically against a highly conductive surface and, like in a C-AFM experiment, the electrical current flowing through the tip was measured. This allowed finding out if the process is repeatable and mechanically stable by multiple circles of pressuring the cantilever against the surface and measuring the current flowing over the tip at the same time. The result can be seen in Figure 49, where both figures have 2 y-axes. The black axis and curve displays the force of the cantilever against the surface and the blue axis and curve display the current flowing over the tip. As can be seen in Figure 49 (a), the current was constant for different measurement cycles which proved the **repeatability** of the conductive sensing process. Figure 49 (b) shows one period in better resolution revealing that after the tip contacted with the surface, the current stayed constant, while the down force was raised. This demonstrated that the Pt coating is **mechanically stable** and doesn't get damaged by the bending of the cantilever, which is very important for the functionality of the concept. Also in Figure 49 (b) shows that the noise of the current during contact is quite low.

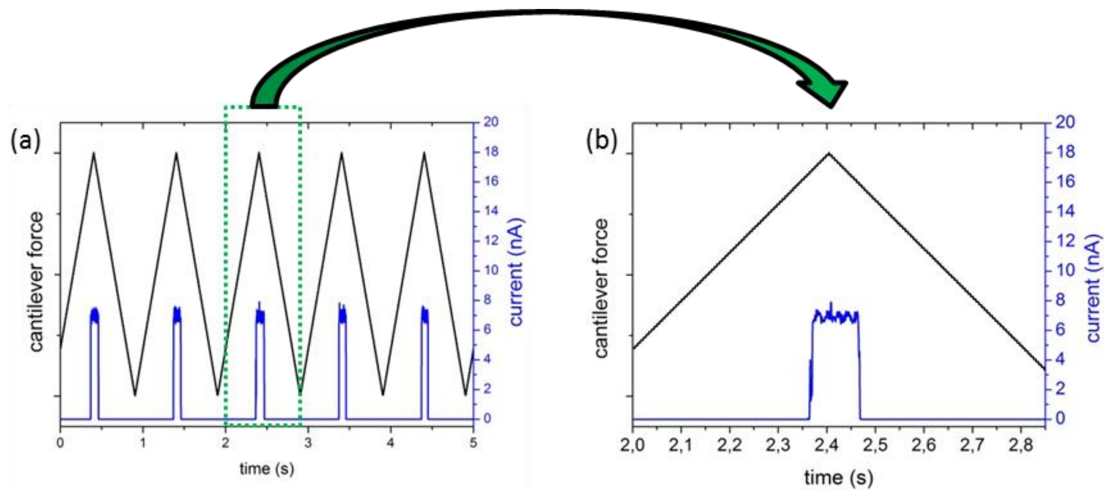

Figure 49: Result of the performance testing of a CL-L type cantilever produced via FEBID and purification technique. The tip of the cantilever was pressed periodically against a conductive surface with a certain force (black axis) and the current flowing over the cantilever was measured (blue axis). (a) shows, that periodical pressure (same force) to the surface results in the same values for the current, which stays constant after the tip contacted the surface and shows that the process is repeatable (b) shows enlarged one period of pressing the cantilever to the surface. The current is approximately constant and doesn't rise with a higher force between cantilever and conductive surface, which demonstrates that the Pt coating is mechanically stable.

First evaluations of the resistance showed relatively high values around 100 kΩ which has 3 reasons:

- The strategy to coat the electrode interface area was not optimal for CL-L 1 and CL-L 2 compared to the other 2 cantilevers (see chapter 3.1.5.2.1). Cracks like in Figure 41 (b), are expected to raise the resistance significantly.
- The contamination layer which formed on the nanopillar also raises the resistance.
- The coating length was long for CL-L 1 and CL-L 2 and the layer thickness of the purified Pt only around 15 nm.

By the usage of smaller cantilevers for coating (smaller electrode – tip distance, which has to be coated), optimized electrodes, layer thickness variation, further improved deposition strategies and the newly developed procedure (by J. Sattelkow) to prevent the formation of the contamination layers on the nano-pillars, the resistance is going to be reduced by more than one magnitude. This reduction would mean that the resistance lays in the area of classical C-AFM specifications.

It has to be mentioned that the resistance values are not corrected by the contact resistance between the SS-CL electrodes and the external electrodes. Future measurements which are going to be corrected by that value are planned in the future on-going of this project. This is also going to improve the received resistance value significantly.

3.1.6 Summary and Outlook

In the 1st part of the master thesis, it could be demonstrated that FEBID is suitable to be used as a direct 3D writing method (3D nano-printer) for local modifications of Self-Sensing Cantilevers (SS-CL). After the purification step to remove the carbon from the coating highly electrical conductive cantilevers can be produced. Experiments conducted by SCL-Sensor.Tech. Fabrication GmbH revealed that the coating is mechanically stable and the characteristic current behaviour repeatable over several measurement cycles.

The purification experiments clearly showed that for Pt-C layers with a thickness of equal or more than 40 nm thickness, like used for the cantilever coating, primary beam energies below 5 keV are not suitable (see chapter 3.1.3).

A set of experiments measuring the resistivity of purified deposits via 4-point measurement, revealed that the best, reliable value, which could be reached, was 180 µΩ cm which is approximately 17 times larger than the bulk value of Pt (see chapter 3.1.4). As reason for this higher resistivity, nano-voids and grain boundary scattering were identified (see Figure 38), which originates from the process of Pt grain growth during the purification process.

For the direct writing via FEBID and the purification step afterwards, it was discovered that a combined strategy of electrode pre-thinning and variable height deposition using a defocused electron beam, leads to the best contact results at the electrode-deposit interface (see chapter 3.1.5.2.1).

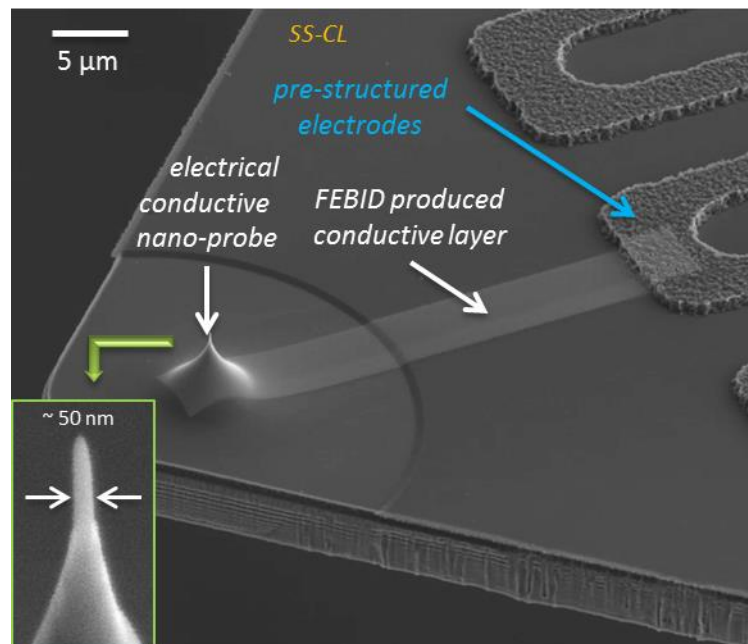

Figure 50: Overview illustration of the proof of concept for electrical conductive self-sensing-cantilevers.

The 3D writing capabilities of FEBID could be used to produce new, sharp tips since the coating process leads to a natural broadening of the AFM tip. However during this thesis an increase of the pillar diameters during the purification process could be observed. As J. Sattelkow could show in the frame of his dissertation thesis, this increase stems from the formation of a contamination layer during imaging processes after the purification. A procedure to overcome the formation of this contamination layer has been also developed. (see chapter 3.1.5.2.2).

The capability of the FEBID technique to modify SS-CL into conductive SS-CL could be confirmed. The electrical performance testing (see chapter 3.1.5.3) revealed that cantilevers produced in that way have the required functionality and the mechanical stability for conductive AFM applications. This means the successful proof of concept of the first conductive self-sensing cantilevers (see Figure 50).

The possibility to produce a conductive SS-CL with a high resolution, metallic tip is a unique selling point in the field of AFM. Based on the official ZFE cost calculations, the expenditure for the modification of one cantilever is 55 € [47]. This calculation doesn't include the sample preparations, the inward and the outward transfer. Though, the price is competitive in the market of AFM cantilevers.

3.2 Plasmonic Gold Nanostructures Produced via FEBID

3.2.1 Motivation

Plasmonic metal structures with a size in the nm-scale, allow light to be concentrated in areas smaller than the light's wavelength itself. Therefore, they are the subject of fundamental as well as of application oriented research [41].

Originally, nanostructured metals were used in the surface-enhanced Raman spectroscopy [51]. At the end of the last century, it was discovered that optical circuits made of metallic nanowires can be much smaller than dielectric (e.g., glass) waveguides [51], that metal films with nanoscale holes have an extraordinary high transmission in the optical wavelength area[52] and that metal thin films can be used as an optical lens[53]. These discoveries triggered an explosion of research interest and activities in the field of plasmonics and in the past 15 years many different applications have been developed. Plasmonic nano-structures opened the field for a new type of biosensors [54] and thermally assisted magnetic recording [51]. A thermal cancer treatment approach, which utilizes the normally unwanted side effect of heat development in plasmonic structures [55] and the usage for nanostructure growth[56] represent further practical applications. Plasmonic devices have been used as computer chips in the form of modulators incorporated into conventional electronics technology [57]. Also nanoscale lasers have been realized [58,59]. A very interesting idea promising a lot of technological progress is the usage of plasmonic lasers as ultrafast amplifiers, which could be used to build ultrafast logic circuits that perform a similar function as the ordinary transistor in semi-conductor industry but would be orders of magnitude faster[51,60].

Lithography techniques can be used to produce plasmonic nanoscale structures. In contrast to the use of lithography, using FEBID would allow to produce not only 2D but also 3D structures, which might enable very interesting new applications for plasmonics. An example for the possibilities of FEBID 3D structures can be seen in Figure 51. Besides that, FEBID technique allows processing on non-flat surfaces and provides big advantages concerning rapid layout change for prototyping.

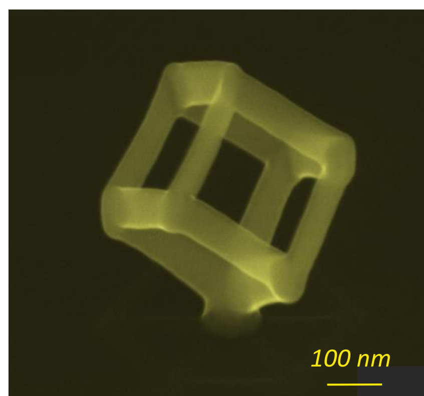

Figure 51: FEBID 3D cube made of Pt-C produced by R. Winkler[61]

To be able to use the precursor $Me_2Au(acac)$, which was newly introduced during this thesis at the FELMI-ZFE it had to be learned how to handle the general deposition. After deposition this precursor contains only approximately 8 at.% Au[21]. For plasmonic applications, pure Au is needed, which means that the purification approach already applied for the Pt precursor in chapter 3.1, had to be expanded for application with the Au precursor material.

After investigating the basic deposition behaviour and expanding the purification approach to the new precursor, the production of pure Au discs was optimized. The plasmonic behaviour of these e-beam lithography produced Au discs was then compared to prove that FEBID is suitable to produce plasmonic Au nano-structures.

Finally, it should be investigated if pure Au bi-ring structures with diameters in the 100 nm range can be produced via FEBID technique to be used for plasmonic examinations. This project was done in cooperation with the group of Prof. Michael Huth at the Goethe-University Frankfurt (Germany).

3.2.2 Au Precursor Deposition Behaviour

First, before the experiments to purify the Au based precursor deposits, the basic deposition behaviour and height growth for certain parameter sets had to be investigated. For the experiments including the Au precursor, the *custom GIS* (see chapter 2.1.2.7) was used.

First the general deposition rate of the new precursor was examined. Therefore, depositions with the parameters of 5keV primary beam energy, 1.6 nA beam current, 100 µs DT, 13 nm PoP, a patterning footprint of $2 \times 2\ \mu m^2$ and a varying amount of passes were produced. Figure 52 shows the deposition growth rate for this parameter set. Compared with the Pt deposition rate for the Pt precursor, for which the exact same deposition parameters, but a different GIS (*working GIS*) were used, the deposition rate is almost 8 times lower (see Figure 26 (b)).

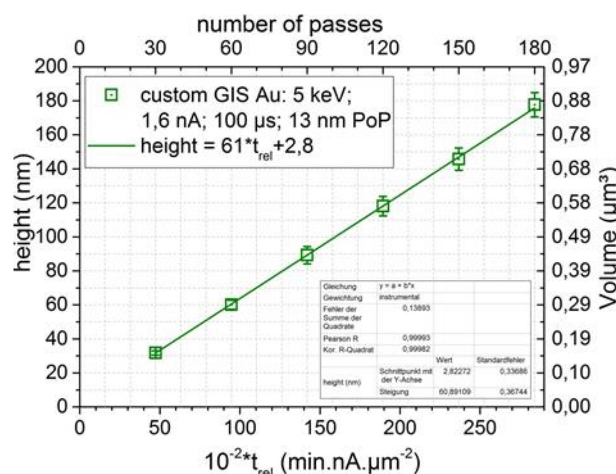

Figure 52: Deposition rate for the Au precursor with the according parameters. The y-axes show the height and the deposition volume of the pad.

According to the adsorption rate model (see equation (6)), there are several possible reasons including a combination of them for the dramatically lower deposition rate:

- Lower adsorption rate, either because of a lower sticking coefficient s or a lower precursor flux J
- Fast desorption because of a low average residence time τ
- Lower surface diffusion coefficient D

Table 3: Edge length and patterning footprint of the deposits concerning the investigation of the influence of the patterning size on the deposition.

Edge length (µm)	Footprint A (µm²)
0,5	0,25
1	1
2	4
4	16

When varying the patterning footprint of the depositions, an interesting effect was observed. Apart from varying the square patterning footprint and using 130 passes, which should lead to a deposition height of approximately 120 nm for the $2 \times 2\ \mu m^2$ pad, the same parameters were chosen for the deposition. Deposits with 4 different square patterning footprints (see Table 3), were produced.

As Figure 53 shows, increasing the deposition patterning footprint results in an increase of the deposition height, which is directly proportional to the relative volume growth rate. The deposition height seems to follow an exponential function, which should reach the maximum of around 180 nm for a patterning footprint of approximately 25 µm². This shows that the deposition regime is strongly MTL limited. By dissociating the precursor molecules with the electron beam, the adsorbed precursor density gets depleted. For larger square patterning footprints, there is more time to replenish the precursor, because – using otherwise the same parameters – the beam needs more time to reach the same patterning area again. This is the so called replenishment time of the 2nd x-axis in Figure 53, referring to the time which is available to replenish the precursor at this point after the depletion. However, since the deposition and depletion for 5 keV and 1.6 nA takes place in a larger area than $13 \times 13\ \mu m^2$ (the PoP value) due to proximity deposition (for more detail see [62]), also surrounding points of the raster got depleted. Subsequent points on the raster and points on close parallel lines of the serpentine pattern (see Figure 6 (a)) are already partly depleted during the same pass. The situation of the precursor replenishment is therefore more complex than the definition used in Figure 53, but it gives an approximate value. The same behaviour in dependence of the replenishment time was already observed in [62]. In Figure 53 is For the Au precursor and this deposition parameters, the square patterning footprint of 25 µm² at which the maximum relative volume growth rate is reached corresponds to a replenishment time of 15 s. This is quite long and since this behaviour couldn't be observed for Pt precursor depositions with the same parameters and deposit sizes, the replenishment mechanisms of adsorption and diffusion must be much larger for the Pt precursor.

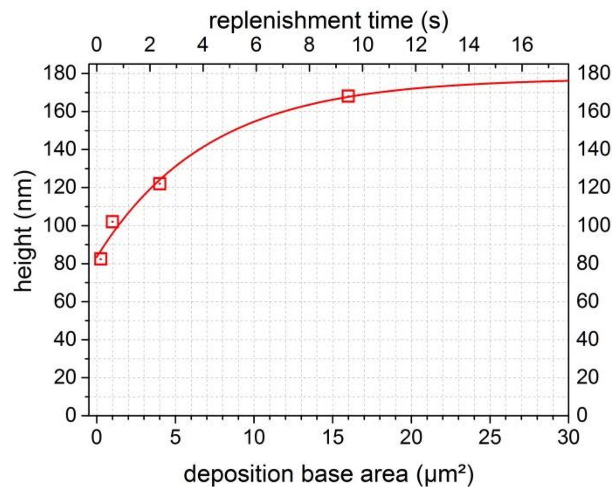

Figure 53: Heights of Au precursor depositions with different patterning footprints for 5 keV, 1.6 nA, 100 µs, 13 nm PoP and 13 passes. Since, for a larger patterning footprint, there is more time for replenishing the Au precursor gas, the deposits grew higher. The increase of the deposition height follows an exponential function, which should reach the maximum of around 180 nm for an area of 25 µm². The 2nd x-axis shows the so called replenishment time, which is defined here as the time needed for 1 pass. This means after this time, the beam gets to the same patterning point again and the precursor can be replenished during this time.

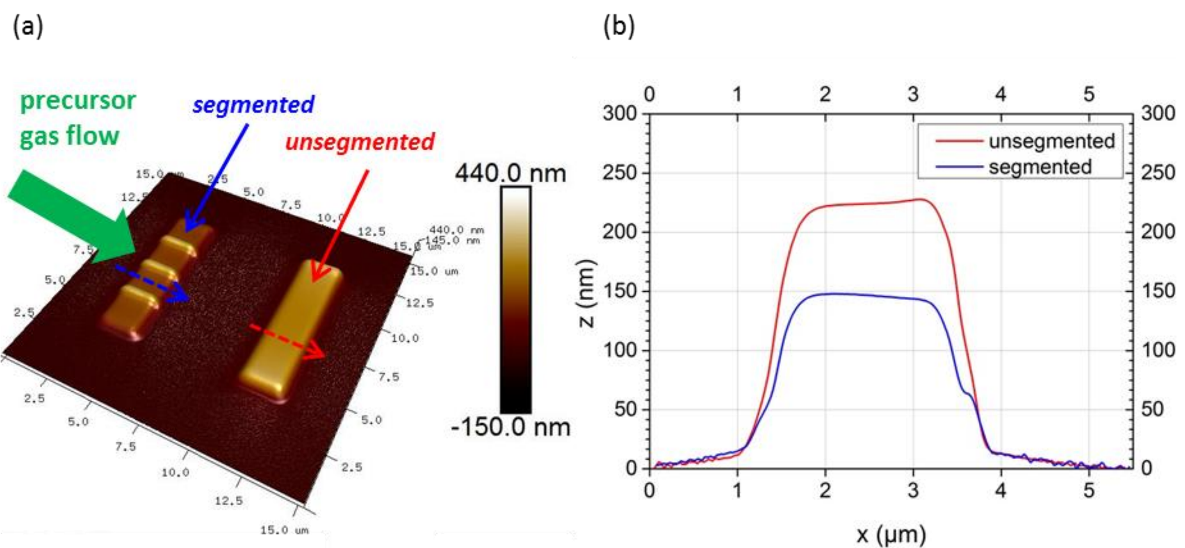

Figure 54: Another experiment demonstrating that the height difference for different patterning footprints originates from the available refreshment time and not from other influences (e.g. proximity effect). Two $8 \times 2\ \mu m^2$ pads were deposited with 2 different strategies: One pad was deposited unsegmented as a whole. The second pad was segmented in four $2 \times 2\ \mu m^2$ pads. All passes of each $2 \times 2\ \mu m^2$ pad were finished, before proceeding to the next one. (a) shows an AFM image of both pads. (b) shows the height profile across the equal coloured line in (a). As we can see the unsegmented pad is much higher than the segmented pad. The reason for that is the larger replenishment time for the $8 \times 2\ \mu m^2$ pad than for the $2 \times 2\ \mu m^2$ pad.

Another experiment was made to demonstrate that the height difference for different patterning footprints originated from the refreshment time given for each single patterning point and not from other influences (e.g. proximity effect). Apart from a patterning footprint of $8 \times 2\ \mu m^2$, the same parameters as before were used to fabricate two deposits with two different strategies: One pad was deposited un-segmented as a whole with the standard serpentine strategy. The second pad was segmented in four $2 \times 2\ \mu m^2$ pads, each again deposited with serpentine strategy. All passes of each $2 \times 2\ \mu m^2$ pad were finished, before proceeding to the next one. Figure 54 (a) shows an AFM image of both pads while, Figure 54 (b) shows the height profile across the equally coloured line in Figure 54 (a). As we can see the un-segmented pad is much higher than the segmented pad. The reason for that is the larger replenishment time for the $8 \times 2\ \mu m^2$ pad than for the $2 \times 2\ \mu m^2$ pad.

These results implicate that a lower beam current would be needed to receive depositions, whose height is uninfluenced by the patterning size in agreement with adsorption rate model (see equation (6); chapter 2.1.2.5). For the plasmonic Au structures (see chapter 3.2.5) and the bi-ring depositions (see chapter 3.2.6) much higher acceleration voltage and much lower current were chosen. However, since the growth rate was already quite low with this high electron beam current and the production of µm-scale pads with a height around 100 nm took already several minutes, these parameters were kept to produce the $2 \times 2\ \mu m^2$ pads for following purification experiments. For some applications deposits above 50 µm² and a target height around 100 nm are requested. However, the low deposition rate results in production times of several hours making it a little problematic for large scale coating applications. When using parameters, for which the final deposition height is not dependant from the patterning footprint, these production times are even going to increase significantly.

Also the patterning size dependency of the growth rate is a strong hint, that a short average residence time τ is not the main reason for the low growth rates of the Au precursor. In general the replenishment mechanisms for the Au precursor seem to be very slow. Possible ways to increase the growth rate could be (1) to lower the deposit temperature to increase the sticking coefficient s (and decrease the desorption rate τ) or (2) to increase the precursor flux from the GIS.

TEM investigations (see Figure 55 (a)) showed that the internal structure of as-deposited FEBID deposits is similar to those, which was observed for the Pt precursor [2,3]. In the TEM BF-image dark grains, which are made of crystalline Au, can be seen with a size between approximately 2 to 4 nm. These Au grains are uniformly embedded in a carbon matrix (bright parts between grains).

In Figure 55 (b) a free standing Au-C 3D nano-architecture can be seen, which proves that 3D structures are also possible with the Au precursor. The application of producing plasmonically active 3D structures is thereby especially interesting (see motivation in 3.2.1).

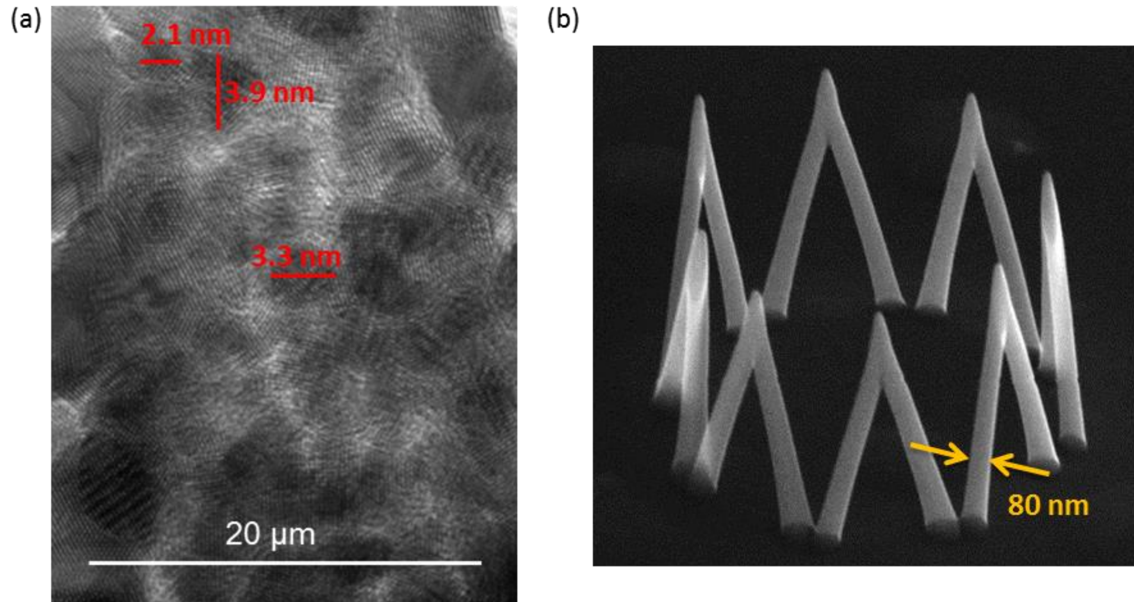

Figure 55: (a) TEM BF image of as-deposited Au-C nanopillar. Similar to Pt [2,3], the TEM investigation showed that the deposit before purification contains crystalline Au grains with a size of 2-4 nm (dark areas) embedded in a carbon matrix (bright part between grains). The pillar was produced via point deposition with 30 keV, 630 pA and 24 s deposition time. (b) ***GOLD CRONE****: SEM-image of the first free standing Au-C 3D nano-architecture proofing the 3D capability of the Au precursor.*

3.2.3 Au Precursor Purification Behaviour

As the inner structure of the nanopillar, which was fabricated from the Au precursor, revealed the inner structure of these deposits is quite similar to the inner structure of Pt deposits. This can be clearly seen if the inner structure of Au precursor deposits in Figure 55 (a) is compared with the inner structure for Pt precursor deposits in Figure 10 (a). Therefore it seemed promising to expand the same purification[2,3] approach already used for the Pt precursor, to the new Au based precursor (see chapter 2.4.1.1).

Au and Pt show quite similar behaviour concerning the peaks of the characteristic X-rays, which were used for the semi quantitative approach. The Pt-N peak lies at an energy of 313 eV and the Au-N peak is only a little bit shifted to 334 eV. The Pt-M peak has an energy of 2122 eV and again the Au-M peak is slightly shifted to 2206 eV. Because of these strong similarities, the carbon content and the progress of the purification can be monitored by using the same semi-quantitative approach as for the Pt precursor (see chapter 2.4.1.1). In Figure 56 there can be seen the EDX spectra of an as-deposited Au-C pad (black), of the same fully purified Au pad (red), of a sputtered Au layer to serve as a reference (green), and of the Si-wafer (3 nm of SiO_2 on Si), which was used as substrate (blue). In Figure 56 in the as-deposited EDXS spectra (black line), the peak around 250 eV contains, similar as for the Pt precursor deposits, not only the C-K peak but also the Au-N peak and the Si-L peak (from the substrate). To calculate the C/Au ratio, first the substrate spectrum is subtracted from the deposit spectrum for background correction. Then the value of the intensity integration from 170-410 eV (C-K and Au-N, for simplification denoted as C-peak) is divided by the value of the

intensity integration from 2000-2350 eV (denoted as Au peak) to receive the C/Au ratio. In Figure 56 the approximate integration ranges are indicated by the grey rectangles.

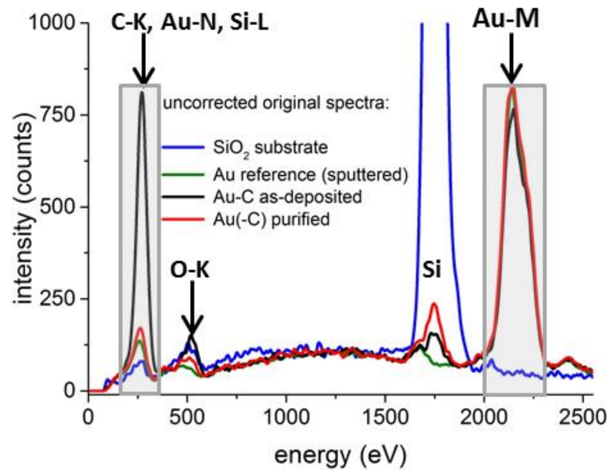

Figure 56: EDX spectra of an as-deposited Au-C deposit (black), the same fully purified Au deposit (red), a sputtered Au layer as a reference (green) and the SiO_2/Si substrate (blue). The as-deposited Au-C spectra has a high peak around 250 eV containing mainly the C-K line but also the Au-N line (originating from the deposit) and the Si-L line (originating from the substrate).

To test the principal applicability of the purification, 3 pads with a base area of $2 \times 2\ \mu m^2$ and heights of approximately 150 nm, 120 nm and 60 nm were produced, using the deposition parameters of chapter 3.2.2. For the purification a primary beam energy of 5 keV, a beam current in HV of 1.9 nA, 1 µs DT, 6 nm PoP, a H_2O pressure of 10 Pa and a purification field of $3.2 \times 3.2\ \mu m^2$ were used. In Figure 57 (a) the time evolution of the *in-situ* (during purification) C/Au peak ratio can be seen. The recording time of the *in-situ* EDX spectra was 120 s. The purification of all pads clearly shows a saturation behaviour, where the C/Au ratio doesn't decrease anymore, indicating that the purification process is finished. The 150 nm high pad was purified with a dose of 50 C/cm², the 120 nm high pad with 32 C/cm² and the 60 nm high pad with 26 C/cm². After the end of the purification, it was switched to the high vacuum mode and *ex-situ* EDX spectra in the centre of the purified pads were recorded with a field of view of $1 \times 1\ \mu m^2$. To compare these EDXS values with the EDX values of pure Au with an ideally low carbon value (stemming from the always present contamination effects in an electron microscope), the EDX spectrum of a sputtered sample was also recorded. The results of the *ex-situ* C/Au peak ratio can be seen in Figure 57 (b). The red circles mark the C/Au ratio of the purified pads having quite exactly the value of the sputtered Au sample. This strongly indicates that the purification was successful and that after the purification the deposits were pure and carbon free. Figure 57 (b) also shows the C/Au peak ratio of the as-deposited pads.

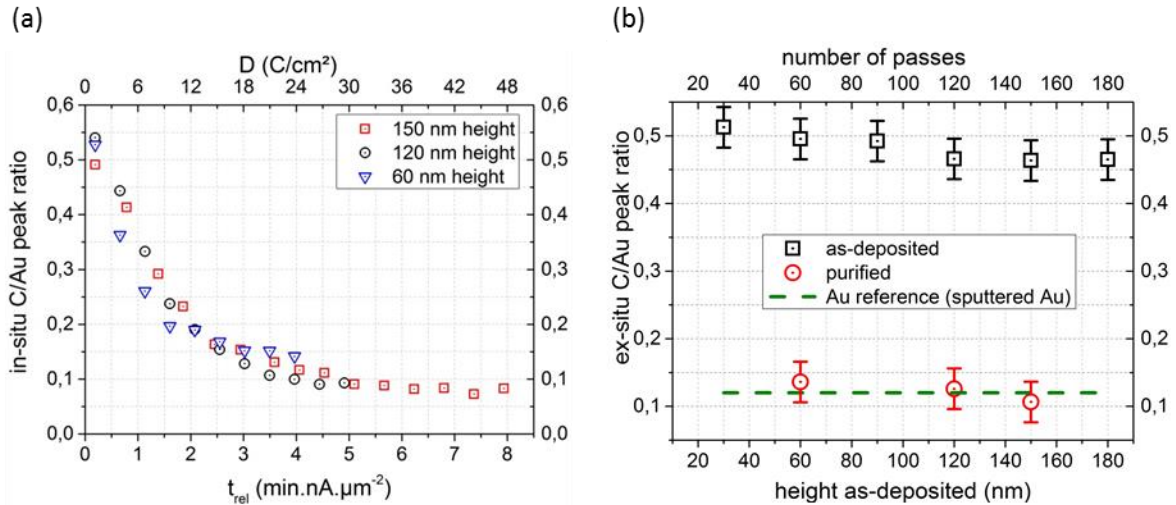

Figure 57: (a) Time evolution of the in-situ C/Au peak ratio for the purification with an electron beam current of 1.9 nA of 3 Au-C pads with different heights. The in-situ spectra were recorded for a period of 120 s. All 3 purification processes show clearly saturation behaviour indicating that the purification is finished. (b) Ex-situ C/Au peak ratio of the purified deposition pads with different heights. They have the same C/Au ratio as a sputtered, and thereby carbon free gold sample, indicating that the purification process produces carbon free depositions. Also the C/Au ratios of the as-deposited pads can be seen.

To examine the beam current influence on the purification, three $2 \times 2\ \mu m^2$ pads with a height of 120 nm were purified with differing purification currents of 0.54 nA, 1.90 nA and 8.40 nA. As can be seen in Figure 58, plotted over the relative purification time, which is an equivalent to the dose, the deposits purified with different currents showed the exact same relative time evolution of the C/Au peak ratio and reached the same saturation value. Therefore, the purification progress and the final purity depend only on the applied dose and there exists no minimal current threshold value.

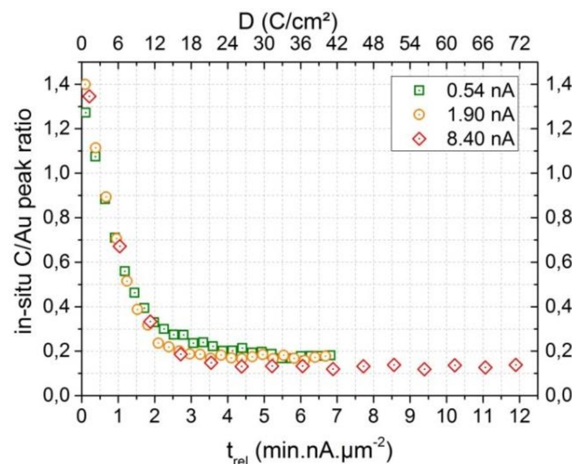

Figure 58: Time evolution of the in-situ C/Au peak ratio for the purification of 120nm high pads with 3 different currents. This shows that the purification progress and the final purity depend only on the applied dose and there exists no minimal current threshold value.

In order to investigate the volume loss and the morphological shape stability, AFM examinations were done on the pads prior and after the purification. The same 3 pads with heights of 150, 120 and 60 nm with the description of the deposition and the purification process above, were used. These examinations revealed a volume loss of (63±3) vol.% (see Figure 59 (a)).

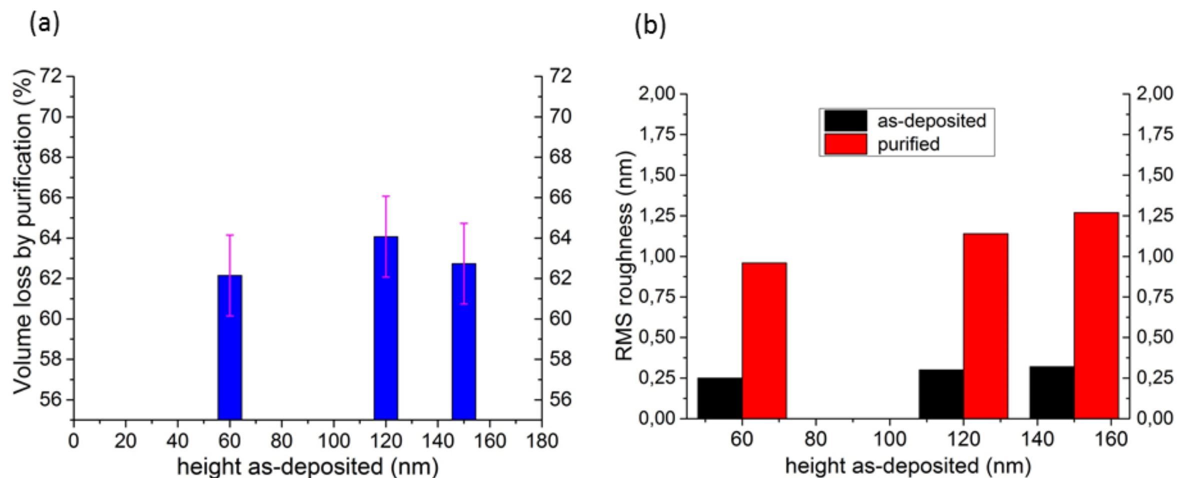

Figure 59: (a) Volume loss of the Au precursor pads of 3 different heights during the purification. (b) Comparison of the RMS surface roughness after deposition (black bars) and after purification (red bars). Because of crystal growth processes during purification[2,3], the RMS roughness increases. However, this has to be seen as a relative effect, because the absolute RMS roughness value of the purified pads is still excellent with a value of 1 nm.

Figure 60 (a) shows the AFM images of the 150, 120 and 60 nm high pads directly after the deposition. Figure 60 (b) shows the same pads after the purification. The surface of the purified pads showed no massive pores or cracks. The morphology remained very similar and the shape is fully maintained as can be seen in Figure 60 (c) which compares the normalized cross-sections before and after the purification.

In the centre of the pads ($1 \times 1\ \mu m^2$ area) the RMS surface roughness was measured. The exact result can be seen in Figure 59 (b). During purification the RMS surface roughness increased approximately by the factor 4. This increase stems from the massive volume loss and the expected grain growth of the Au crystals during the purification. The grain growth was not examined during this work in detail, but was already observed for the Pt precursor [2,3]. However, apart from this large increase in relative scale, it has to be kept in mind that the absolute values of the RMS roughness after purification are still very good with values of 1.00 - 1.25 nm. The smooth surface without pores or cracks is a major advantage of this purification approach compared to others.

A lateral shrinking of less than 3 rel.% was observed for the $2 \times 2\ \mu m^2$ pads. This lateral shrink corresponds to an absolute value of 60 nm. A similar behaviour was already observed for the Pt precursor [2,3]. The lateral shrink doesn't have much influence on the quality of purified µm-scale structures. However, at the edge of the 2 highest pads, the formation of cracks, which are indicated

by green arrows in Figure 60 (b), could be observed after the purification. The reason for these cracks is probably the lateral shrink during purification, which stresses the very thin deposition layers beside the actual pattern. These thin deposit layers originate from proximity deposition.

The purification of Au precursor deposits was successful and with 5 min.nA.µm^{-2} similar fast as for the Pt precursor. The purified deposits were carbon free (as suggested by EDXS) and showed a volume loss of (63±3) vol.%. The surface roughness increased slightly but is still good and the surface showed no pores or cracks. The lateral shrink was below 3 rel.%.

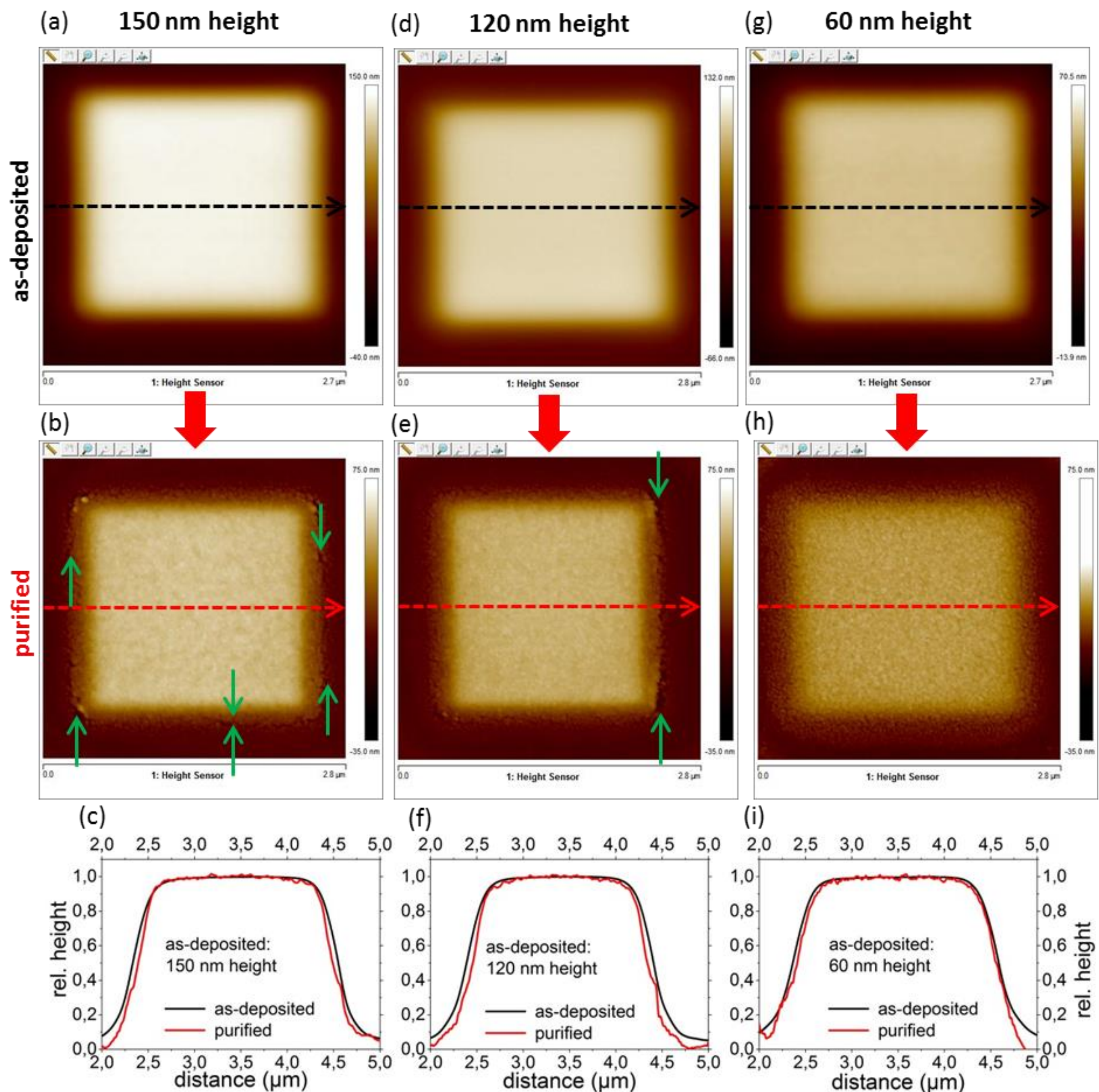

Figure 60: (a) AFM images of the 150, 120 and 60 nm high as-deposited Au-C pads and (b) the same pads after the purification. The green arrows in the AFM images of the purified pads indicate little cracks at the edge of the pads because of lateral shrinkage. (c) shows the normalized AFM cross-sections of the pads before and after purification and are indicated by a dashed line in the according colour in (a) or (b). They show that the lateral shrink during purification is below 3 rel.% ($\Delta d \cong 60\ nm$).

3.2.4 Post Purification Cleaning

After being able to produce pure Au FEBID deposits with fully maintained shape and good morphologies, the unwanted side effect of carbon contaminations, which appear during the purification process, had to be addressed. For example, during the electrical measurements of purified Pt deposits in chapter 3.1.4.1, although the purified Pt layers were carbon free, between the Pt layers carbon contaminations had formed (see Figure 36 (b) and Figure 37). Another typical form of contamination is an outer rim in the size of the purification frame around the structure, which can be seen in Figure 61 (a).

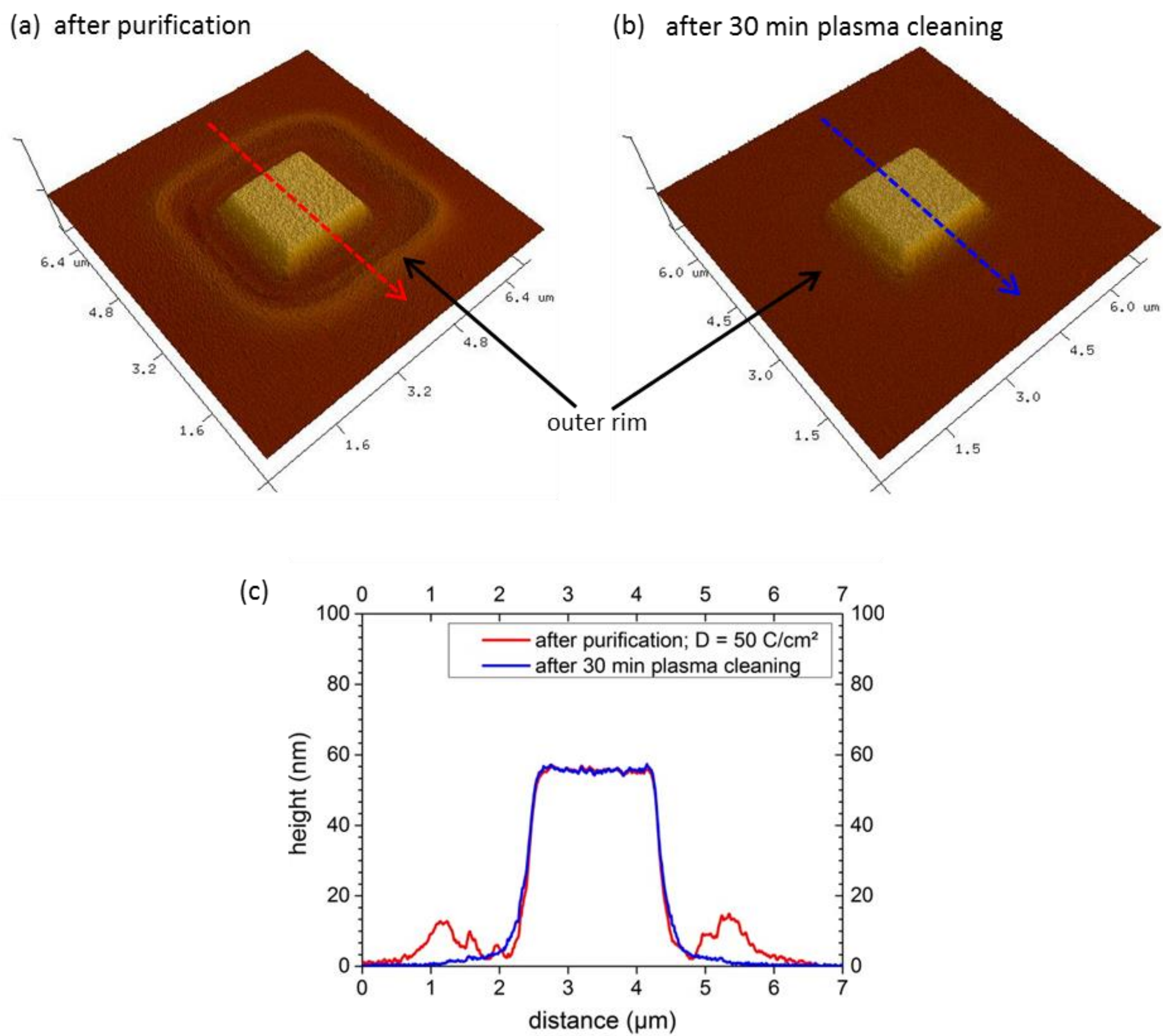

Figure 61: Graphics showing the effect of post purification cleaning. (a) AFM image, which shows the typical contamination after the purification process in form of an outer rim in the size of the purification frame. Representatively the 150 nm high pad from chapter 3.2.2 and 3.2.3 is displayed. (b) shows the same Pt pad after a 30 min O_2 plasma cleaning step. As can be seen, the so called outer rim was removed completely by the plasma cleaning step. (c) height cross section after the purification and after plasma cleaning along the red and blue line in the AFM images above. It can be seen that beside the removal of the outer rim, the topographical shape of the deposition didn't change.

These rims were already observed before[3]. Although, the structure itself is totally carbon free, these contaminations can have a negative influence for certain applications and therefore it's highly desirable to remove them.

In previous experiments, the O_2 plasma cleaning step showed little improvement concerning the contamination. During this thesis, it was discovered that the O_2 plasma cleaning step has to be applied for a relative long time to reach the desired outer rim removal. The removal is a non-linear process with low removal rates at the beginning followed by very fast removal after about 20 min. That explains why previous experiments with shorter plasma cleaning times showed no removal of the contaminations. The recommended plasma cleaning time for complete outer-rim removal is 30 min, for which the result can be seen in Figure 61 (b). The purified deposition itself isn't modified by the plasma cleaning. In Figure 61 (c) it can be seen that the topographical shape and height stay exactly the same. Also the surface roughness and the chemical composition are maintained.

The contamination itself seems to stem either from the deposition of the so called residual gas during purification in the chamber of the ESEM, or from contaminated samples. In any case, the accumulation of the contamination follows the same principles as the FEBID process. The molecules, which are responsible for the contamination rim are dissociated by the purification electron beam in volatile and non-volatile parts. The non-volatile parts form a kind of deposition, which represents the mentioned contamination. Because the purification beam depletes the surface density of adsorbate molecules inside the purification frame, a concentration gradient of these adsorbed molecules is created between the inside and the outside of the purification frame. As a result the molecules are supplied via diffusion processes from outside the frame.

This explains very well the formation of the outer rim. When the purification process is started, the adsorbate molecules responsible for the contamination get quickly depleted inside the scan frame and the resupply diffusion from outside the scan frame, where no deposition takes place, starts. Because of the high current, all the molecules get already dissociated and deposited before they are able to reach the central area of the purification frame and therefore, the outer rim forms at the edge of the purification frame as can be seen in Figure 61 (a). In cases where the purification frame is significantly larger than the $3.2 \times 3.2\ \mu m^2$ used here, the beam needs more time per purification frame scan and therefore, there is more time for the molecules to diffuse also to the centre of the scan frame. When larger purification frames are used, the contamination is deposited like a layer across the whole purification frame. Because of this, in chapter 3.1.4.1 contamination layers above the purified deposit were observed. The thickness of the contamination layer depends on the applied purification time and dose. For optimal parameters, they are reduced drastically (see chapter 3.1.4 and Figure 36 (a)).

The theory of the diffusion was confirmed with an experiment where deep FIB cuts, as can be seen in Figure 62, were made around the pad. These FIB cuts should form a morphological barrier to the diffusion process of the adsorbent molecules and prevent that a purification rim like in Figure 61 is formed. The pad was purified with the same parameters as the pads from chapter 3.2.3, so a purification rim should have formed. However, as the AFM image of the fully purified pad in Figure 62 shows, no outer rim appears around the deposit.

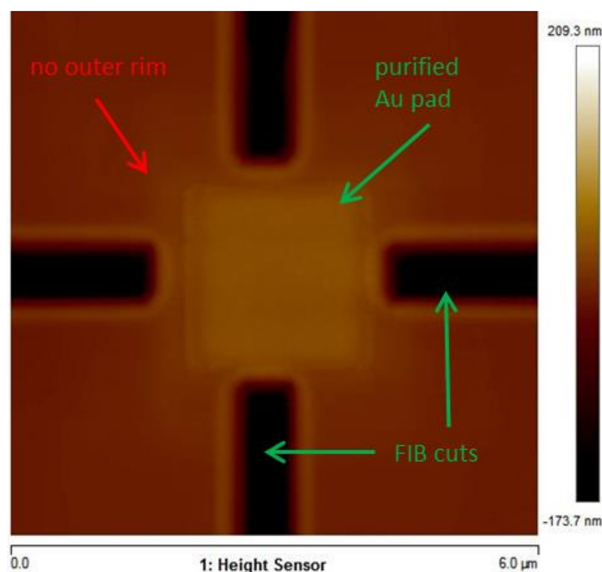

Figure 62: AFM image of a fully purified Au precursor pad, where FIB cuts in a cross form were made around the pad for better alignment during the purification process (D = 50 C/cm²). The as-deposited pad was 120 nm high and the same purification parameters as in chapter 3.2.3 were used. Due to the physical barrier the FIB cuts represent towards the diffusion of the contamination molecules, no contamination rim (outer rim) was formed during the purification.

3.2.5 Plasmonic Au Discs

After being able to produce pure Au FEBID deposits (see chapter 3.2.2 and 3.2.3) and being able to remove also the outer purification rim thanks to a newly developed post purification cleaning strategy (see chapter 3.2.4), the next step was to produce plasmonic structures to demonstrate that FEBID plasmonics is possible. In order to reach this important milestone, gold discs in different diameters were produced and their production parameters optimized. The plasmonic activity of these discs should then be compared with those of discs with the same dimensions but produced with the conventional fabrication technique of electron beam lithography (**EBL**). After this proof of concept, the path would be open to use FEBID's unique fabrication capabilities for the production of totally new plasmonic structures not possible with other fabrication techniques (see chapter 3.2.1).

3.2.5.1 Production of the Discs

For the plasmonic experiments with FEBID produced Au discs, the aim was to fabricate pure discs with 6 different diameters of 150, 200, 250, 300, 350, and 400 nm on a 15 nm thick Si_3N_4 TEM grid (Ted Pella; Prod-Nr: 21569-10), which was already used for the EBL produced discs. Same as the EBL discs, the FEBID produced discs should have an approximate height of 30 nm. The 15 nm thick Si_3N_4 substrate layer of the TEM grid is embedded in a thicker frame structure of the grid, which grants mechanical stability. In Figure 63 (a) light microscope image of this TEM Grid can be seen. The Si_3N_4 window forms a topographical cavity of 200-300 nm depth with relation to the surface of the surrounding frame structure. This is important, since this cavity seems to improve the replenishment mechanism and increase the surface density of the adsorbed precursor molecules leading to different deposition behaviour in comparison with totally flat substrates. This could be clearly observed in the experiments concerning the bi-ring (chapter 3.2.6.2). Beneath the under surface of

the TEM window, there is about 500 µm of chamber vacuum (200 µm broadness of the TEM grid holder adds up with 300 µm because of a cavity in the holder of the TEM grid) before the Cu body of the TEM grid holder follows (see Figure 63 (b)).

Since higher primary beam energy results in better resolution[14], the highest possible value of 30 keV was chosen for the deposition. This higher primary beam energy reduces the spot size of the electron beam and the proximity deposition compared to lower beam primary beam energies. An electron beam current of 150 pA was chosen as a compromise between growth speed and broadening of the electron beam for higher currents.

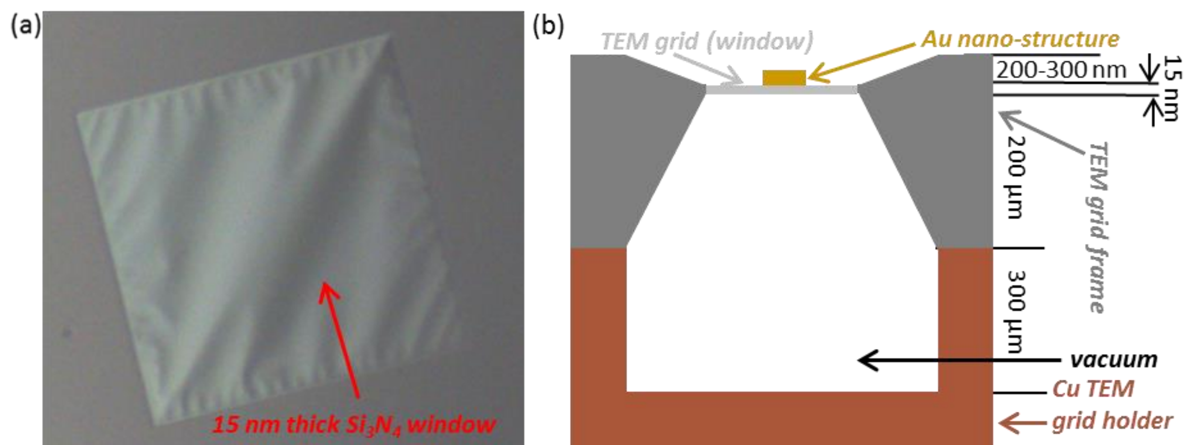

Figure 63: (a) Light microscope image of the 15 nm thick Si_3N_4 window embedded in the frame structure of the TEM grid. It can be seen that the surface of the TEM window is topographically lower than the surface of the frame structure and forms a cavity. (b) Schematic illustration of the TEM Grid position during deposition not showing the true proportions.

To examine the growth rate and the optimal parameters for the disc fabrication, $300 \times 300\ nm^2$ pads were produced on a conventional Si wafer and on a TEM grid with 30 keV, 150 pA, varying DT, PoP and t_{rel} (relative exposure time). The deposition height on the Si wafer seemed to be mostly independent for a DT variation between 1 and 10 ms, which can be seen in Figure 64 (a) by the data points in the different shades of green. Also changing the PoP didn't change the growth rate as can be seen by the blue data points in Figure 64 (a). This behaviour is the expected one for a strong MTL deposition regime. If the DT is large (in the area of ms), in a first, only small fraction of the DT most of the initial precursor coverage is depleted. During the rest of the DT the growth rate depends on the number of precursor molecules supplied by the replenishment mechanisms. However, for the depositions on the TEM grid (which forms a cavity), a bigger DT leads to a larger height growth rate if the same t_{rel} is applied, as can be seen in Figure 64 (a) by the light red and dark red data points. The reason why different DT leads to different heights for the cavity of the TEM grid as substrate, but not for the Si wafer, isn't yet understood and further examinations have to be done, since only one single experiment of this kind was carried out.

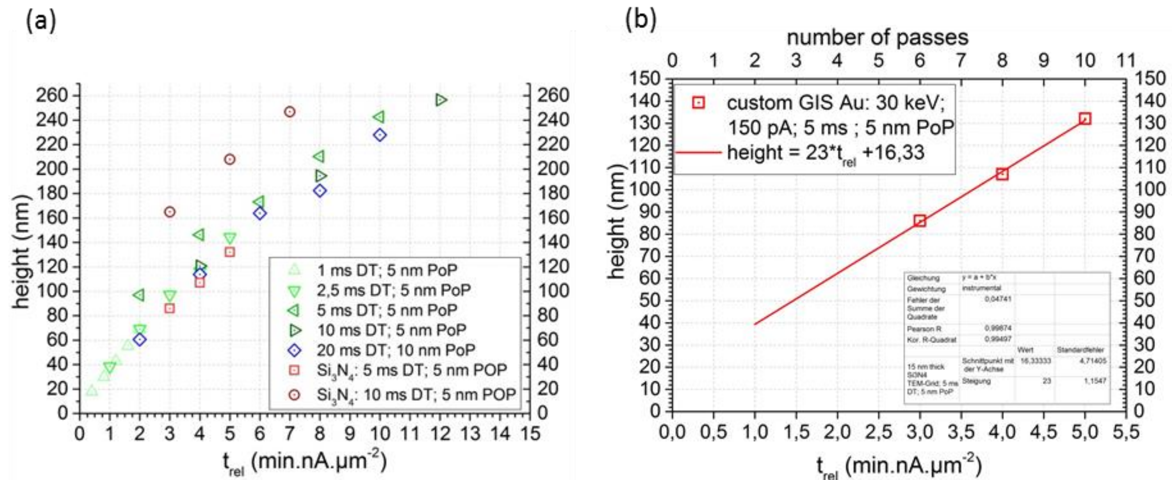

Figure 64: (a) Deposition height of the Au precursor for square pads with 300 nm edge length in dependency of t_{rel} (relative exposure time). A primary beam energy of 30 keV and a beam current 150 pA were used for deposition. The DT, the PoP and the number of passes were varied. The depositions of the data points in different shades of green and blue were done on a conventional Si Wafer substrate, while the depositions of the data points in the shades of red were done on the 15 nm thick Si_3N_4 TEM grid. As can be seen in the green and blue data points, different DT and PoP values only have a relative small influence on the deposition height on the flat Si wafer. The deposition height depends approximately linearly on t_{rel}. Interestingly, the deposition heights on the TEM grid are much larger for the 10 ms DT than for 5 ms DT. The reason for that is not clear, and further experiments have to be carried out, since only one of this kind was done in the frame of this thesis. (b) Au precursor growth rate for 5 ms DT and 5 nm PoP, which were the chosen parameters for the disc production on the TEM grid. Via the linear fit, it can be determined that for a target height of 62 nm, 4 passes had to be chosen.

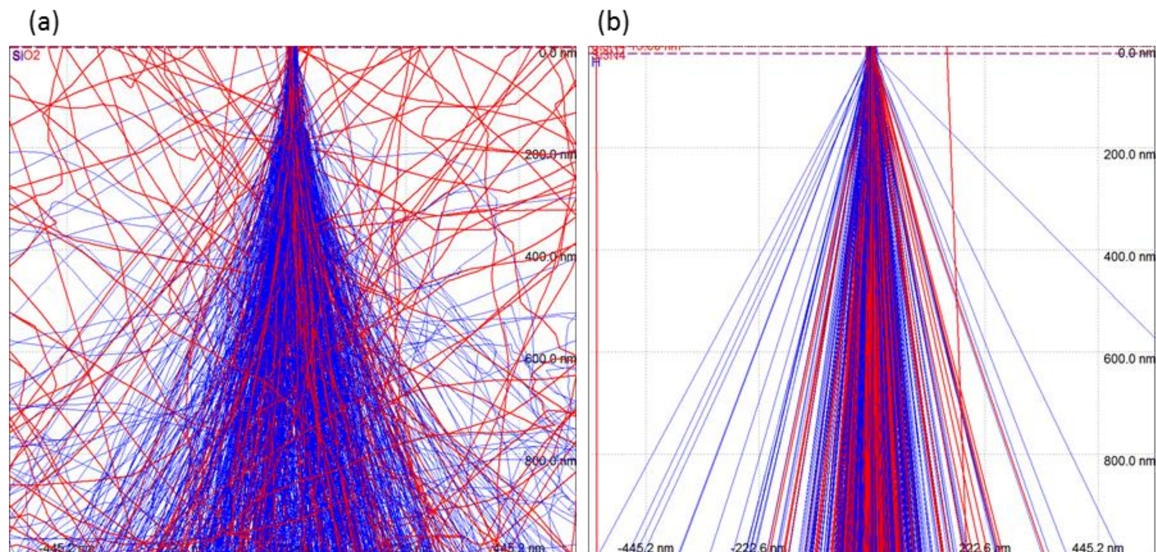

Figure 65: Monte-Carlo simulations of the electron path with Casino 2.48 [48] for a primary beam energy of 30 keV. (a) shows the simulation for a conventional Si wafer with 100 trajectories displayed (3 nm of SiO_2 above pure Si). (b) displays the simulation for a 15 nm thick Si_3N_4 TEM grid, where beneath the TEM grid there is 500 µm vacuum before the Cu surface of the TEM-Grid holder follows (5000 trajectories). The red trajectories are BSE.

In Figure 65 (a) the Monte-Carlo electron path simulation can be seen for a conventional Si wafer and can be compared with the path simulation for a 15 nm thick Si_3N_4 TEM grid (Figure 65 (b)). The TEM-grid positioned in the holder has 500 µm of vacuum between it's under surface and the Cu surface of the TEM grid holder. For the Si-wafer substrate (Figure 65 (a)), there are much more backscattered electrons in relative proximity to the location of the beam impingement than for the TEM-grid substrate (Figure 65 (b)).

For the production of the discs on the TEM grid, 5 ms DT and 5 nm PoP were chosen, for which the height growth rate can be seen in detail in Figure 64 (b). This allowed good height tunability. To reach the target height of 62 nm, 4 passes were chosen (note the number of passes on the 2nd x-axes in Figure 64 (b)).

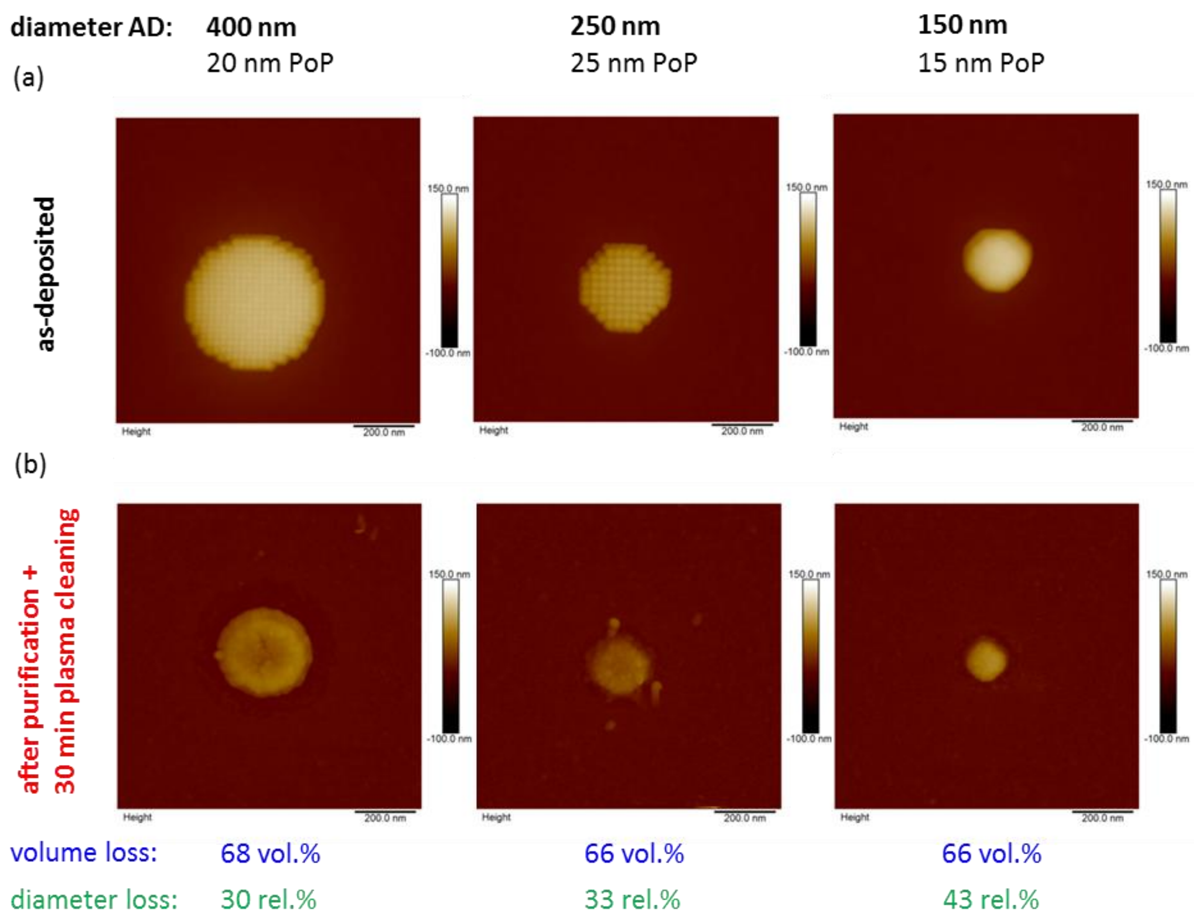

Figure 66: AFM height images of Au precursor discs on a Si wafer showing them in (a) the as-deposited state and (b) the fully purified one including 30 min O_2 plasma cleaning after the purification. The discs have an as-deposited diameter of 400, 250 and 150 nm and the PoP during deposition varied between 15 and 25 nm. It's important to note that while the volume loss was as expected between 66 and 68 vol.%, the lateral shrink is with 30-43 rel.% very large compared to the one of a 2 µm pad.

Experiments examining the deposition and purification of Au precursor discs on a Si wafer revealed interesting aspects. The discs were deposited with a larger PoP (between 15 and 25 nm), a DT of 20 ms and 16 passes. This resulted in slightly different heights in the range of 80-110 nm. The as-deposited discs can be seen in Figure 66 (a).While for the disc with 250 µm diameter and 25 nm PoP, the single patterning points can be distinguished in the AFM image, this is not the case anymore for discs with 150 µm diameter and 15 nm PoP. Still, even for a PoP of 15 nm, the edge of the disc is not circle like yet. Therefore a much smaller PoP of 5 nm was finally chosen.

Figure 66 (b) shows the AFM images of the fully purified discs after a 30 min O_2 plasma cleaning step. The discs were purified using 5 keV primary beam energy, 2 nA beam current, 1 µs DT, 6 nm PoP, 10 Pa H_2O pressure, a purification field size of $2 \times 2\ \mu m^2$ and a dose of 53 C/cm². Each disc was individually purified but due to the large purification area compared to the size of the discs, the EDXS background signal from the substrate was too strong for significant *in-situ* EDXS data. While the volume loss for the fully purified discs was within the expected range (66-68 vol.%), the lateral shrink differed severely from those of µm-scale pads (see chapter 3.2.3). The relative lateral shrink for the discs was 30-43 rel.% and increases if the disc diameter is decreased. The reason for is probably to find in the relation of the cohesive force between deposit and substrate and the internal forces, which occur due to the shrinking process. In the fully purified and plasma cleaned image of the disc with an original diameter of 250 nm, there can be seen particles directly beside the pad. The reason for that is that the GEA plasma cleaner (see chapter 2.3) used for this sample, is also used for metal sputtering. This results in residues of the sputtering process being in the plasma cleaning chamber and these residues can be unwillingly transferred on the sample during plasma cleaning. For discs which were plasmonically examined, the plasma cleaner for TEM samples was used, which doesn't have this problem.

For the production of the Au-C discs, the parameters mentioned above were used for the deposition. The discs of all 6 different sizes were deposited in a triangular pattern having at least 2 µm distance between two discs. This triangular pattern can be seen in Figure 67 (a) as a HAADF image of the as-deposited discs. In the HAADF images, which give a strong Z contrast, light elements are dark while heavy elements are bright. The TEM, which was used for all examinations of plasmonic Au structures including all the HAADF images in Figure 67 was a TF-20. The TEM investigations and the plasmonic examinations were done together with F. Schmidt. Figure 67 (b) shows representatively the as-deposited disc with a diameter of 350 µm. In the proximity of the disc, there can be seen bright structures on the otherwise dark Si_3N_4 substrate. These are probably proximity depositions of backscattered electrons (see Figure 65 (b)). BSE hit the Cu surface of the TEM grid holder after flying through the only 15 nm thick Si_3N_4 and 500 µm of chamber vacuum to the Cu surface of the TEM grid holder. There they get backscattered and fly back to the TEM-grid surface. Due to the large flight route in vacuum, they get spread across a large area. This can be seen by the relative few BSE exiting the TEM grid close to the location of the primary beam impingement in Figure 65 (b) compared to the usual situation with a Si-wafer substrate (Figure 65 (a)).

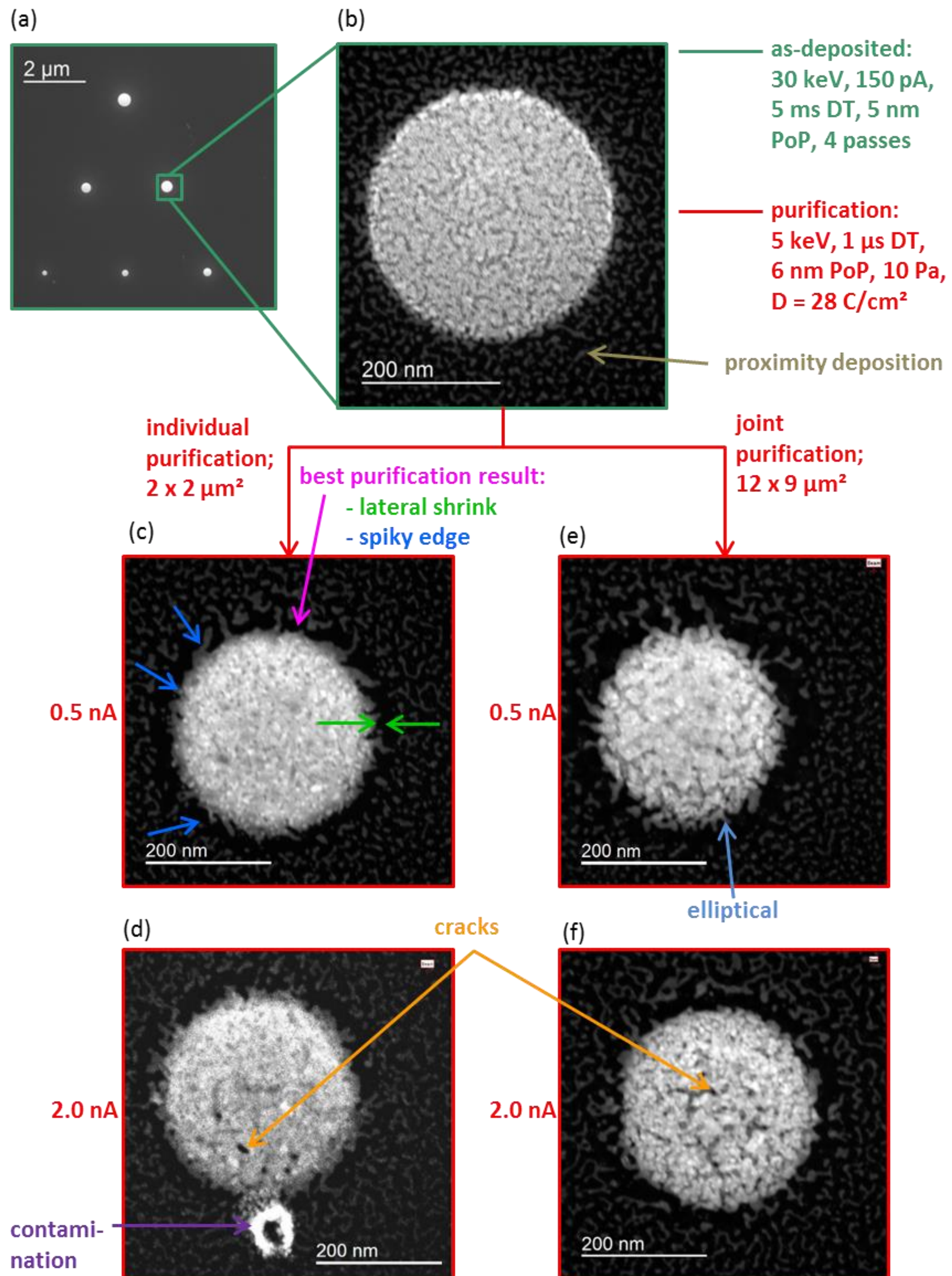

Figure 67: Schematic representation showing HAADF images of as-deposited discs (green frame) and fully purified discs (red frame) for which different purification parameters were used. (a) Overview image of the general arrangement of the 6 different sized discs. (b) as-deposited disc with 350 µm diameter. (c) and (d) show the same size fully purified discs, which were individually purified in a $2 \times 2\ \mu m^2$ *scan frame with a current of either (c) 0.5 nA and (d) 2.0 nA. (e) and (f) show the fully purified discs for the purification strategy where all the discs seen in (a) where jointly purified in a* $12 \times 9\ \mu m^2$ *scan frame with (e) 0.5 nA or (f) 2.0 nA. Individual purification with 0.5 nA (c) leads clearly to the best result.*

For the purification of the discs 4 different strategies were chosen. The constant purification parameters were always 5 keV primary beam energy, 1 µs DT, 6 nm PoP, 10 Pa H_2O pressure and a dose of 28 C/cm². This dose is sufficient for the purification as it can be concluded by the previous experience in chapter 3.2.3 and the time development of the C/Au ratio during the purification (Figure 68 (a)). Using a $2 \times 2\ \mu m^2$ purification scan frame, the 2 sets of discs of all different sizes were purified each of them individually using either 0.5 nA (Figure 67 (c)) or 2 nA (Figure 67 (d)) purification beam current. Also for 2 sets of discs, the hole set was purified simultaneously using a $12 \times 9\ \mu m^2$ scan frame and thereby using again either 0.5 nA (Figure 67 (e)) or 2 nA (Figure 67 (f)) beam current. After the purification the discs were cleaned in the Fischione plasma cleaner for TEM samples

The quality of the 350 µm discs, which were representative for the other disc sizes, was quite different and can be seen in Figure 67 (c)-(f) in HAADF images. Both, the individual and the joint purification process using 2 nA resulted in discs, which showed cracks inside the discs with no or only very few Au there, which can be seen in Figure 67 (d) and (f). Figure 67 (e) also shows a contamination, whose origin is not clear. The joint purification with 0.5 nA current (Figure 67 (e)) led to discs which had mostly not a circular shape anymore but an elliptical. The appearance is granular and the grain size appears to be relatively large compared to the other discs.

The best result was clearly achieved by using 0.5 nA and the individual purification approach for each disc, as can be seen in Figure 67 (c). Therefore, these were the discs, which were used for the plasmonic examinations in chapter 3.2.5.2. The discs show a nanogranular appearance and seemingly smaller grain size than discs with the joint purification approach and the same beam current (Figure 67 (e)). The darker zones in the HAADF image are nanovoids due to the granular inner structure. However, if the appearance of the discs with these parameters is compared to the discs purified with a beam current of 2.0 nA (Figure 67 (d) and (f)), they are much more homogenous and don't contain the big cracks. The discs also showed a relatively large lateral shrink, like observed before for the discs on a Si wafer. The shrink is marked by the green arrows in Figure 67 (c). Also the edge of the disc shows a spiky appearance, indicated by the blue arrows in Figure 67 (c). The shrink and the spiky edges stem from the dynamics and the volume loss during the purification.

The time evolution of the *in-situ* C/Au peak ratio for the individual purification of all 6 discs with 0.5 nA can be seen in Figure 68 (a). Gaining these data was only possible because the EDX signal from the substrate was massively reduced because of the thinness of the TEM-grid. The purification curves of all discs show clearly a saturation behaviour which indicates that they were fully purified. The time evolution shows the expected saturation trend but the data are relatively inaccurate though to the small disc sizes.

In Figure 68 (b) the EELS spectra of an as-deposited disk (green) and the same, fully purified disc (red), which were gained by a TEM examination, can be seen. While the C_K peak was high and very well visible in the spectrum of the as-deposited disc, for the fully purified disc it almost disappeared completely and only a very small shoulder is still visible there. If it is taken into account, that minimal carbon contaminations from the laboratory environment are present on basically every sample, this demonstrated in a very strong way that the discs were carbon free. While, in the as-deposited spectra the N_K peak is not visible because of the relative high absolute thickness of 60 nm, in the

spectrum of the purified disc, it is slightly visible, because the absolute thickness is approximately halved.

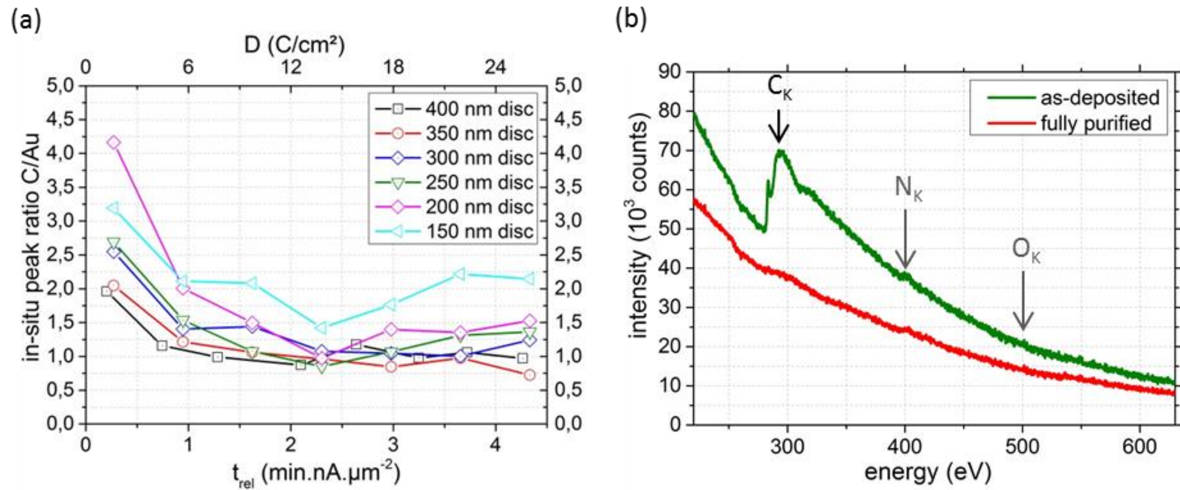

Figure 68: (a) time development of the in-situ C/Au peak ratio for the individually purified discs with a purification current of 0.5 nA on a 15 nm thick TEM grid. All the discs show clearly saturation behaviour. (b) EEL spectra of an as-deposited disc (green) and the same disc fully purified (red) gained via TEM. While, the as-deposited disc shows a clear carbon peak, on the fully purified disc the carbon peak is almost completely gone.

As mentioned above, the discs on the Si wafer and the TEM grid, showed a much larger relative lateral shrink, than observed for $2 \times 2\ \mu m^2$ large pads (see chapter 3.2.3). To investigate the behaviour of the lateral shrink in detail, in Figure 69 (a) the relative lateral shrink and in Figure 69 (b) the absolute lateral shrink, both in dependence of the deposit size, can be seen. The term "deposit size" means the edge length for square deposits and the diameter for discs. Blue data points show the shrinkage for deposits on a Si wafer and red data points for deposits on the Si_3N_4 TEM grid. The blue data squares in Figure 69 show the relative shrinkage of a typical $2 \times 2\ \mu m^2$ pad (edge length 2000 nm) and the discs from Figure 66 with 400, 250 and 150 nm as-deposited diameter. The red circles in Figure 69 show the relative lateral shrink of the discs on the TEM grid with 400, 350, 300, 250, 200 and 150 nm as-deposited diameters, and which were purified with 0.5 nA and individual purification strategy. It can be seen in Figure 69 (a), that the relative lateral shrink for all deposits on the Si wafer (blue squares) and for the 4 largest discs on the Si_3N_4 TEM grid (red circles), follow a logarithmic behaviour. However, the 2 smallest discs on the TEM grid with 200 and 150 nm diameters don't follow this trend. The difference of the shrinking concerning the two substrates stems probably from different interfacial energies between the deposit and the substrate. Looking at the absolute lateral shrink in Figure 69 (b), it can be seen, that the largest value for the Si wafer substrate is measured for the disc with 400 nm diameter. This suggests the following behaviour: The interface force between the deposit and the substrate is proportional to the size of the footprint of the deposit. For large deposits (2000 nm edge length) the interface force is large enough to keep the deposit sticking to the substrate, although the lateral strain, inflicted by the purification and the

resulting volume loss, tries to decrease the footprint by a larger amount than observed for the $2 \times 2\ \mu m^2$ pads. When the footprint of the deposit becomes smaller, there is a limit, where the interface force isn't able to withstand the lateral strain anymore, and the deposit breaks loose from the substrate eliminating the resistance against the lateral strain. Therefore at this limit the absolute lateral shrinkage reaches its maximum value. When the footprint is further reduced, the absolute lateral shrinkage is linked to the absolute volume shrink and therefore reduces again.

Independently from the shrinking behaviour, it has to be mentioned, that the TEM grid is so thin that after deposition and purification the surface is not flat anymore, but shows topographical features, similar like a tensioned plastic foil on which at some points weight forces are applied.

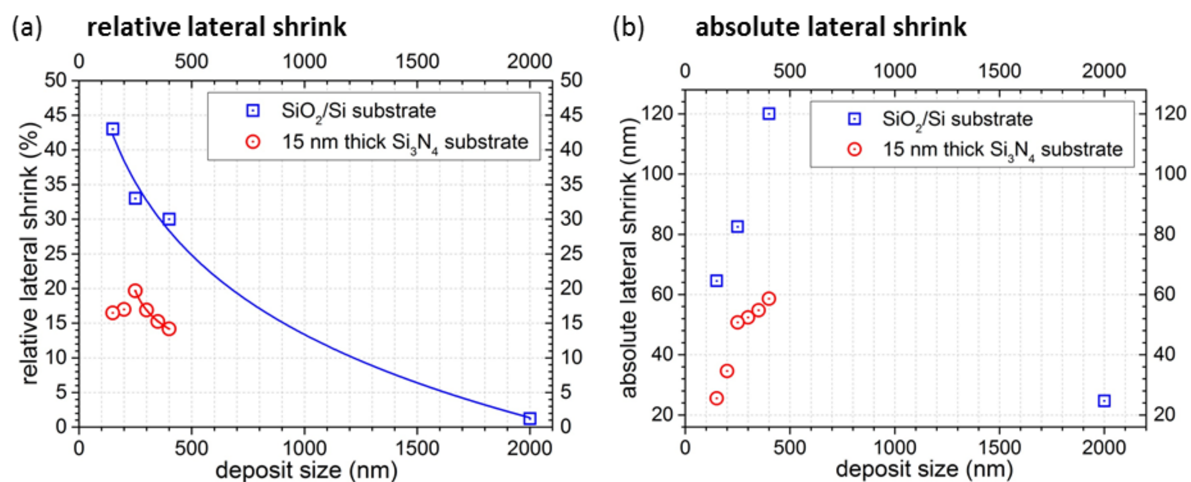

Figure 69: (a) relative lateral shrink and (b) absolute lateral shrink of Au precursor deposits during purification in dependence of their size with either a Si wafer as substrate (blue squares) or a Si_3N_4 TEM grid (red circles). The lateral shrinking behaviour is determined (1) by the interfacial force between deposit and substrate and (2) by the lateral strain which is inflicted by the purification.

3.2.5.2 Plasmonic Properties

To study the plasmonic behaviour, electron energy loss spectroscopy (**EELS**) was used. These examinations were done in a transmission electron microscope (TEM) of the type FEI Tecnai F20. To check the effect of purification, the plasmonic behaviour of purified discs were compared with that of as-deposited discs. Also the plasmonic behaviour of purified discs were compared with those of pure gold discs fabricated via electron beam lithography (**EBL**). This data of the EBL discs were gained by F. Schmidt in the course of his research before this thesis.

Figure 70 demonstrates by showing EELS-maps that fully purified discs show plasmonic behaviour while as-deposited discs show no plasmonic behaviour at all. The energy of the EELS-maps ranks from 1 eV to 2 eV with a step width of 0.2 eV. In Figure 70 (a), showing the fully purified disc, from 1.0 eV to 1.6 eV, plasmonic excitation can be seen along the edge and represent the so called edge modes. At energies of 1.8 eV and 2.0 eV plasmonic excitations can be seen in the centre of the discs. This is the so called breathing mode. Figure 70 (b) shows the EEL-maps of the as-deposited disc,

where no plasmonic excitations can be seen and the EELS-maps show only noise on the discs. The deconvoluted EELS-maps of the raw data from Figure 70 (a) can be found in Figure 71 (a).

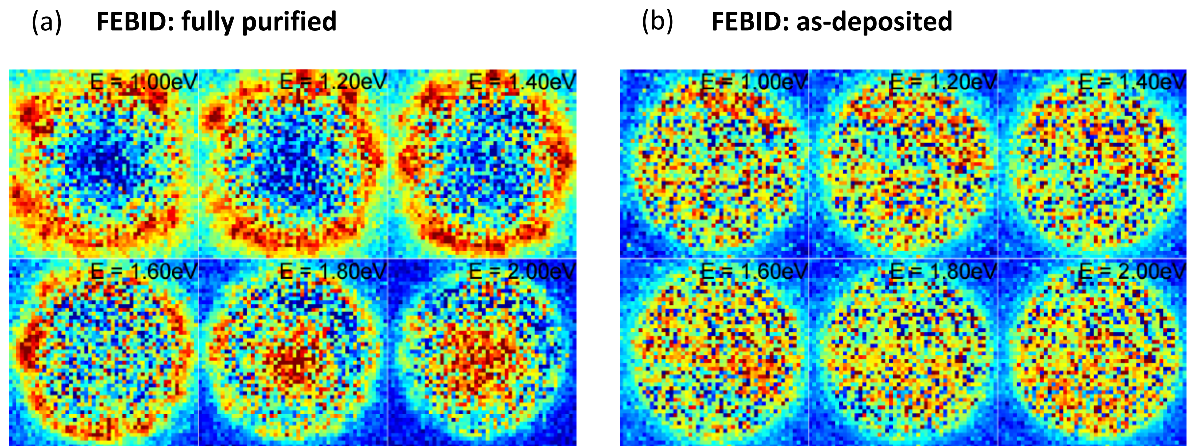

Figure 70: EEL-maps (raw data) of a two FEBID discs with an as-deposited diameter of 400 nm. While the fully purified disc in (a) shows clearly plasmonic behaviour (diameter after purification ≈350 nm), the as-deposited disc in (b) shows no plasmonic behaviour at all.

Figure 71 compares the deconvoluted EELS-map of the fully purified disc produced via FEBID (Figure 71 (a)) with the EEL-maps of a disc in the same size and height, which was fabricated via EBL (Figure 71 (b)). The comparison demonstrates that FEBID fabricated discs show basically the same plasmonic behaviour as EBL fabricated discs. However, taking a closer look some differences can be seen. For example for for the FEBID produced disc the breathing mode appears at 1.80 eV, while for EBL disc at the same energy, it can’t be seen yet. Differences at the disc border stem from the non-perfect edges of the FEBID produced disc (Figure 67 (c)).

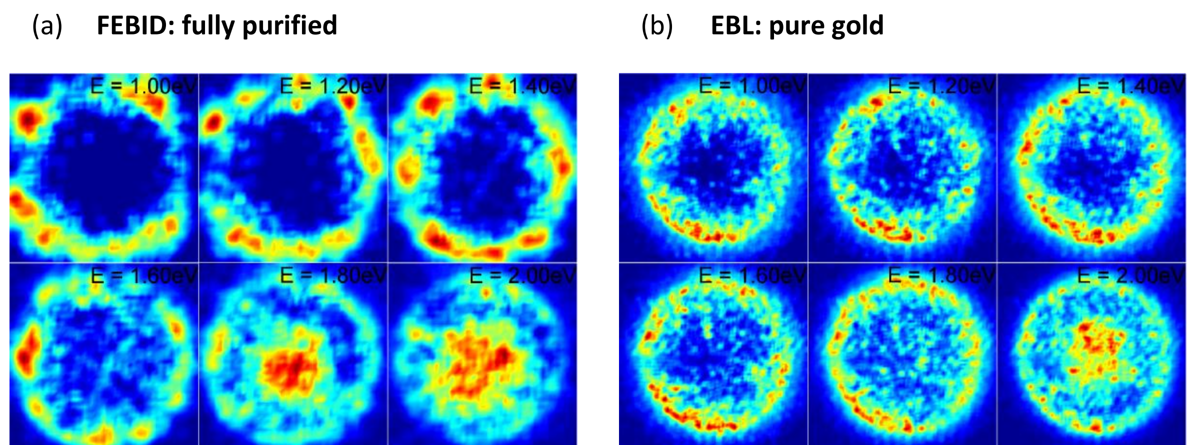

Figure 71: (a) Deconvoluted EEL-maps of the fully purified FEBID disc from Figure 70 (a). (b) Deconvoluted EEL-maps of a pure Au disc of the same size produced via EBL.

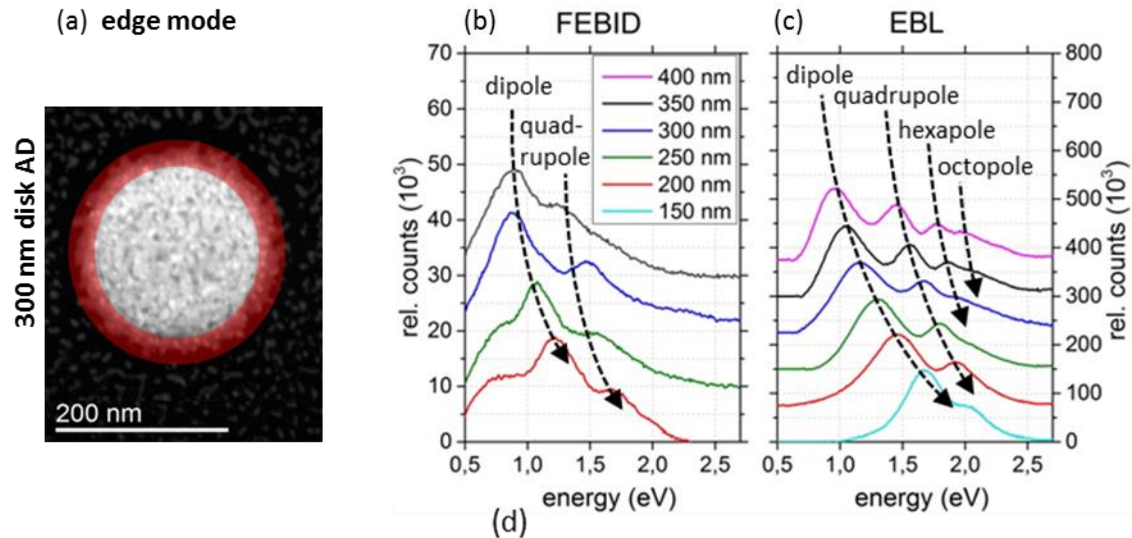

Figure 72: (a) Fully purified FEBID disc with an as-deposited diameter of 300 nm. During the purification the diameter shrank to 250 nm (for the shrinkage see Figure 69). The red ring at the edge, indicates the area of the disc, from which the edge modes in (b) were collected. (b) EELS-spectra for the 4 biggest discs produced via FEBID. The dipole and quadrupole mode can be clearly identified. (c) EELS-spectra of the EBL discs with diameters of 150 to 400 nm. Beside the dipole and the quadrupole mode, also the hexapole and octopole mode can be seen.

To look into the EELS-data in more detail, from the EELS-maps, spectra from a certain area of the disc were created. If the EELS signal along the edge of the discs is used, like it is demonstrated in Figure 72 (a) by the red ring, the plasmonic edge modes are received. Figure 72 (b) shows these edge modes for the 4 biggest fully purified FEBID discs (350, 300, 250 and 200 nm after purification – the absolute shrink for all 4 discs was approximately 50 nm). Clearly, the dipole and quadrupole mode can be seen. Comparison with the edge modes of EBL produced discs in Figure 72 (c), reveals that the dipole- and the quadrupole-mode are also characteristic for the EBL produced discs. However in the spectra of the EBL disc, also the hexapole and the octopole mode can be seen. Also it has to be mentioned, that the signal of peaks of the dipole and the quadrupole mode in Figure 72 (c) are a little bit better pronounced and higher. These differences stem from the non-ideal edges as already discussed for Figure 67 (c).

If the EELS data are collected from the centre of the discs, the so called breathing mode should be observed if the disc is plasmonically active. For that, once again the data of an as-deposited disc was compared with those of a fully purified one. In Figure 73 (a) the HAADF image of an as-deposited Au-C disc with a diameter of 400 nm and produced via FEBID can be seen. Figure 73 (b) shows the same disc after purification and a diameter shrinkage to 350 nm. As can be seen in the EEL-spectra in Figure 73 (c) for the as-deposited disc, which contains approximately 90 at.% carbon (≈ 70 vol.%), no plasmonic excitation can be seen (green curve). However, for the purified disc, a peak which represents the breathing mode can be clearly seen.

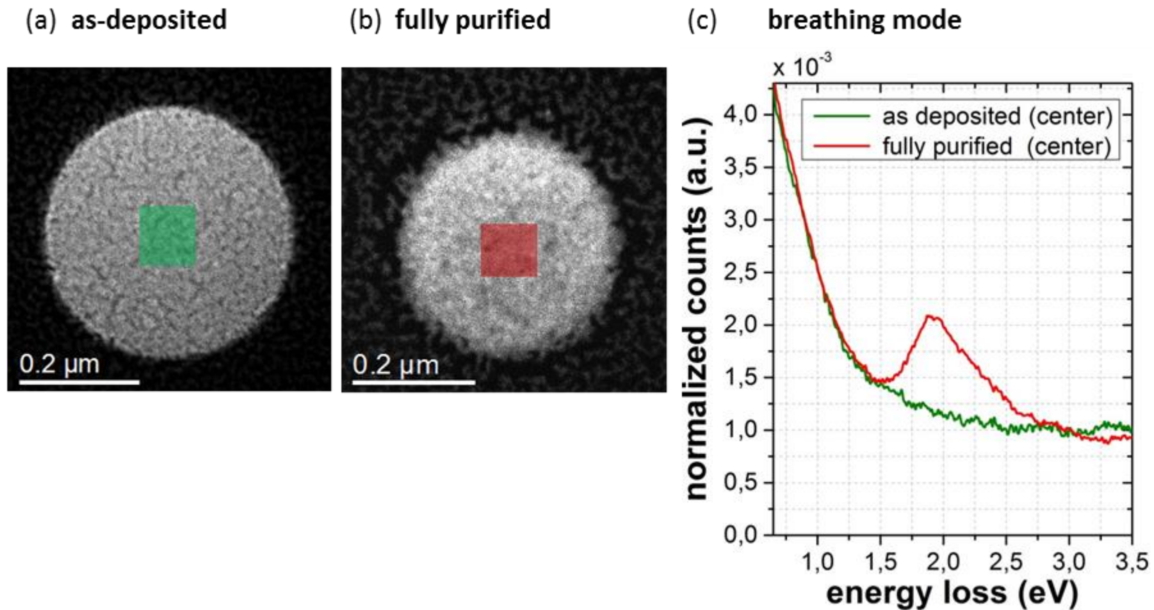

Figure 73: FEBID produced Au(C) disc with a diameter of 400 nm before purification (a) and after purification (b). The green and the red rectangle in the centres of the discs, indicates the approximate area from which the EELS-data for the breathing mode were collected. (c) spectra of the centre area of the as-deposited and fully purified disc. While in the spectrum of the as-deposited disc (green curve) nothing is visible, the spectrum of the purified disc (red curve) shows a peak representing the so called breathing mode.

Summing up, it can be said, that Au discs produced via FEBID and purification, show clearly plasmonic behaviour. Concerning the edge modes, the plasmonic behaviour differs a little bit from that of conventional, EBL produced, discs. This stems from the non-perfect edges of the FEBID discs. But although in detail, there can be found some differences concerning the plasmonic behaviour, it can be stated, that in general, the discs fabricated with this two methods, show a very similar plasmonic behaviour. This was the successful proof of concept, that FEBID is suitable to produce plasmonic nano-structures and opens up a wide field of new abilities and possible applications. FEBID provides three unique capabilities, which other techniques, especially EBL, can't: the possibility to produce real 3D structures, its applicability on almost every, also non-flat, surfaces and its flexibility concerning layout changes. This enables totally new kinds of plasmonic nano-structures, e.g. plasmonically active freestanding 3D structures (see Figure 51) or plasmonic structures at the end of optical fibres.

After the successful fabrication of planar plasmonic nano-structures with FEBID, in the following chapter of this Thesis, the suitability of FEBID for high-resolution plasmonic structures is investigated.

3.2.6 Downscaling and Plasmonic Au Bi-Rings

3.2.6.1 Idea and Expected Problems

After proving successfully that FEBID produced structures are well suitable for plasmonics, the idea was to advance in this field and expand FEBID technique to more complicated deposition shapes. In cooperation with the group of Prof. Michael Huth at the Goethe University Frankfurt the idea was developed to produce Au bi-ring structures like displayed in Figure 74 (a). The width of the rings was supposed to be 25 nm, which is close the fundamental resolution limit reachable with FEBID technique, as showed for the Pt based precursor [14]. Therefore, especially after purification, reaching this small ring width was considered a difficult task. The required diameters of the inner and the outer rings were 65 and 165 nm. The bi-rings should be produced on an ITO substrate. The location of the deposition was lying inside a topographical cavity with a depth of 300 nm (see Figure 81 (a)). The height should lie between 5 and 25 nm. However, higher rings are expected to be broader due to growth effects and FSE leading to proximity deposition. The thereby produced bi-rings should then be sent back to the group of Prof. Huth, who is experienced on the plasmonic nano-characterization. Being able to produce this bi-ring structures, would unfold the midterm perspective to produce this sort of structures for terahertz applications.

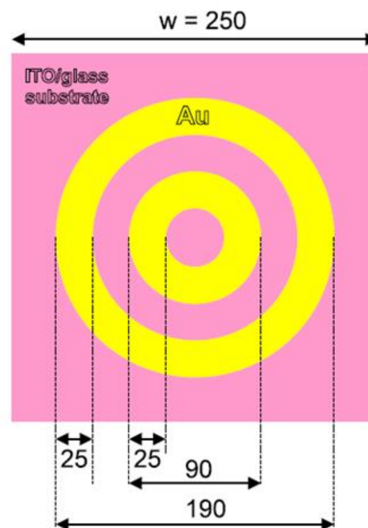

Figure 74: Schematic representation of the intended bi-ring structure. The rings should have a width of 25 nm and the diameter of the inner and the outer ring are supposed to be 65 and 165 nm. The rings should be produced on an ITO substrate inside a topographical cavity.

3.2.6.2 Fabrication Aspects of the Bi-Rings

In order to examine the limits and the possibilities in regard of the bi-ring structures, deposition experiments were performed. These deposition experiments were done on the ITO substrate beside the cavity, where the finally produced rings should be deposited. An array of bi-rings with different parameters was deposited, as can be seen in Figure 75 (a). Each ring was deposited in one single

pass. The array consisted of 4 sub-arrays representing the usage of different parameters and deposition strategies. The blue and the red squares in Figure 75 (a) indicate these sub-arrays. The blue squares signal that the outer ring was deposited before the inner ring, which is hereinafter referred to as “Outer to Inner”. The red squares indicate the opposite situation where the inner ring was fabricated before the outer ring. This is hereinafter referred to “Inner to Outer”. Also two different PoPs were used. For the rings at the top half in Figure 75 (a) 1 nm was used while 10 nm were used for the rings in the bottom half.

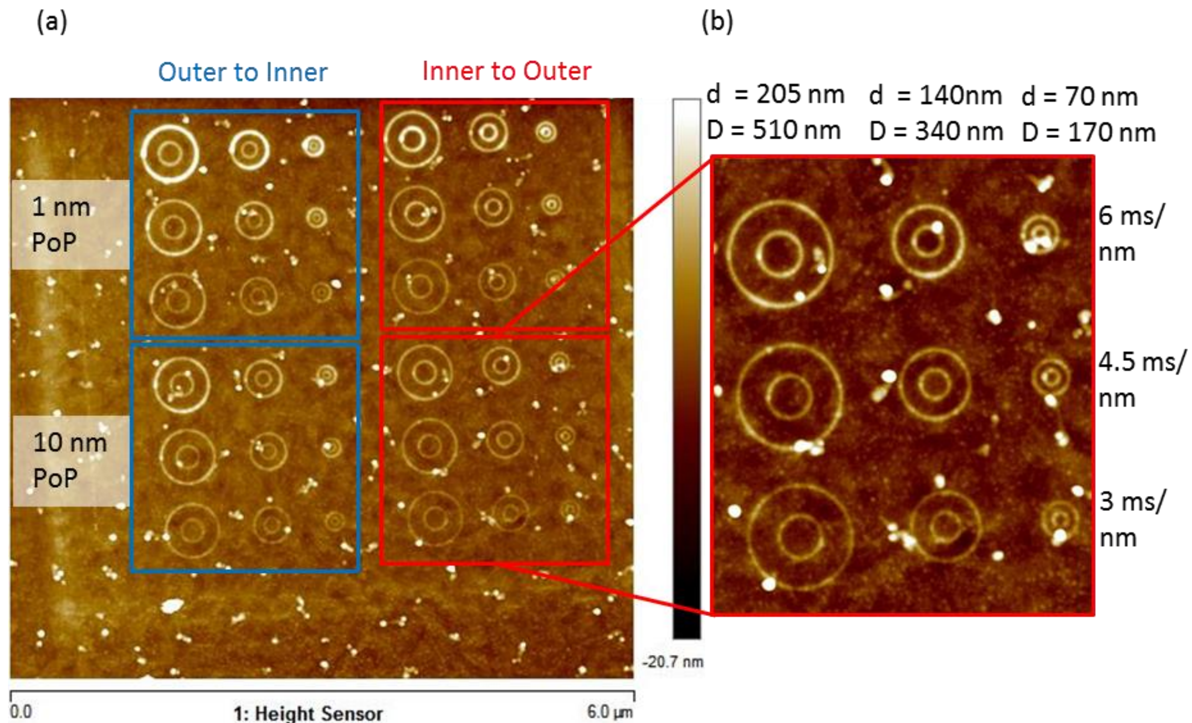

Figure 75: (a) AFM image of a bi-ring array to test the general deposition performance especially concerning the height and the FWHM. All the rings were produced in single pass depositions. The sub-arrays which are marked by the blue and red squares tested different strategies concerning the deposition order of the rings and the size of the PoP. The blue squares indicate that the outer ring was fabricated before the inner ring and the red squares the opposite. (b) Enlarged AFM image of the sub-array with the inner ring produced before the outer one with 10 nm PoP. The rings were fabricated with 3 different specific total exposure times (S-TET) with decreasing diameters. The diameter of the inner ring is indicated by the lower case letter “d”, while the diameter of the outer ring is indicated by the capital “D”.

Beside and above the enlarged image of the sub-array in Figure 75 (b) the parameter for the 9 bi-rings within a sub-array can be seen. The parameter variation within the other 3 sub-arrays is the same. For the specific total exposure time (**S-TET**) values of 3, 4.5 and 6 ms/nm were chosen. The specific total exposure time is the DT applied per nm of the ring pattern. More details about the S-TET can be found in chapter 2.1.2.4. The diameter of the rings was decreased in 2 steps to see, if the height and especially the sharpness of the ring structures (FWHM) is negatively influenced by the reduction of the diameter to the requested values. The largest bi-rings had ring diameters of 205 and

510 nm. The 2nd largest bi-rings had diameters of 140 and 340 nm and the bi-rings according to the requested specifications had diameters of 70 and 170 nm.

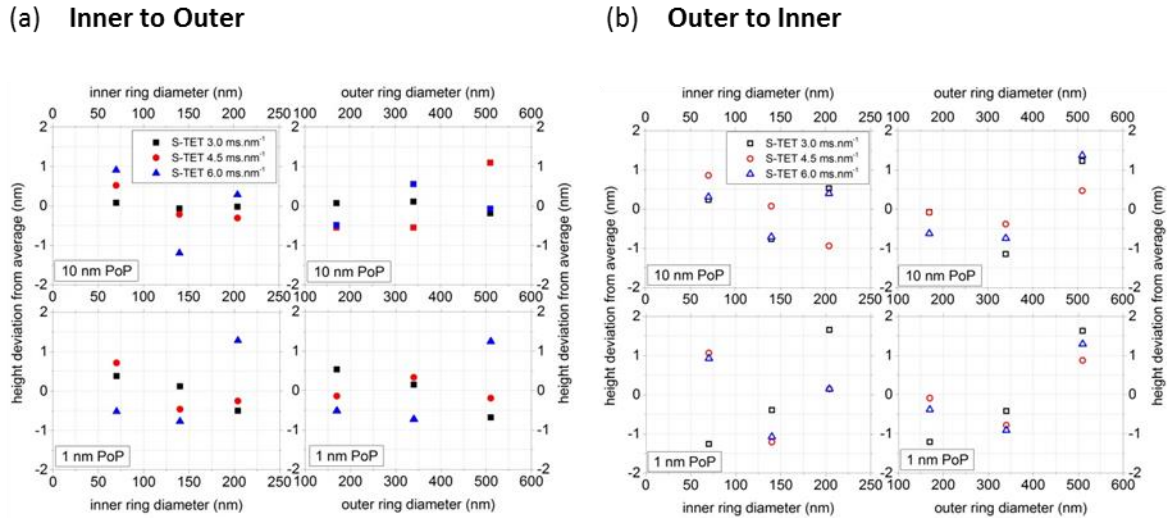

Figure 76: Height accuracy of the bi-rings for the different deposition strategies and parameters. (a) the filled symbols indicate the result for the Inner to Outer strategy, while (b) the open symbols show the result for the outer to inner strategy. The x-axes display the diameters of the inner or outer rings, while the y-axes indicate the deviation of the ring height in regard of the average height for the applied S-TET.

A very important aspect concerning the deposition behaviour of the bi-rings is the question, if the thickness of the rings varies in dependency on the S-TET, PoP and scan routine and how accurately a certain thickness can be reached. In Figure 76 the height accuracy for the Inner to Outer strategy (Figure 76 (a)), marked by filled symbols, as well as for the Outer to Inner strategy (Figure 76 (b)) ,marked by open symbols, can be seen. The y-axes thereby display the deviation of the ring height from the average ring height for a specific S-TET. The inner ring and the outer ring have thereby to be separated, since other effects, which will be considered below, lead to height differences between them. In general Figure 76 shows that the height accuracy is widely independent from the total heights originating from the different S-TET (see the different colours of the data points). The ring heights for depositions with the Inner to Outer strategy (see Figure 76 (a)) showed slightly better accuracy and stayed within a deviation of ± 1 nm, which is an excellent accuracy. The heights for the Outer to Inner strategy (see Figure 76 (b)) showed slightly higher variations, but were still around ± 1 nm. Therefore, FEBID process is extremely accurate considering, that the RMS surface roughness of the ITO substrate has a value 0.6 nm. Regarding the downscaling of the bi-ring diameters (from right to left in the diagrams), there were no critical effects observed, although all different parameters and strategies revealed slightly higher deposits in the sub-100 nm diameter regime (left part of the quadrants of Figure 76 (a) and (b)).

Figure 77 (a) shows the height tunability of the outer rings including the accuracy (error bars), which was derived from the data in Figure 76. Filled symbols indicate the Inner to Outer strategy while

open symbols indicate the Outer to Inner strategy. The S-TET (in general longer S-TET means larger height) as well as the PoP are possible tuning parameters for the ring height. The Outer to Inner deposition strategy shows higher growth rates due to an initially better gas situation but Inner to Outer is more preferably due to a more linear behaviour and higher accuracy. Also 10 nm PoP seems to show in general a better linear behaviour than 1 nm PoP.

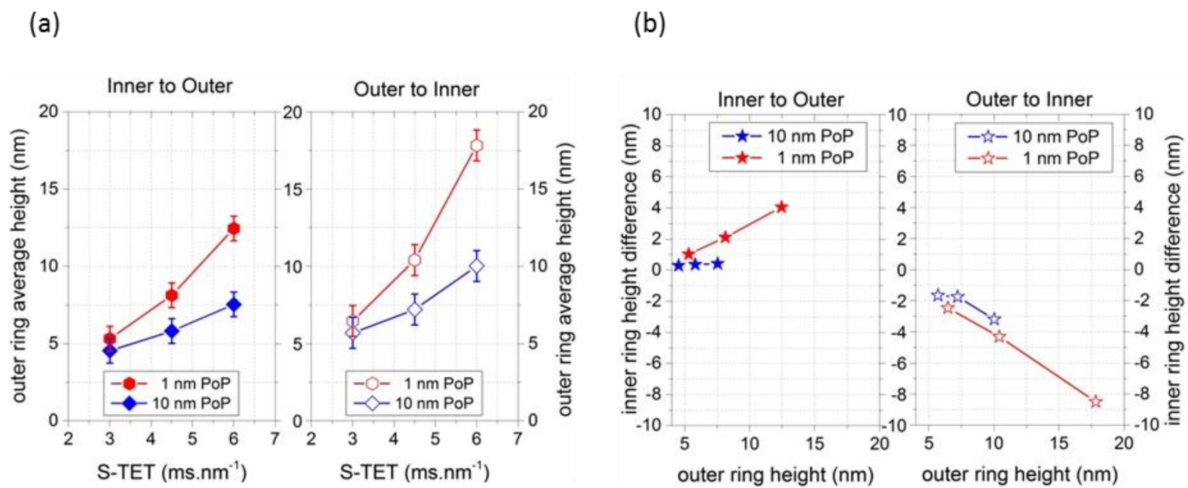

Figure 77: (a) Height tunability for the Outer ring including the accuracy (error bars) derived from Figure 76. Filled symbols indicate the Inner to Outer strategy while open symbols indicate the Outer to Inner strategy. Although, the Inner to Outer strategy has smaller growth rates, it's more preferably due to a more linear behaviour and higher accuracy. (b) Height difference of the inner ring (y-axes) in regard to the height of the outer ring (x-axes).

Figure 77 (b) displays the height difference of the inner ring, which is displayed along the y-axes, in regard of the outer ring. The x-axes display the average height of the outer ring. As can be seen, the Outer to Inner strategy leads to inner rings which are always significantly lower than the outer ring. The reason is that by depositing the outer ring first, a diffusion barrier is build which reduces the growth rate of the inner ring. It's especially remarkable that, although all the outer rings are less than 20 nm high, this low topographical heights are enough to represent a diffusion barrier for the precursor molecules. Higher PoP values leaded to a smaller ring height difference, because proximity growth becomes negligible. In particular the Inner to Outer strategy with 10 nm PoP showed practically no height difference between inner and outer ring. All that leads to the conclusion that Inner to Outer is definitely the better strategy over Outer to Inner. Also higher PoP values are desirable, since that maximized the height accuracy.

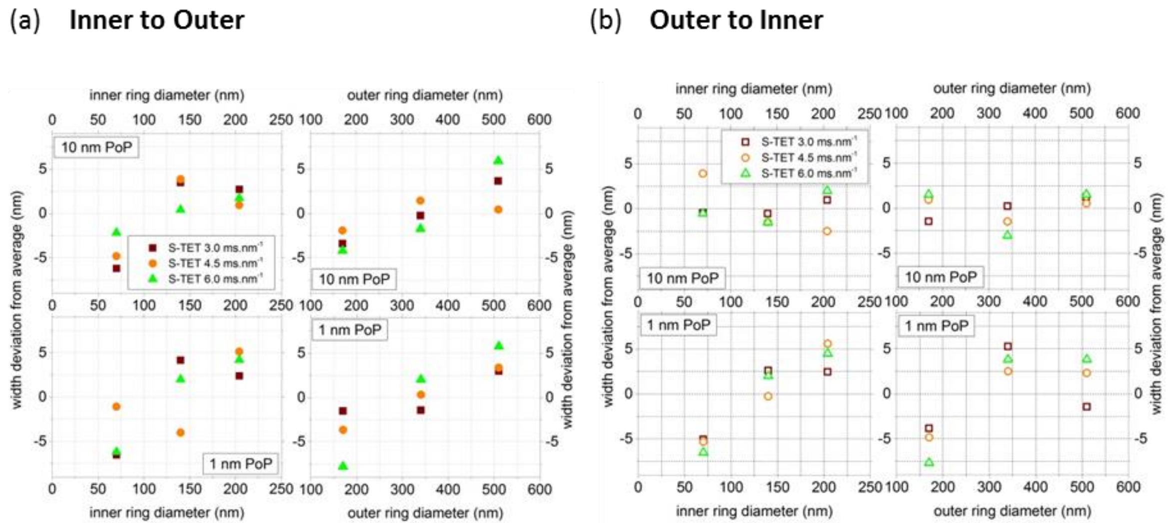

Figure 78: Width accuracy of the bi-rings for the different deposition strategies and parameters. (a) shows the result for the Inner to Outer strategy, while (b) shows the result for the outer to inner strategy. The x-axes display the diameters of the inner or outer rings, while the y-axes indicate the deviation of the ring width in regard of the average width for the applied S-TET.

Further, the influence of the S-TET, the PoP and the scan routine on the width of the rings was investigated. For the ring widths the full width half maximum (**FWHM**) of the cross section of the rings was measured. Figure 78 shows the accuracy of the width for the Inner to Outer strategy (Figure 78 (a)) as well as for the Outer to Inner strategy (Figure 78 (b)) in regard of the average width for the applied S-TET. Surprisingly, the data in Figure 78 strongly indicate that the reduction of the ring diameter decreases the ring width instead of the expected increase. This means the smaller rings are sharper and downscaling the rings to the smallest of the 3 bi-ring sizes is possible. Solely for the outer to inner strategy and 10 nm PoP the ring width didn't decrease for the smallest ring diameters. Therefore the Inner to Outer strategy seems again a better choice according to the ring width.

In Figure 79 the left side black axes and the associated blue squares represent the width/height ratio of the outer ring. The right side green axes and the associated green stars represent the width difference of the inner ring in relation to the according outer ring. The Inner to Outer strategy with 10 nm and 1 nm PoP in Figure 79 (a) and (b) resulted in inner rings which are equally sharp or even a little bit sharper than the outer ring. For Outer to Inner strategy in Figure 79 (c) and (d) the inner rings were broader than the outer rings. This means the rings which were produced first, were sharper. The cause for this behaviour is probably, that first produced rings profit from the better initial precursor gas situation.

Figure 80 (a) represents the width/height ratio of the smallest bi-rings of 70 nm inner ring diameter and 170 nm outer ring diameter. The width/height ratios give the impression that the small PoP (bright green data points) lead to sharper rings than the larger PoP (brown data points). However, the absolute ring widths in Figure 80 (b) reveal that this is not the case. The reason for that impression concerning the width/height ratios is that much of the broadening of the rings originates from the BSE. But the smaller PoP leads to higher deposits (see Figure 77 (a)) and therefore saturates

faster concerning the BSE width. The absolute width of the smallest bi-rings in Figure 80 (b) varies between 20 and 30 nm. There is a tendency that a larger S-TET leads to larger ring widths, because the deposit is higher, but since the height differences are small, that trend is not clear in this diagram.

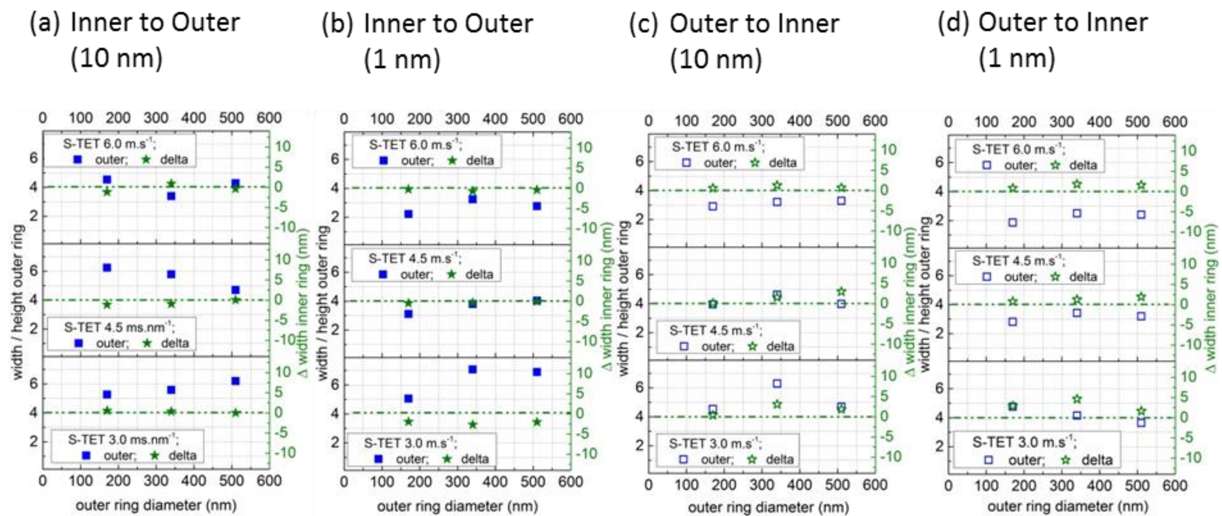

Figure 79: Width deviation of the inner ring in regard of the outer ring. (a) shows the Inner to Outer strategy for 10 nm PoP and (b) shows the same strategy for 1 nm PoP. (c) demonstrates the Outer to Inner strategy for 10 nm PoP and (d) presents the same for 1 nm PoP (filled symbols – Inner to Outer, open symbols – Outer to Inner). On the left (black) axes the width /height ratio of the outer ring can be seen. On the right (green) axes the deviation of the inner ring width can be found. The first ring seems to be in general sharper, which might be a result of the improved initial gas situation.

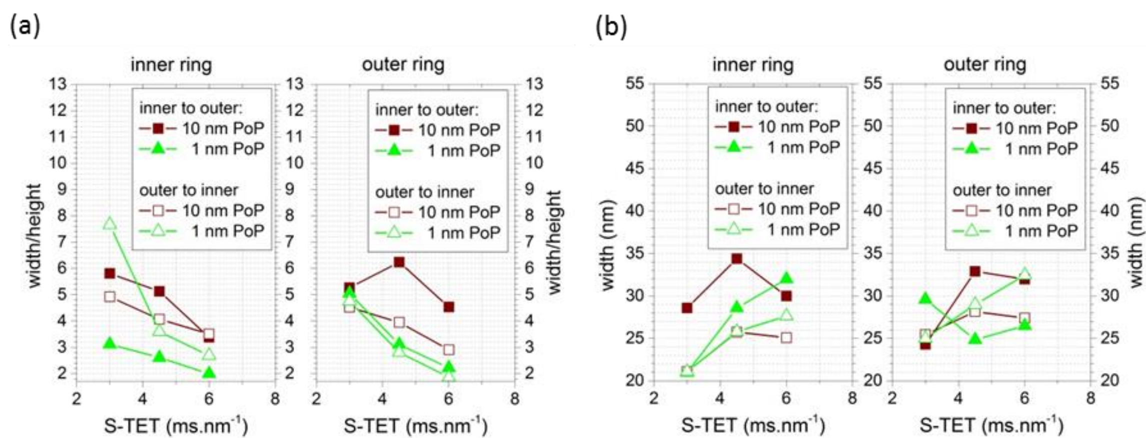

Figure 80: (a) Width / height ratio of the smallest bi-rings (70 nm diameter of the inner ring, 170 nm diameter of the outer ring) in dependence of the S-TET. Filled symbols represent data of the Inner to Outer strategy while empty ones represent the data of the Outer to Inner strategy. (b) Total ring width for the smallest bi-rings. The width / height ratios of the rings give the impression that smaller PoPs lead to sharper rings. However, the reason for that is initial BSE broadening since smaller PoPs produce higher deposits (see Figure 77 (a)) and by that saturates faster concerning their BSE width.

Summing up, it was possible to determine unequivocally, that the Inner to Outer strategy is superior over the Outer to Inner strategy. Higher PoPs results in better tuneable ring height and higher accuracy.

The height of the fully purified rings should be 5–15 nm, which meant for an approximated height loss of 2/3 that the as-deposited rings should be 15–45 nm high. To reach a better growth rate, a compromise of 4 nm PoP between fast growth rates for small PoP and better height accuracy for large PoP, was chosen. Still, much longer S-TET had to be chosen, which resulted in lift-off of the depositions from the surface, if a single pass strategy to deposit each ring was used. The strategy therefore had to be changed to a strategy, for which every ring was deposited with multiple passes. Thereby, first all passes for the inner ring were done before starting with the deposition of the outer ring.

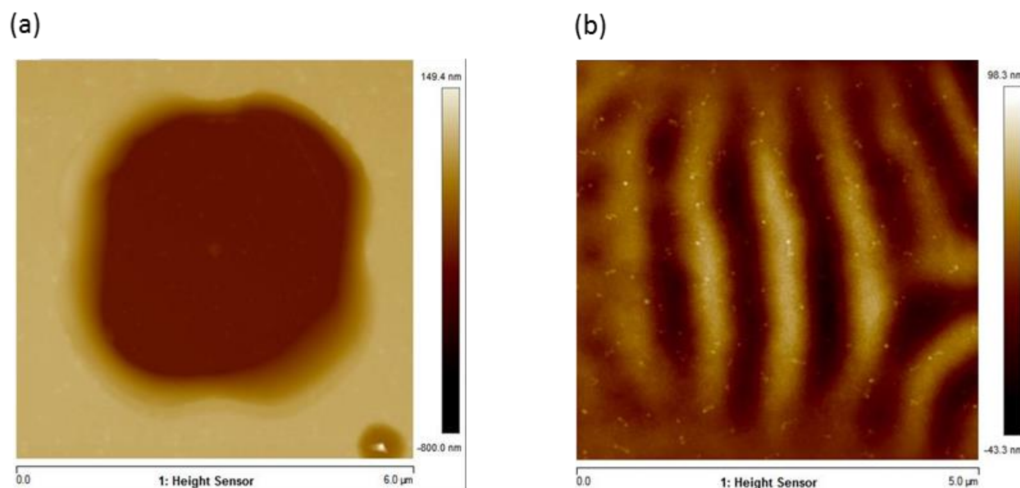

Figure 81: (a) AFM image of the final bi-ring deposition place inside a $5 \times 5\ \mu m^2$ large cavity with a depth of 300 nm. This leads to a different precursor behaviour and higher deposition rates. (b) AFM image of the ITO substrate after purification with 5 keV, 5 nA, 1 µs DT, 10 nm PoP, 10 Pa H_2O pressure and a dose of 60 C/cm². The height differences between minima and maxima of the wavy surface structure are up to 70 nm. The ITO seems to loosen from the glass slide.

As already mentioned above, the depositions for the bi-rings, whose plasmonic characteristics were going to be investigated, had to be done inside a topographical cavity with a depth of 300 nm. This resulted in totally different deposition characteristics originating probably from better precursor replenishment inside the cavity and therefore a higher surface density of adsorbed precursor molecules. The growth rates were larger by a factor of 3–4. Also, the height differences between inner and outer ring were so large, that the S-TET had to be chosen differently for the inner and outer ring to reduce the height difference to an acceptable degree. The results for the heights of the rings inside the cavity can be seen in Figure 82 (a). The inner rings inside the cavity were deposited with 4, 5 and 6 passes, which correspond to 8, 10 and 12 ms/nm S-TET (bright red data points with dashed lines), while the outer rings were deposited with 7, 8 and 9 passes, which correspond to 14, 16 and 18 ms/nm S-TET (dark red data points with solid lines). As comparison, the data points in

green in Figure 82 (a) represent the average height of the bi-rings on the plain substrate with single pass strategy from the previous experimental configuration from Figure 75. The purple data points represent the bi-ring depositions with multiple passes on the plain substrate.

In Figure 82 (b) the width of the bi-rings can be seen. Although the bi-rings deposited inside the cavity (red) have a larger width than the rings deposited on the plain (green and purple), the reason for that seems to be by a major part the much larger height of the rings in the cavity. However, it can also be seen, that the inner bi-rings for deposition inside the cavity (bright red with dashed line) are significantly broader with a width of 39 nm to 48 nm than the outer rings (dark red with solid line) with a width of 30 to 34 nm. The cause for that behaviour is probably the initial precursor situation caused by the cavity at the beginning of the deposition of the inner ring.

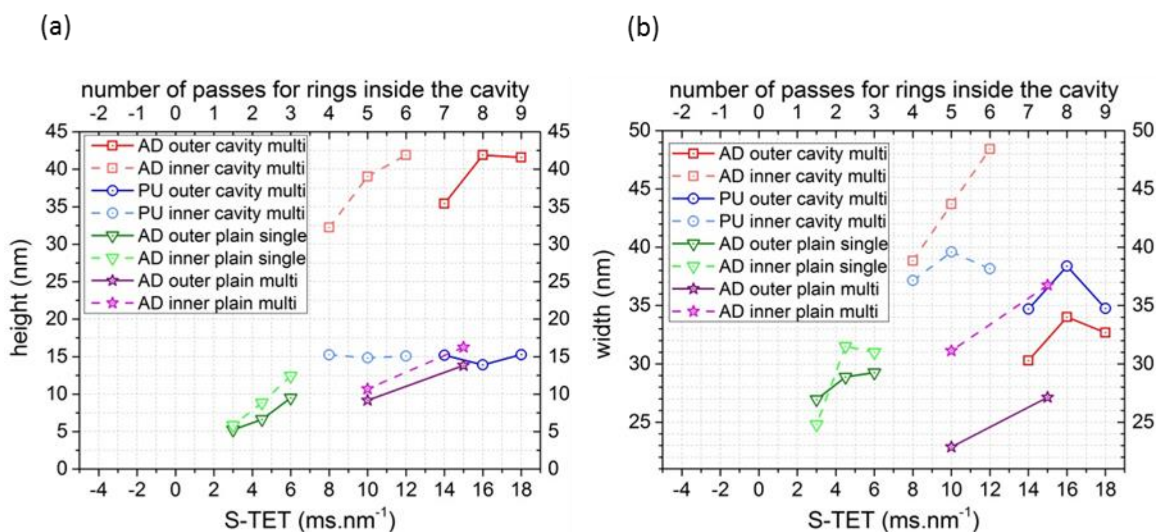

Figure 82: (a) Heights and (b) widths of bi-ring depositions with different strategies inside the cavity and on the plain substrate in dependence of the applied S-TET. Data points of the outer rings are displayed with solid lines and according dark colour while inner ring data points have dashed lines in between and the according bright colour. "AD" means as-deposited and "PU" purified. Red are the as-deposited rings inside the cavity and blue are the fully purified rings inside the cavity. (a) shows clearly that the deposition efficiency of the rings inside the cavity (red) is much higher than for rings on the plain, which were either deposited with a single pass (green) or with multiple passes (purple). (b) shows that the width of the rings inside the cavity (red) is larger than for the rings on the plain (green and violet). However, the reason for this is partly the much larger height of the bi-rings inside the cavity, which results in a bigger width of the bi-ring deposits.

The purification of the bi-rings was done with 5 keV, 5 nA, 1 µs DT, 4 nm PoP, 10 Pa H_2O pressure, $4 \times 4\ \mu m^2$ purification field and a purification dose of 60 C/cm². The purification had a large, unexpected effect on the ITO substrate, which can be seen in Figure 81 (b). After the purification the substrate showed a wavy topographical surface structure with height differences of up to 70 nm between the minima and maxima. This wavy surface structure probably originates from a delamination of the ITO layer from the glass slide.

The height of the bi-rings during purification reduced as expected by 57-65 rel.%. The absolute height of the rings inside the cavity after purification can be seen in Figure 82 (a) by the dark blue data with a solid line for the outer rings and the bright blue data with a dashed line for the inner rings. For all the different applied S-TET, which leaded to different heights of the as-deposited bi-rings, interestingly, the height for all the purified bi-rings, either inner or outer, was approximately 15 nm. However, it must be kept in mind, that because of the wavy surface structure, it was difficult to measure these heights exactly. The widths of the purified bi-rings inside the cavity were between 35 and 40 nm, as can be seen in Figure 82 (b). In Figure 83 (a) the as-deposited bi-ring inside the cavity with 4 passes for the inner ring and 7 passes for the outer ring can be seen. Figure 83 (b) shows the same, fully purified bi-ring which lost 57 rel.% of its height.

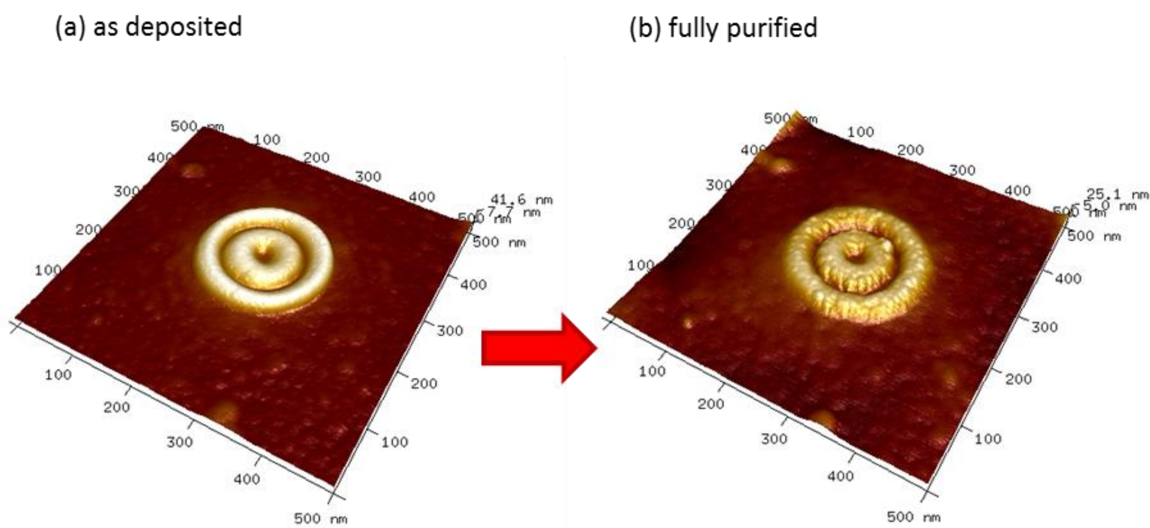

Figure 83: (a) As-deposited bi-ring inside the cavity with 4 passes and 32 ms/nm S-TET for the inner ring and 7 passes and 56 ms/nm S-TET for the outer ring. (b) the same ring after a purification with 5 keV, 5 nA, 1 µs DT, 4 nm PoP, 10 Pa H_2O pressure, $4 \times 4\ \mu m^2$ purification field and a dose of 60 C/cm². The height loss is 57 rel.%. The wavy structure of the substrate has been compensated by plane fitting the substrate.

As comparison to the bi-ring in the cavity, a bi-ring deposited on the plain can be seen in Figure 84. The bi-ring was deposited with 5 passes corresponding to 15 ms/nm S-TET for the inner and the outer ring. The bi-ring before purification can be seen in Figure 84 (a). During the purification the height of the bi-ring was reduced from approximately 15 nm to 5 nm, as can be seen in Figure 84 (b). The most important finding from this experiment was that a plasma cleaning step of 60 min, to a large extend didn’t alter the ring, as can be seen in Figure 84 (c). Although this was already observed for pad formed deposits in the µm-size, the same behaviour for such a fine ring structure was questionable, since the surface–volume ratio of the bi-ring deposits is much larger than for the pads, which might raise the Au removal by an etching effect from a non-measurable level to a measurable one. Since the height is quite small, the substrate not plain but wavy and the surface rougher than for the as-deposited bi-ring, reasonable results about the width couldn’t be gained from the data

anymore. Measuring the substrate surface roughness (measured at multiple places in a $250 \times 250\ \mu m^2$ large square) revealed that the RMS surface roughness was more than doubled from approximately 0.6 nm for the substrate around the as-deposited discs to approximately 1.2 nm for the substrate after purification and after plasma cleaning. It should be kept in mind that this is in absolute values still relatively smooth but has a non-deniable influence on very fine and low structures like these for sure. However, the wavy surface topology after purification, which didn't contribute to the RMS surface roughness, since the measuring area was too small, might be a bigger issue for some application.

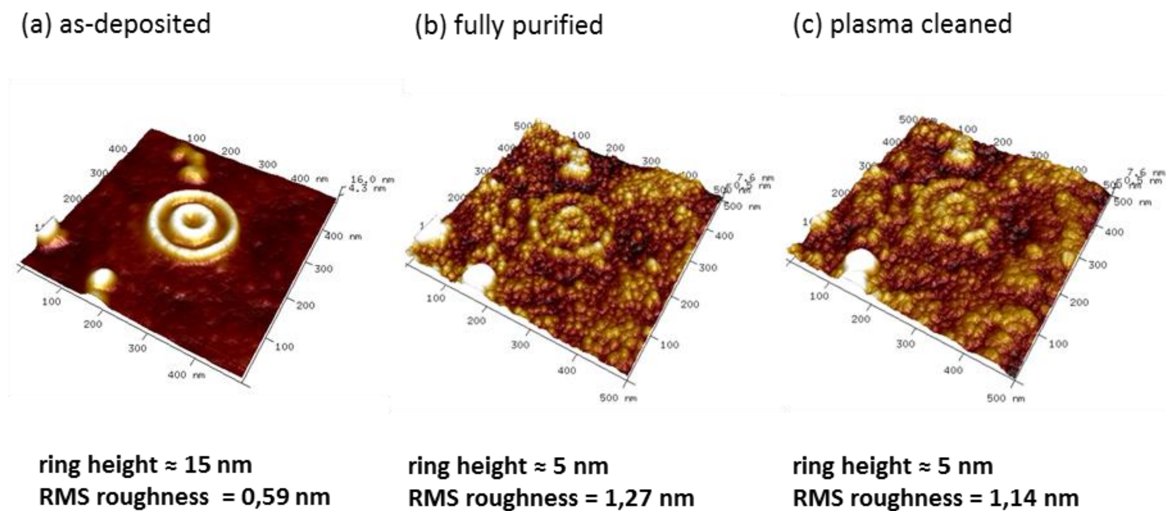

Figure 84: AFM images of a bi-ring deposited on the plain with 5 passes corresponding to 15 ms/nm S-TET. (a) shows the as-deposited bi-ring, while (b) shows the same bi ring after purification with 5 keV, 5 nA, 10 µs DT, 4 nm PoP, 10 Pa H_2O pressure, $5 \times 5\ \mu m^2$ purification field and a purification dose of 60 C/cm². (c) shows the AFM image of the same bi-ring after 60 min of plasma cleaning. The ring structure is uninfluenced by the purification.

3.2.6.3 Experimental Results Concerning the Plasmonic Activity of the Bi-Rings

Since there was a misunderstanding in the cooperation with the group of Prof. Huth, the bi-rings which were produced during this work, were single bi-rings. However, for the measurements at the Goethe University, arrays of 20×20 bi-rings were requested to be fabricated. Since producing these arrays, would have been beyond the frame of this master thesis, they were produced by J. Sattelkow. In the experimental results in Figure 85 (a) for these arrays of bi-rings with heights of 5-10 nm, clearly measurable spectral modulation could be observed around a wavelength of 650 nm. Both, un-purified (as-deposited) and purified samples showed that behaviour, but with a deeper feature for the purified ones. The results for 3 un-purified samples were highly consistent and the therefore clearly repeatable. Compared to the existing simulations in Figure 85 (b), the experimental dip was broader and weaker than the predicted one in this spectral range for an Au film thickness of 5-10 nm.

This was the first successful demonstration of plasmonic MTM (Model-Test-Mode; direct comparison of simulated with calculated results) with FEBID structures. These results open the mid time perspective for terahertz applications.

(a) (b)

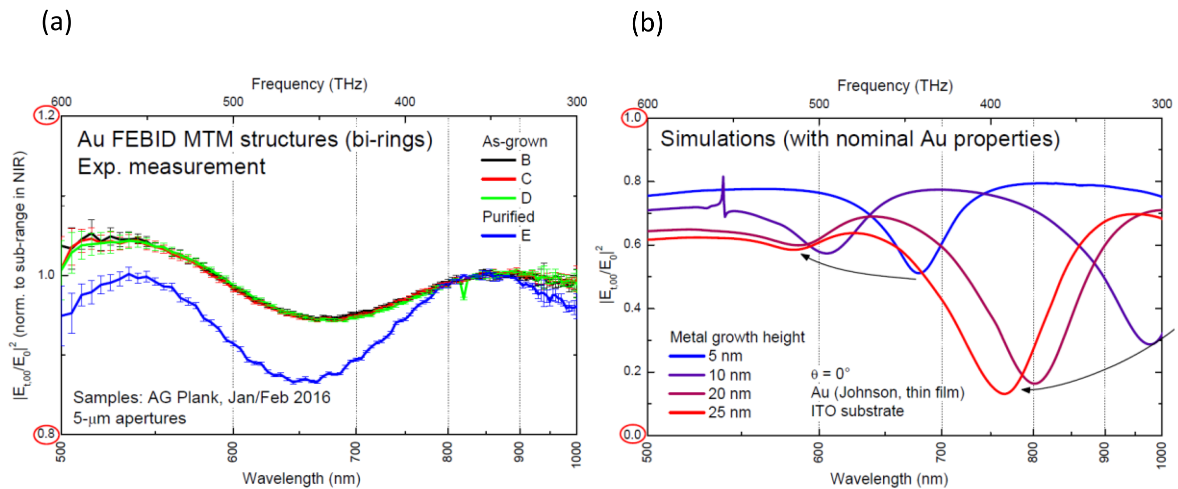

Figure 85: (a) Experimental measurement of the transmission curve for as-deposited and purified Au bi-ring arrays produced via FEBID and purification technique. The purified bi-rings have a height between 5 and 10 nm. Clearly a spectral modulation can be seen for as-deposited as well as for fully purified bi-rings in the transmission curve around a wavelength of 650 nm. (b) Calculated transmission curves for Au bi-rings for heights of 5-25 nm. Both was done by the group of Prof. Michael Huth.

3.2.7 Summary and Outlook

The main result of the 2nd part of this master thesis were first investigations of the deposition behaviour of the new $Me_2Au(acac)$ precursor. It could be shown that beside very basic deposit shapes, also very fine quasi 2D (bi-rings), as well as free standing 3D structures, can be produced. The same approach for the carbon removal as for the Pt precursor could be successfully applied and resulted in crack and pore free deposits. Most importantly, it could be successfully demonstrated that carbon free gold discs produced via FEBID are plasmonically active. Therefore, this technique should be suitable to build more complex plasmonic structures like free standing 3D structures not obtainable with other production techniques or bi-rings for terahertz plasmonics, for which the fabrication parameter were optimized in the last step of this thesis.

In more detail, the Au precursor deposition rate is approximately 8 times lower than the deposition rate for the platinum precursor, although the GIS is closer to the deposition side. This originates probably from a different precursor behaviour concerning the replenishment mechanism. Therefore, at the parameters used the deposition height was influenced by the patterning footprint, which is directly proportional to the replenishment time for the precursor (Figure 55). This indicates that the deposition is far in the MTL regime. It could be demonstrated with a free standing 3D crone (see Figure 55 (b)), that 3D structures are possible to manufacture with this precursor. TEM investigations revealed that the inner structure after deposition consists of 2-4 nm large Au grains embedded in a carbon matrix (see chapter 3.2.2).

The so called purification experiments revealed, that electron beam irradiation under the presence of water vapour resulted in a volume loss of (63±3) vol.% (see Figure 59 (a)). *Ex-Situ* EDXS measurements of fully purified pads in comparison to a sputtered layer of pure gold, strongly suggested, that the precursor deposits were really carbon free after purification (Figure 57 (b)). *In-Situ* EDXS measurements revealed a decreasing C/Au peak ratio with a saturation behaviour, which allows determining *in-situ* during the purification, when the carbon removal process is finished. The purification is a RRL (Reaction Rate Limited) process, which was revealed by the fact that for a wide range of different purification currents, the course of the C/Au peak ratio development was identical in regard of the dose or the relative exposure time (t_{rel}; see Figure 58). RMS surface roughness on the deposit was raised from 0.25 to 1.2 nm, which is in relative values a large change. However, in absolute values, this describes still a very smooth surface after purification. More importantly, the surfaces of the purified structures were crack and pore free and the original shape was maintained. For the $2 \times 2\ \mu m^2$ large pads, the volume shrinks manifested mostly in a height loss. The lateral shrink was below 3 rel.%. (see chapter 2.2.2).

As sometimes carbon contaminations appear on top of the purified layer or around the purified structure in the size of the purification field, it was crucial to discover that these carbon contaminations can be removed by a post purification O_2 plasma cleaning step of at least 30 min (see Figure 61). This relative long cleaning time is necessary since the process is non-linear and visible removal starts only after a long time (approximately 20 min). The pure gold structure is not affected by this plasma cleaning step. The development of this post-purification cleaning step was essential, since these contaminations could have been problematic for some applications (see chapter 3.2.4).

For the production of the plasmonic Au discs, the deposition parameters had to be adjusted to receive as sharp discs as possible (see Figure 64). Purification of the discs with different parameters revealed that a small current of 0.5 nA and an individual purification of each single disc, resulted in the best quality of the purified discs preventing holes, cracks and an elliptical shapes of the discs (see Figure 67). Independently, from the EDXS characterisation in the ESEM, it could be confirmed via TEM that purified Au deposits are chemically pure and carbon free (see Figure 68 (b)). An interesting observation was the fact that the discs showed a larger relative shrink than the 2 µm large discs. The measurement results suggest that when the deposit becomes smaller, at a certain point it breaks loose from the substrate and the shrinkage rises dramatically (see Figure 69). This has to be considered when purifying smaller structures. TEM EELS investigations to examine the plasmonic properties revealed that the discs produced via FEBID and purification showed very similar plasmonic behaviour as e-beam lithography produced discs (see Figure 71 and Figure 72). The differences stem mostly from fact that the edges of the FEBID discs are not ideally sharp. Also there is a small amount of proximity deposition around the disc. Unpurified discs however show no plasmonic behaviour at all (see Figure 73). Therefore, the proof of concept, that structures produced via FEBID and purification are in principal suitable for plasmonic experiments and applications, was successful. This opens the way to use FEBID to build plasmonic structures, which aren't possible with conventional techniques (see chapter 3.2.5).

Finally, it was demonstrated that thin bi-rings with a width a ring width around 30 nm can be produced and successfully downscaled to a diameters of 70 and 150 nm. The strategy to deposit first the inner ring and then the outer ring proved superior over the opposite. Generally larger PoPs showed better accuracy concerning the height while the width of the rings stayed mostly uninfluenced (see Figure 77 and Figure 80). A topographical cavity as the place for the deposits, changes the precursor behaviour (probably the replenishment mechanisms) at the deposition side leading generally to larger growth rates. The purification process using a high current and a high dose resulted in a very wavy topographical structure of the ITO substrate after the purification. However reducing the dose or even the current would have risked to receive a not completely purified quasi 2D structure, as previous examinations suggested [2,3]. First measurements of bi-ring arrays by the group of Prof. Michael Huth clearly revealed, that purified and also as-deposited rings show plasmonic behaviour in the form of a measurable spectral modulation in the transmission curve. This feature is steeper for the purified bi-rings (see Figure 85 (a)). Compared to simulated transmission curves for rings in the according height (see Figure 85 (b)), the transmission spectra looks similar. However, the dip around 650 nm is broader and weaker for the experimental data. The cooperation with the group of Prof. Huth is going to continue beyond this Thesis to improve and better understand the results. Further, there might open up the possibility for new terahertz applications for FEBID structures in the mid time perspective (see chapter 3.2.6).

Proving the suitability of FEBID produced nano-structures for plasmonic applications by the studies of discs and bi-rings was a very important milestone for highly pure metal FEBID deposits. Now that the proof of concept of FEBID produced plasmonic structures was successful, the path is open to use this technique for new types of plasmonic structures, whose fabrication is only possible with FEBID technique (e.g: freestanding 3D structures; see Figure 51)) and in general a wide use of FEBID in plasmonics.

4 Conclusion

This master thesis focused on two application concepts, which both require pure metallic nano-structures (Pt, Au). In combination with FEBIDs flexible direct-write capabilities, this thesis contributed to a meanwhile commercially available product (Pt nano-probes) and opened up new routes for on-demand fabrication of pure gold nano-structures for plasmonic applications.

In the first part, the goal was to modify a special type of cantilever with a highly conductive Pt layer. For the aimed thicknesses, a systematic multi-technique characterization revealed 5 keV as ideal primary electron energy for full purification at highest rates. Although the final electric resistivity of 180 µΩ.cm is more than an order of magnitude higher than for bulk Pt (≈ 10 µΩ.cm[45,49]), the study revealed that the inner nano-crystalline structure is most likely responsible for this discrepancy, which therefore can be considered as an intrinsic limitation of FEBID based Pt materials. The main achievement of this part, however, was the successful fabrication of Pt nano-pillars with diameters and end-radii of 50 nm and < 10 nm, respectively (see Figure 86 (a)). In collaboration with our industry partner SCL-Sensor.Tech.Fabrication GmbH we could fabricate the first electrical conductive self-sensing cantilever for high-resolution nano-probing which are meanwhile commercially available.

The vision for the second part was the FEBID based on-demand fabrication of plasmonic gold structures on virtually any given surface. By that, surface areas could be addressed where traditional approaches, such as lithography, are strongly limited or even impossible. In this thesis we could successfully transfer our previously developed e-beam purification approach to gold based FEBID materials. After optimization this process provides entirely carbon-free Au deposits without any surface cracks, pinholes or lateral shrink. Based on these achievements, we subjected FEBID based Au nano-discs to transmission-electron-microscopy based nano-characterization and could prove for the first time full plasmonic activities (see Figure 86 (b)) in agreement with conventional, by electron beam lithography (EBL) produced Au nano-discs. As a first step towards applications, the last part of this thesis successfully focused on the fabrication of Au bi-ring systems for THz plasmonics with dimensions very close to FEBIDs fundamental limitations. The full potential of this achievement will be exploited in combination with FEBID's unique fabrication capabilities, which also allows the fabrication of freestanding 3D structures beyond current limitations.

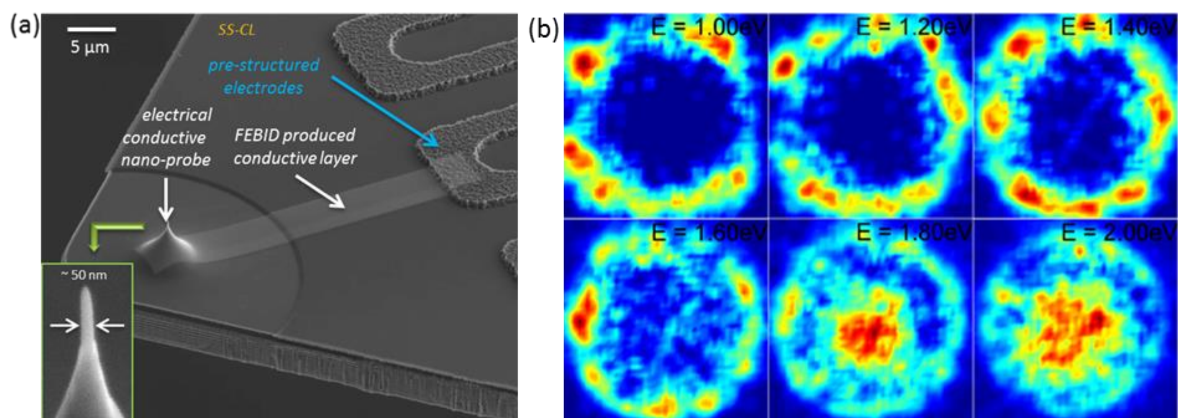

Figure 86: (a) Illustration of the proof of concept of electrical conductive self-sensing cantilevers. (b) STEM-EEL maps of a fully purified FEBID fabricated disc with approximately 350 nm diameter.

References

1. Utke, I., Moshkalev, S. & Russel, P. *Nanofabrication using focused ion and electron beams: principles and applications*. (Oxford University Press, 2012).

2. Geier, B. *et al.* Rapid and Highly Compact Purification for Focused Electron Beam Induced Deposits: A Low Temperature Approach Using Electron Stimulated H2O Reactions. *J. Phys. Chem. C* **118,** 14009–14016 (2014).

3. Geier, B. Rapid and Highly Compact Purification at Room Temperature for Focused Electron Beam Induced Pt-C Deposits. (Graz University of Technology, 2014).

4. Dual Beam. Available at: http://www.fei.com/products/dualbeam/. (Accessed: 10th January 2016)

5. FELMI Instrumentation. Available at: http://portal.tugraz.at/portal/page/portal/felmi/instrumentation/FIB. (Accessed: 10th January 2016)

6. Winkler, R. Implications of Precursor Dynamics on Nanostructures during Focused Electron Beam Induced Deposition. (Graz University of Technology, 2013).

7. Private communication with FEI.

8. Goldstein, J. *et al. Scanning Electron Microscopy and X-Ray Microanalysis*. (Springer, 1981).

9. Reimer, L. *Scanning Electron Microscopy: Physics of Image Formation and Microanalysis*. (Springer, 1998).

10. *Courtesy of Univ.-Doz. Dr. Harald Plank, Institute for Electron Microscopy and Nanoanalysis, Graz University of Technology, Austria, 2016*.

11. Plank, H., Haber, T., Gspan, C., Kothleitner, G. & Hofer, F. Chemical tuning of PtC nanostructures fabricated via focused electron beam induced deposition. *Nanotechnology* **24,** 175305 (2013).

12. Engmann, S. *et al.* Absolute cross sections for dissociative electron attachment and dissociative ionization of cobalt tricarbonyl nitrosyl in the energy range from 0 eV to 140 eV. *J. Chem. Phys.* **138,** (2013).

13. Botman, a, Mulders, J. J. L. & Hagen, C. W. Creating pure nanostructures from electron-beam-induced deposition using purification techniques: a technology perspective. *Nanotechnology* **20,** 372001 (2009).

14. Arnold, G. *et al.* Fundamental resolution limits during electron-induced direct-write synthesis. *ACS Appl. Mater. Interfaces* **6,** 7380–7387 (2014).

15. Utke, I., Hoffmann, P. & Melngailis, J. Gas-Assisted Focused Electron Beam and Ion Beam Processing and Fabrication. *J. Vac. Sci. {&} Technol. B Microelectron. Nanom. Struct.* **26,** 1197 (2008).

16. Winkler, R. *et al.* The nanoscale implications of a molecular gas beam during electron beam induced deposition. *ACS Appl. Mater. Interfaces* **6,** 2987–2995 (2014).

17. Winkler, R., Geier, B. & Plank, H. Spatial chemistry evolution during focused electron beam-induced deposition: origins and workarounds. *Appl. Phys. A* (2014). doi:10.1007/s00339-014-8496-y

18. Utke, I., Friedli, V., Purrucker, M. & Michler, J. Resolution in focused electron- and ion-beam induced processing. *J. Vac. Sci. Technol. B Microelectron. Nanom. Struct.* **25,** 2219–2223 (2007).

19. Szkudlarek, A., Gabureac, M. & Utke, I. Determination of the Surface Diffusion Coefficient and the Residence Time of Adsorbates via Local Focused Electron Beam Induced Chemical Vapour Deposition. *J. Nanosci. Nanotechnol.* **11,** 8074–8078 (2011).

20. Szkudlarek, A. *et al.* Lateral resolution in focused electron beam induced deposition: Scaling laws for pulsed & static exposure. *Appl. Phys. A* **117,** 1715–1726 (2014).

21. Botman, A., Mulders, J. J. L., Weemaes, R. & Mentink, S. Purification of platinum and gold structures after electron-beam-induced deposition. *Nanotechnology* **17,** 3779–3785 (2006).

22. LookChem. Available at: http://www.lookchem.com/-Trimethyl-methylcyclopentadienylplatinum-IV-/. (Accessed: 1st April 2016)

23. LookChem. Available at: http://www.lookchem.com/cas-149/14951-50-9.html. (Accessed: 1st April 2016)

24. Johnson, R. *Environmental Scanning Microscopy: An introduction to ESEM®*. (1996).

25. *Standard Operating Procedure FEI Quanta 200 Scanning Electron Microscope*. (San José State University, 2008).

26. Fitzek, H. M. Optimizing the Environmental Scanning Electron Microscope for chamber pressures up to 2700 Pa. (Graz University of Technology, 2014).

27. Fletcher, A. L., Thiel, B. L. & Donald, A. M. Amplification measurements of alternative imaging gases in environmental SEM. *J. Phys. D Appl. Phys.* **30,** 2249–2257 (1997).

28. Danilatos, G. D. Foundations of Environmental Scanning Electron Microscopy. *Adv. Electron. Electron Phys.* **No. 71,** 141 (1988).

29. Rattenberger, J., Wagner, J., Schröttner, H., Mitsche, S. & Zankel, A. A method to measure the total scattering cross section and effective beam gas path length in a low-vacuum SEM. *Scanning* **31(3),** 107–113 (2009).

30. *Handbook of Adhesive Technology, Revised and Expanded*. (Marcel Dekker, 2003).

31. Shun'ko, E. V. & Belkin, V. S. Cleaning properties of atomic oxygen excited to metastable state 2s^(2)2p^(4) (^(1)S_(0)). *J. Appl. Phys.* **102,** 083304 (2007).

32. *Product Brochure Fischione Instruments Model 1020 Plasma Cleaner*. (E.A. Fischione Instruments, Inc., 2013).

33. X-Ray Spectrum. *Australian Radiation Protection and Nuclear Safety Agency* Available at: http://www.arpansa.gov.au/radiationprotection/basics/xrays.cfm. (Accessed: 28th December 2015)

34. Plank, H. *et al.* Electron-Beam-Assisted Oxygen Puri fi cation at Low Temperatures for Electron-Beam-Induced Pt Deposits: Towards Pure and High- Fidelity Nanostructures. *ACS Appl. Mater. Interfaces* (2013).

35. Mehendale, S., Mulders, J. J. L. & Trompenaars, P. H. F. A new sequential EBID process for the creation of pure Pt structures from MeCpPtMe3. *Nanotechnology* **24,** 145303 (2013).

36. Auger electron spectroscopy. Available at: https://en.wikipedia.org/wiki/Auger_electron_spectroscopy. (Accessed: 30th December 2015)

37. *Courtesy of Ao.-Univ.-Prof. Dr. Werner Grogger, Institute for Electron Microscopy and Nanoanalysis, Graz University of Technology, Austria, 2016*.

38. Plank, H. *Rasterkraftmikroskopie - Atomic Force Microscopy (AFM)*. (Lecture Material, 2010).

39. Williams, D. B. & Carter, C. B. *Transmission Electron Microscopy*. (Springer, 2009).

40. Schmidt, F.-P. Mapping plasmons of designed nanostructures with fast electrons. (University of Graz, 2014).

41. Maier, S. A. *Plasmonics: Fundamentals and Applications*. (Springer, 2007).

42. Schmidt, F. P. *et al.* Dark plasmonic breathing modes in silver nanodisks. *Nano Lett.* **12,** 5780–5783 (2012).

43. Krug, M. Bright and Dark Plasmonic Modes of Silver Nanodisks. (University of Graz, 2014).

44. Pelton, M. & Bryant, G. W. *Introduction to metal-nanoparticle plasmonics*. (Wiley, 2013).

45. Kolb, F. Development of a Humidity Sensor based on Focused Electron Beam Induced PtC Deposition. (Graz University of Technology, 2013).

46. Michelitsch, S. G. Electrical in situ measurements during electron beam induced platinum deposition. (Graz University of Technology, 2011).

47. Plank, H. Elektrische Modifikation von Self-Sensing Cantileverspitzen mittels FEBID 3D Nanoprinting Zentrum für Elektronenmikroskopie Graz. *Final Rep. Inov. cheque* (2015).

48. Casino 2.48. Available at: http://www.gel.usherbrooke.ca/casino/index.html. (Accessed: 5th November 2014)

49. Kolb, F. *et al.* Variable tunneling barriers in FEBID based PtC metal-matrix nanocomposites as a transducing element for humidity sensing. *Nanotechnology* **24,** 305501 (2013).

50. Vaz, A. R., Da Silva, M. M., Leon, J., Moshkalev, S. A. & Swart, J. W. Platinum thin films deposited on silicon oxide by focused ion beam: Characterization and application. *J. Mater. Sci.* **43,** 3429–3434 (2008).

51. Brongersma, M. L. & Shalaev, V. M. 1.6 The Case for Plasmonics. *Science (80-.).* **328,** 440 (2010).

52. Ebbesen, T. W., Lezec, H. J., Ghaemi, H. F., Thio, T. & Wolff, P. A. Extraordinary optical transmission through sub-wavelength hole arrays. *Nature* **391,** 667–669 (1998).

53. Pendry, J. B. Negative refraction makes a perfect lense. *Phys. Rev. Lett.* **85,** 3966–3969 (2000).

54. Anker, J. N. *et al.* Biosensing with plasmonic nanosensors. *Nat. Mater.* **7,** 442–453 (2008).

55. Hirsch, L. R. *et al.* Nanoshell-Mediated Near-Infrared Thermal Therapy of Tumors under Magnetic Resonance Guidance. *Proc. Natl. Acad. Sci. U.S.A.* **100,** 13549–13554 (2003).

56. Cao, L., Barsic, D. N., Guichard, A. R. & Brongersma, M. L. Plasmon-assisted local temperature control to pattern individual semiconductor nanowires and carbon nanotubes. *Nano Lett.* **7,** 3523–3527 (2007).

57. Cai, W., White, J. S. & Brongersma, M. L. Compact, high-speed and power-efficient electrooptic plasmonic modulators. *Nano Lett.* **9,** 4403–4411 (2009).

58. Noginov, M. A. *et al.* Demonstration of a spaser-based nanolaser. *Nature* **460,** 1110–1112 (2009).

59. Oulton, R. F. *et al.* Plasmon lasers at deep subwavelength scale. *Nature* **461,** 629–632 (2009).

60. Stockman, M. I. The spaser as a nanoscale quantum generator and ultrafast amplifier. *J. Opt.* **12,** 024004 (2010).

61. *Courtesy of DI Robert Winkler, Institute for Electron Microscopy and Nanoanalysis, Graz University of Technology, Austria, 2016*.

62. Plank, H. *et al.* Fundamental Proximity Effects in Focused Electron Beam Induced Deposition. *ACS Nano* **6,** 286–294 (2012).